

Department of Physics and Astronomy

University of Heidelberg

Master Thesis
in Physics
submitted by
Ann-Kathrin Perrevoort
born in Gronau (Westfalen)

2012

Characterisation of
High Voltage Monolithic Active Pixel Sensors
for the Mu3e Experiment

This Master thesis has been carried out by
Ann-Kathrin Perrevoort
at the
Physikalisches Institut Heidelberg
under the supervision of
Prof. Dr. André Schöning

Characterisation of High Voltage Monolithic Active Pixel Sensors for the Mu3e Experiment:

In this Master thesis, *High Voltage Monolithic Active Pixel Sensors (HV-MAPS)* have been characterised and the suitability for their use in the *Mu3e* experiment has been evaluated.

The *Mu3e* experiment is an upcoming experiment which searches for the lepton flavour violating muon decay $\mu^+ \rightarrow e^+e^-e^+$ which is forbidden in the Standard Model of particle physics. The observation of this decay would be a clear sign for new physics.

In order to achieve the projected sensitivity of one in 10^{16} muon decays, challenges like high muon rates and minimal multiple scattering have to be met. The tracking detector will therefore be based on *HV-MAPS*, a novel concept for thin silicon pixel sensors with integrated electronics and fast charge collection. The first two *HV-MAPS* prototypes are tested with internally generated test pulses and different kinds of particles like X-rays, photons, γ - and β -radiation as well as pions. Additionally, the temperature dependence of the detection performance has been studied.

The *HV-MAPS* technology turns out to be very promising for *Mu3e* as for instance signal-to-noise ratios in excess of 20 are measured. Nevertheless, shaping times in the range of μs show that for the actual use in the experiment the timing has to be significantly improved.

Charakterisierung von Monolithischen Aktiven Pixel-Sensoren in Hochspannungs-Technologie für das Mu3e-Experiment:

Im Rahmen dieser Master-Arbeit wurden *Monolithische Aktive Pixel-Sensoren in Hochspannungs-Technologie (HV-MAPS)* charakterisiert und ihre Eignung für den Einsatz im *Mu3e*-Experiment überprüft.

Das geplante *Mu3e*-Experiment sucht nach dem Leptonflavourzahl-verletzenden Zerfall $\mu^+ \rightarrow e^+e^-e^+$, welcher im Standard-Modell der Teilchenphysik verboten ist. Die Beobachtung dieses Zerfalls wäre ein klares Zeichen für neue Physik.

Um die geplante Sensitivität von einem in 10^{16} Myon-Zerfällen erreichen zu können, muss der Detektor hohen Anforderungen wie etwa hohen Myon-Raten und geringer Vielfachstreuung gerecht werden. Daher wird der Spurdetektor auf *HV-MAPS* beruhen, einem neuen Konzept für dünne Silizium-Pixel-Sensoren mit integrierter Elektronik und schneller Ladungssammlung.

Die ersten beiden *HV-MAPS*-Prototypen wurden mit intern generierten Test-Pulsen und verschiedenen Sorten von Teilchen – wie zum Beispiel Röntgenstrahlen, Photonen, γ - und β -Strahlung sowie Pionen – getestet. Zudem wurde der Einfluss der Temperatur auf die Detektor-Eigenschaften untersucht.

Die *HV-MAPS*-Technologie stellt sich als sehr vielversprechend für das *Mu3e*-Experiment heraus. So wurde beispielsweise ein Signal-zu-Rausch-Verhältnis von über 20 gemessen. Dennoch zeigen Zeitkonstanten des Pulsformers im Bereich von μs , dass für den tatsächlichen Einsatz im Experiment das Zeitverhalten noch deutlich verbessert werden muss.

サルも木から落ちる。

Japanese proverb

Contents

I	Introduction	1
1	Introduction	3
2	Theory	5
2.1	The Standard Model	5
2.2	Lepton Flavour Violating Decays of the Muon	7
3	The Mu3e Experiment	11
3.1	The Decay of the Muon	12
3.1.1	Standard Model Decays	12
3.1.2	Lepton Flavour Violating Muon Decays	13
3.2	Current Experimental Situation	13
3.2.1	SINDRUM	13
3.2.2	MEG	14
3.2.3	Muon Conversion Experiments	14
3.3	Sources of Background	15
3.3.1	Accidental Background	15
3.3.2	Background Due to Internal Conversions	16
3.4	The Concept of the Mu3e Experiment	17
3.4.1	The Muon Beam	18
3.4.2	The Target	20
3.4.3	The Design of the Mu3e Detector	20
4	Pixel Sensors for Mu3e	25
4.1	Silicon as a Semiconductor	25
4.2	Interactions of Electrons and Positrons with Matter	28
4.2.1	Collision Stopping Power	29
4.2.2	Bremsstrahlung	30
4.3	HV-MAPS	32

II	Characterisation of the MuPix Sensor	35
5	The Experimental Setup	37
5.1	The Prototypes MuPix1 and MuPix2	37
5.2	The Setup	40
6	Measurements with Injection Pulses	43
6.1	Injection-Scan for a Single Pixel	43
6.2	Injection-Scan and Threshold-Scan for the Entire Pixel Matrix	47
6.3	TDAC-Tuning	48
6.4	Pixel Response Time	51
7	Measurements with LEDs and Laser Diodes	55
7.1	Latency and Time-over-Threshold	55
7.2	Pulse Shape	58
7.3	Double Pulse Resolution	60
7.4	Readout of the Total Pixel Matrix	64
8	Measurements with Radioactive Sources	65
8.1	Radioactive Sources	65
8.2	Time over Threshold Spectra	66
9	Measurements with X-ray Fluorescence	71
10	Temperature Dependence	77
10.1	⁵⁵ Fe Source	77
10.2	Test Pulses	77
10.2.1	ToT Spectra	77
10.2.2	Injection Scan	82
10.3	Temperature Sensor	82
11	Testbeam Measurements at the SPS	87
III	Discussion	93
12	Discussion and Outlook	95
12.1	Discussion	95
12.2	Summary	99
12.3	Outlook	100

IV Appendix	101
1 PN-Junction	103
2 The CR-RC Filter	107
3 The Configuration and Data Readout Software	111
Lists	115
4 List of Figures	115
5 List of Tables	117
Bibliography	119

Part I

Introduction

1 Introduction

The Standard Model is the basis of today's particle physics. It describes all known elementary particles and their interactions.

The lepton flavour is a conserved quantity in the Standard Model. No interaction is allowed which turns a lepton of one generation into a lepton of another generation. But the observation of neutrino oscillations led to extensions of the Standard Model which allow for lepton mixing. A charged lepton flavour violating process like $\mu^+ \rightarrow e^+e^-e^+$, for which will be searched in the *Mu3e* experiment, can thus be realised via neutrino mixing, but only on loop-level.

As the Standard Model leaves many questions unanswered, there are many theories beyond the Standard Model. Often, charged lepton flavour violating processes are predicted at experimentally accessible energy scales. As in the extended Standard Model $\mu^+ \rightarrow e^+e^-e^+$ mediated by neutrino mixing is highly suppressed, its observation would be a clear sign for new physics.

The proposed *Mu3e* experiment (see [B⁺12]) will search for the lepton flavour violating decay $\mu^+ \rightarrow e^+e^-e^+$ with a sensitivity of $\text{BR}(\mu^+ \rightarrow e^+e^-e^+) \approx 10^{-16}$ at 90% confidence level, four orders of magnitude better than the previous *SINDRUM* experiment [B⁺88]. This sensitivity can only be achieved by a detector with high momentum and vertex resolution which is capable to suppress the background efficiently and to handle the necessary high muon rates.

The *Mu3e* detector is therefore based on a tracking detector consisting of a novel kind of silicon pixel sensor, the so-called *High Voltage Monolithic Active Pixel Sensors* (*HV-MAPS*). These sensors rely on a thin charge

1 Introduction

collecting diode depleted by a relatively high reverse bias voltage and have thus an excellent charge collection time. The digitisation of the signals is already integrated in the sensor itself, an additional readout chip is unnecessary. As most of the undepleted bulk does not contribute to particle detection, thinning of the sensors becomes possible and thus the material amount in the active detector volume can be significantly reduced, leading to an improvement of the multiple scattering dominated spatial resolution.

The suitability of the *HV-MAPS* concept for the *Mu3e* experiment is tested in this thesis by characterising the first two prototypes: *MuPix1* and *MuPix2*.

With internally generated pulses, the noise level can be determined. Moreover, these test pulses are used for a tuning procedure that reduces pixel-to-pixel non-uniformities. The timing of the sensor, especially latency and double pulse resolution, is studied with a LED setup. Spectral measurements are performed with radioactive sources and a X-ray fluorescence setup. For this purpose, the time over threshold information is read out which is a measure for the deposited energy. The X-ray fluorescence setup in particular allows for energy calibrations. Furthermore, the influence of temperatures above room temperature on the sensor performance is studied. Additionally, a first testbeam measurement at the *SPS* at *CERN* has been performed.

The tested *MuPix* prototypes appear to be very promising candidates for *Mu3e*, but for the actual use in the later experiment an improvement of the timing has to be achieved. Thus, there will be a further generation of prototype sensors.

2 Theory

The Standard Model of particle physics does not allow interactions in which the lepton flavour is violated – like in the decay $\mu \rightarrow eee$. It can be extended to allow neutrino mixing as observed in neutrino-oscillation experiments. Here, charged lepton flavour violation is still forbidden at tree level but can be achieved on loop-level via neutrino mixing. Nevertheless, $\mu \rightarrow eee$ is highly suppressed, even in the extended Standard Model. Many theories beyond the Standard Model instead predict charged lepton flavour violation with a much higher probability.

This chapter gives an overview about the Standard Model and introduces lepton flavour violation in muon decays.

2.1 The Standard Model

The Standard Model is a quantum field theory that explains the fundamental constituents of matter. It consists of twelve fermionic elementary particles – six leptons and quarks respectively – and their antiparticles, arranged in three generations (see figure 2.1). Interactions are mediated by the gauge bosons. Additionally, the Standard Model includes the Higgs boson in order to be able to explain the origin of mass.

The first generation of leptons consists of the negatively charged electron e^- and the uncharged electron-neutrino ν_e and is characterised by the electron lepton flavour number L_e . In an analogous manner, the second generation (muon μ^- and muon-neutrino ν_μ) and third generation (tau τ^- and tau-neutrino ν_τ) are given the muon lepton flavour number L_μ and the tau lepton flavour number L_τ . Lepton flavour is considered to be a conserved quantity in the Standard Model. The upcoming *Mu3e*

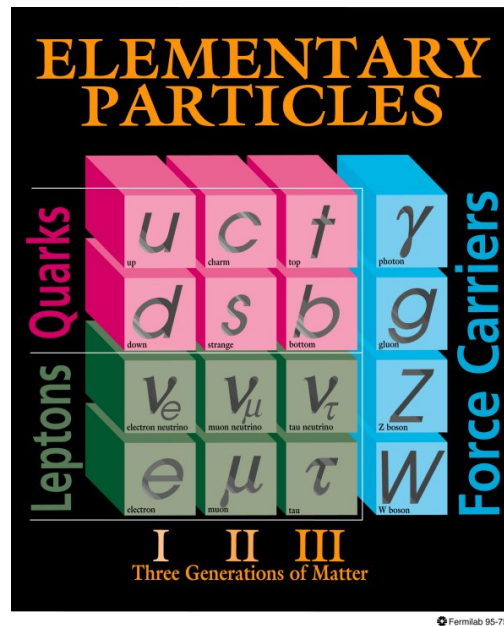


Figure 2.1: Elementary particles and gauge bosons in the Standard Model of particle physics (graphic taken from [FER12])

experiment will probe the conservation of the muon and electron lepton flavour.

Similarly, the first generation of quarks consists of the up quark u and the down quark d , whereas the second generation is made up by the strange quark s and the charm quark c and the third by the bottom quark b and the top quark t .

The interactions between the elementary particles are mediated by exchange of gauge bosons with spin 1: the photon γ for the electromagnetic force, the W^+ , W^- and Z^0 for the weak interaction and a set of eight gluons for the strong interaction.

So far, the gravitational force is not included in the Standard Model.

Recently, the *ATLAS* and *CMS* experiment at the *Large Hadron Collider LHC* at *CERN* reported evidence for a new particle consistent with the Higgs boson at (125–126) GeV [Hig12]. The Higgs boson is the last particle missing in the Standard Model. It is a scalar boson with spin 0 predicted by the Higgs mechanism, which is responsible for the electro-weak symmetry

breaking, that causes the masses of the W^\pm and the Z^0 , and gives, in addition, mass to the other elementary particles.

Experiments like *Super-Kamiokande* [F⁺98], *SNO* [A⁺01] and *KamLAND* [E⁺03] have discovered that neutrinos from one generation can turn into neutrinos of another generation, the so-called neutrino oscillations. This implies that neutrinos have a small, but not vanishing mass. And moreover, this process is lepton flavour violating. The Standard Model can be extended to allow lepton mixing and thus explain neutrino-oscillations. Even though it has been very successful, e.g. in predicting the W^\pm and Z^0 bosons, the Standard Model and the extended Standard Model have a lot of open questions. A set of free parameters is needed whose values are solely determined by experiments and cannot be derived from calculation. They do not explain why there are three generations of leptons and why the mixing between quarks and between neutrinos is so different or why the masses of the neutrinos are so small compared to others. Thus, a lot of new theories arose like grand unified theories or supersymmetry which all need experimental investigation.

2.2 Lepton Flavour Violating Decays of the Muon

The decay $\mu^+ \rightarrow e^+e^-e^+$, that the *Mu3e* experiment is looking for, is a lepton flavour violating decay. It can be realised in the extended Standard Model which includes lepton mixing. Figure 2.2 shows the corresponding Feynman diagram. The violation of the lepton flavour occurs via neutrino mixing in a loop. The W^+ with a mass of $80.4 \text{ GeV}/c^2$ is extremely heavy compared to the mass difference of the light neutrinos ($\mathcal{O}(10 \text{ meV})$). Thus, the process is heavily suppressed by a factor of $\sim \left(\frac{\Delta m_\nu}{m_W}\right)^4$ and has a

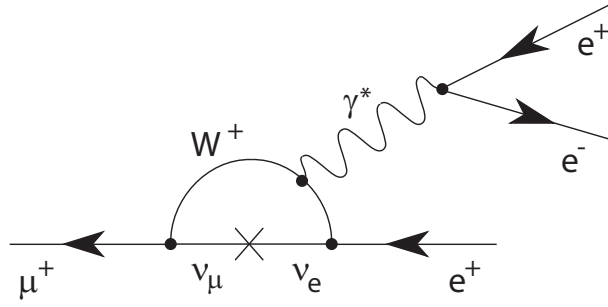


Figure 2.2: Feynman diagram of the decay $\mu^+ \rightarrow e^+e^-e^+$ via neutrino mixing in a loop

branching ratio of $\text{BR} < 10^{-50}$. Any observation of the decay $\mu \rightarrow eee$ ¹ is therefore a clear sign for new physics beyond the Standard Model.

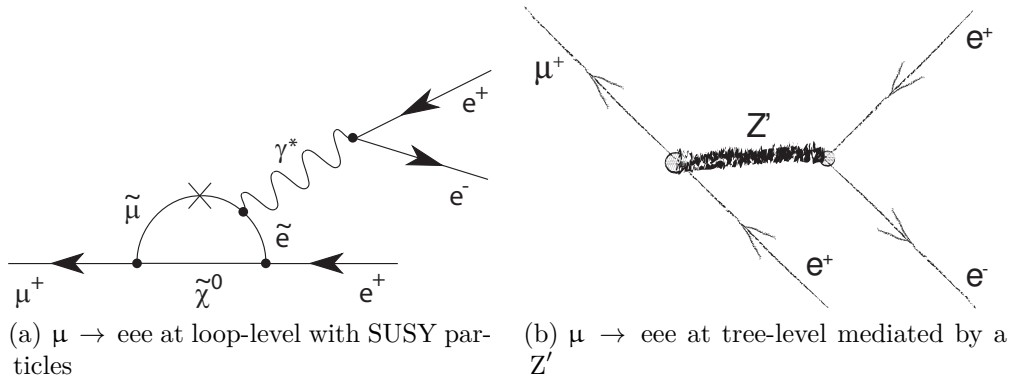
Many models exist which predict charged lepton flavour violating processes mediated by new, heavy particles. For the decay $\mu \rightarrow eee$, these processes can be split into two categories: processes which occur at loop-level like the one involving neutrino-mixing and those at tree-level.

Loop-level decays that have a higher branching ratio than the previously discussed process can be realised by having super-symmetric (SUSY) particles like sleptons running in the loop (see figure 2.3(a)). The lepton flavour violation is mediated by slepton mixing. SUSY particles are expected to have high masses and consequently the mass differences could be large as well. This would result in experimentally accessible branching ratios for $\mu \rightarrow eee$.

At tree-level the lepton flavour violating process is mediated by a single particle (see figure 2.3(b)). For example, models with extra-dimensions or new Z bosons predict such particles. However, these particles must have a high masses, which results in the suppression of this type of decay.

Experiments like *SINDRUM* ($\mu \rightarrow eee$) and *MEG* ($\mu \rightarrow e\gamma$) and the future *Mu3e* experiment give constraints on the model parameters.

¹For the sake of completeness: The decay $\mu \rightarrow e\gamma$ has a very similar diagram except for the $\gamma \rightarrow e^-e^+$ production vertex. Nevertheless, its branching ratio is also far beyond experimental reach.


 Figure 2.3: Diagrams of the decay $\mu^+ \rightarrow e^+e^-e^+$ in new physics models

In order to be able to estimate the reach in mass scale for various sensitivities, for example of the decays $\mu \rightarrow eee$ and $\mu \rightarrow e\gamma$, a simplified Lagrange function can be utilised [B⁺12]

$$\mathcal{L}_{\text{LFV}} = \frac{m_\mu}{(\kappa + 1)\Lambda^2} \bar{\mu}_R \sigma^{\mu\nu} e_L F_{\mu\nu} + \frac{\kappa}{(\kappa + 1)\Lambda^2} (\bar{\mu}_L \gamma^\mu e_L) (\bar{e}_L \gamma_\mu e_L). \quad (2.1)$$

Herein, Λ denotes the common mass scale and κ the amplitude ratio between the two summands. e and μ are the spinors of the electron and muon, the indices R and L indicate right- and left-handedness. The first term of equation 2.1 represents dipole coupling and thus loop-level decays whereas the second one² describes four-fermion contact action (tree-level decays). The reach in mass scale Λ as a function of κ is shown in figure 2.4. At low κ the loop-level decays are dominant. To exceed the accessible mass range of *MEG*, the *Mu3e* experiment has to overcome the additional $\gamma \rightarrow e^-e^+$ vertex and thus be two orders of magnitude better in sensitivity ($\propto \alpha_{\text{em}}$, the electromagnetic coupling constant). At high κ however, the tree-level decays dominate which cannot mediate $\mu \rightarrow e\gamma$ but $\mu \rightarrow eee$.

²For simplicity reasons the left-left vector coupling is chosen exemplarily.

2 Theory

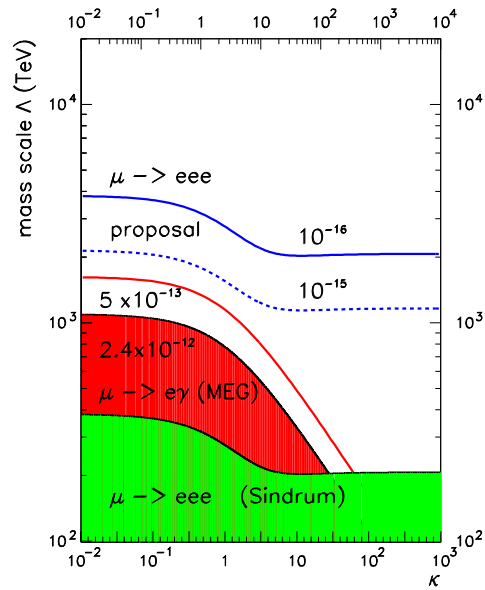


Figure 2.4: Reach in mass scale for the experiments *SINDRUM*, *MEG* and *Mu3e* at the corresponding sensitivities as a function of the occurrence of loop- and tree-level decays (low and high κ respectively). The graphic is taken from [B⁺12]

3 The Mu3e Experiment

The proposed *Mu3e* experiment searches for the lepton flavour violating decay $\mu^+ \rightarrow e^+e^-e^+$ with a sensitivity of one in 10^{16} decays, four orders of magnitude better than previous experiments (see [B⁺12]). In order to reach this goal, high muon rates are required to perform the experiment within a suitable time scale. Furthermore, for an efficient background suppression a detector with high spatial resolution and precise timing information is necessary.

Various muon decays are discussed in this chapter to introduce the signal decay $\mu \rightarrow eee$ and its possible sources of background. Furthermore, the current experimental situation is presented and a general overview of the experiment is given.

Decay Mode	Branching Ratio	Confidence Level
$\mu^+ \rightarrow e^+\bar{\nu}_\mu\nu_e$	$\approx 100\%$	
$\mu^+ \rightarrow e^+\gamma\bar{\nu}_\mu\nu_e$	$(1.4 \pm 0.4)\%$	
$\mu^+ \rightarrow e^+e^-e^+\bar{\nu}_\mu\nu_e$	$(3.4 \pm 0.4) \cdot 10^{-5}$	
$\mu^+ \rightarrow e^+\nu_\mu\bar{\nu}_e$	$< 1.2\%$	90 %
$\mu^+ \rightarrow e^+\gamma$	$< 2.4 \cdot 10^{-12}$	90 %
$\mu^+ \rightarrow e^+e^-e^+$	$< 1.0 \cdot 10^{-12}$	90 %
$\mu^+ \rightarrow e^+\gamma + \gamma$	$< 7.2 \cdot 10^{-11}$	90 %

Table 3.1: Branching ratios of various muon decay modes (values taken from [K. 10, A⁺11])

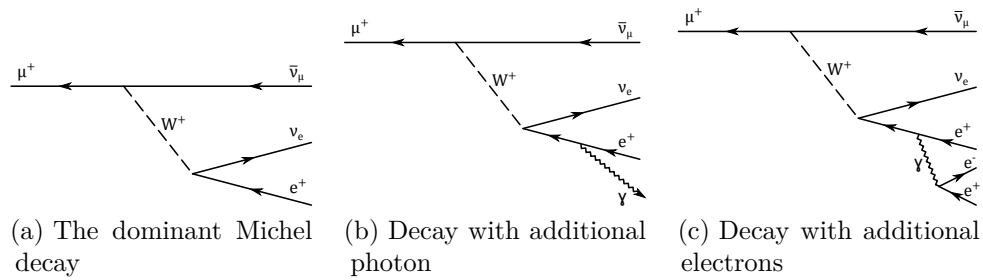


Figure 3.1: Lepton flavour conserving decays of the muon which are allowed in the Standard Model

3.1 The Decay of the Muon

The muon¹ is the charged lepton of the second generation. It has a mass of $m_\mu = (105.658\,367 \pm 0.000\,004) \text{ MeV}/c^2$ and a mean life time of $(2.197\,034 \pm 0.000\,021) \mu\text{s}$ [K. 10]. Because of its small mass and the conservation of the electrical charge it can only decay into electrons, neutrinos and photons.

The following considerations will be limited to the antimuon because the *Mu3e* experiment will use an antimuon beam.

3.1.1 Standard Model Decays

In the Standard Model the lepton flavour is conserved like in the dominant decay mode of the muon, the so-called Michel decay $\mu^- \rightarrow e^- \nu_\mu \bar{\nu}_e$ with a branching ratio of nearly 100 % (see figure 3.1(a)).

Other lepton flavour conserving decays have additional photons or electron positron pairs like $\mu^+ \rightarrow e^+ \gamma \bar{\nu}_\mu \nu_e$ and $\mu^+ \rightarrow e^+ e^- e^+ \bar{\nu}_\mu \nu_e$ (see figures 3.1(b) and (c)). The various decay modes of the muon are summarised in table 3.1.

¹The terms ‘muon’ and ‘electron’ stand – if not denoted differently – for both muons and antimuons and electrons and positrons, respectively.

3.1.2 Lepton Flavour Violating Muon Decays

There are various lepton flavour violating muon decays which are experimentally investigated, like the muon decay into a photon and an electron ($\mu \rightarrow e\gamma$) or muon conversion on nuclei. The muon decay into three electrons ($\mu \rightarrow eee$) is discussed further in the following.

The Decay $\mu^+ \rightarrow e^+e^-e^+$

The $\mu \rightarrow eee$ decay is a prompt decay. All decay electrons originate from a common vertex.

If the muon decays at rest, the vectorial sum of the momenta of the electrons vanishes:

$$|\mathbf{p}_{\text{tot}}| = \left| \sum \mathbf{p}_i \right| = 0. \quad (3.1)$$

Moreover, the total energy of the decay particles has to match the muon mass:

$$E_{\text{tot}} = \sum E_i = m_\mu c^2. \quad (3.2)$$

Thus, the energies of the decay electrons lie within the range of 0 MeV to 53 MeV (half the muon mass $m_\mu c^2$).

The conservation of energy and momentum and the coincidence of the decay particles allow for discrimination between signal and background.

3.2 Current Experimental Situation

Lepton flavour violation is of large interest and therefore various experiments looking for lepton flavour violating processes have been built in the past or are planned in the near future. Current limits on branching ratios for lepton flavour violating muon decays are summarised in table 3.2.

3.2.1 SINDRUM

The *SINDRUM* experiment was operated at the *Paul Scherrer Institute (PSI)* from 1983 to 1986. As *Mu3e*, it was searching for the decay $\mu^+ \rightarrow$

3 The Mu3e Experiment

Decay Channel	Experiment	Limit on Branching Ratio
$\mu \rightarrow e\gamma$	MEGA	$< 1.2 \cdot 10^{-11}$ [B ⁺ 99]
	MEG	$< 2.4 \cdot 10^{-12}$ [A ⁺ 11]
$\mu \rightarrow eee$	SINDRUM	$< 1.0 \cdot 10^{-12}$ [B ⁺ 88]
$\mu \text{Au} \rightarrow e \text{Au}$	SINDRUM II	$< 7 \cdot 10^{-13}$ [B ⁺ 06]

Table 3.2: Limits on branching ratios for lepton flavour violating muon decays and muon-to-electron conversion experiments

$e^+e^-e^+$.

In the absence of a signal, a limit on the branching ratio was set: $\text{BR}(\mu \rightarrow eee) < 10^{-12}$ at 90 % CL [B⁺88].

3.2.2 MEG

The *MEG* experiment searching for $\mu^+ \rightarrow e^+\gamma$ is in operation at *PSI* since 2008 and will continue until end of 2012. Possible upgrades and thus a prolongation are currently under discussion.

The *MEG* experiment sets the current limit on the branching ratio: $\text{BR}(\mu \rightarrow e\gamma) < 2.4 \cdot 10^{-12}$ (90 % CL) [A⁺11]. It can reach a sensitivity of about 10^{-13} for $\mu \rightarrow e\gamma$ and is mainly limited by accidental background.

The decay $\mu \rightarrow eee$ as well is sensitive to lepton flavour violating dipole couplings but because of the additional vertex the sensitivity is reduced by about two orders of magnitude with respect to $\mu \rightarrow e\gamma$. The decay $\mu \rightarrow e\gamma$ instead cannot detect lepton flavour violating four-fermion contact interactions.

3.2.3 Muon Conversion Experiments

The conversion of muons into electrons on nuclei is another possibility for lepton flavour violation tests. An advantage of these tests is the clear signature of monochromatic electrons.

The *SINDRUM II* experiment for example holds the most stringent limits for $\mu \rightarrow e$ conversion on gold (among other nuclei): $\text{BR}(\mu \text{Au} \rightarrow$

$\epsilon(\text{Au}) < 7 \cdot 10^{-13}$ [B+06] .

New experiments testing muon conversion like *Mu2e* [C+08, Tsc11] at *Fermilab* or *DeeMe* [Aok12, Aok10], *COMET* [C+09, Kun10] and *PRISM* [Kun08, PJU+10] at *J-PARC* are planned. They intend to reach sensitivities from 10^{-14} to 10^{-16} or better.

Besides lepton flavour violating dipole couplings also four-fermion couplings can be tested. In muon conversion light quarks are involved and thus these experiments are complementary to other searches for lepton flavour violation.

3.3 Sources of Background

Given a sufficiently high number of muon stops, the final sensitivity of the experiment is determined by how well the signal events can be discriminated from the background. For the *Mu3e* experiment, there are two types of backgrounds. One is the accidental or combinatorial background, so the random coincidence in time and space of three electrons from different processes which is misidentified as a signal decay. The probability for accidental background increases with the intensity of the muon beam.

The second source of background is the inevitable background from muon decays into three electrons with additional particles like $\mu^+ \rightarrow e^+e^-e^+\bar{\nu}_\mu\nu_e$.

3.3.1 Accidental Background

In the accidental background, two positrons and an electron from different processes look like the signal event (see figure 3.2). For example, the positrons can originate from Michel decays and the electron can be mimicked by a positron – for example from a recurling track – whose charge has been misidentified. The electron in this scenario can also come from Bhabha scattering, a muon decay with internal conversion or a photon conversion process. For instance, these photons can be produced by the

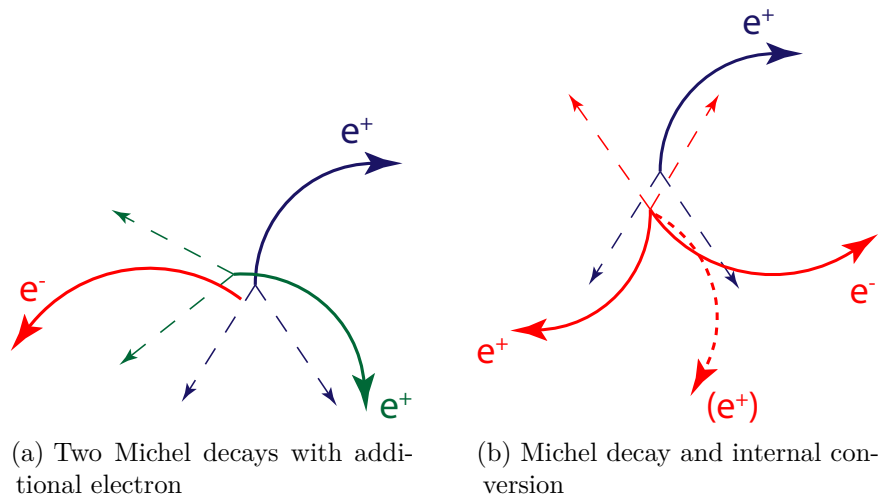


Figure 3.2: Sources of accidental background. The straight dashed lines indicate neutrinos

radiative muon decay $\mu^+ \rightarrow e^+ \gamma \bar{\nu}_\mu \nu_e$. The probability of photon conversion can be reduced if the material amount in the detector is minimised.

The processes involved in accidental background are neither coincident in time nor do they share a common vertex or fulfil the criteria of momentum and energy conservation (see equations 3.1 and 3.2). Thus, this source of background can be drastically reduced by a good vertex, time and momentum resolution.

3.3.2 Background Due to Internal Conversions

The muon decay with internal conversion is a radiative muon decay with the radiated photon immediately decaying into an electron-positron pair: $\mu^+ \rightarrow e^+ e^- e^+ \bar{\nu}_\mu \nu_e$. It is a Standard Model decay with a branching ratio of $(3.4 \pm 0.4) \cdot 10^{-5}$ [K. 10].

In contrast to the accidental background, all decay particles are coincident in time and share a common vertex. The internal conversion process is therefore the most severe source of background for the *Mu3e* experiment. As the neutrinos cannot be detected in the *Mu3e* detector, the conservation

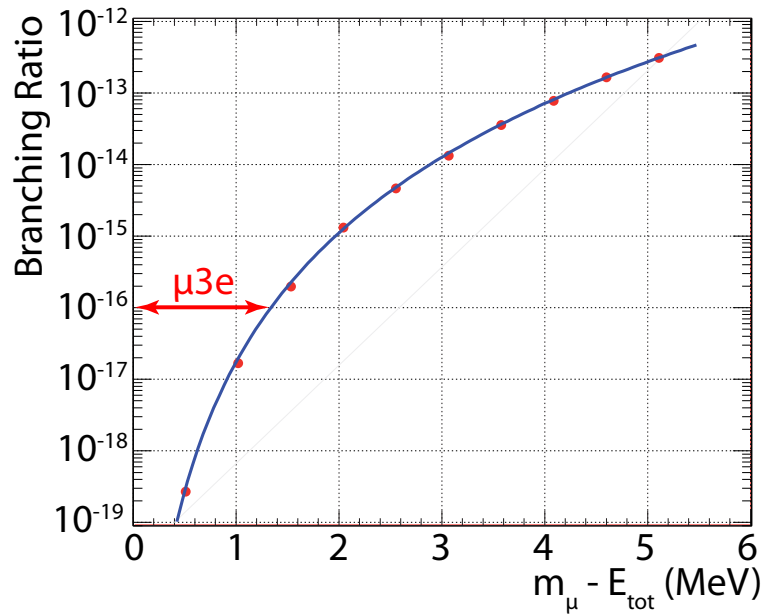


Figure 3.3: Effective branching ratio as a function of missing energy due to the neutrinos (figure taken from [DK09])

of momentum and energy is not fulfilled which can be utilised to suppress the background due to internal conversion processes.

Figure 3.3 shows the branching ratio of the process $\mu \rightarrow ee\nu\nu$ as a function of the missing energy $m_\mu c^2 - E_{\text{tot}}$ ². For the projected sensitivity of 10^{-16} for the *Mu3e* experiment, a momentum resolution for the sum of the three electron momenta of below 1 MeV is required.

The radiative muon decay $\mu^+ \rightarrow e^+ \gamma \bar{\nu}_\mu \nu_e$ has to be considered as well as a source of background if the photon converts in the target region. These events have the same signal topology as the internal conversion events.

3.4 The Concept of the Mu3e Experiment

The *Mu3e* experiment faces a lot of challenges to reach a sensitivity in branching ratio of $< 10^{-16}$ (see [B⁺12]). It needs very high muon rates

² E_{tot} is the sum of the energies of the electrons. The neutrinos are not included.

3 The *Mu3e* Experiment

which in the final sensitivity phase will exceed the currently available rates. The detector must not only be able to deal with such a high particle rate but has also to provide high spatial and time resolution in order to suppress the background below a level of $< 10^{-16}$. Consequently, the total material amount in the active detector volume has to be kept at a minimum to reduce multiple scattering.

As electrons and positrons represent the only decay products of the muon which can be seen in the detector no particle identification has to be performed.

3.4.1 The Muon Beam

The *Mu3e* experiment will be operated in two phases with different muon rates.

In the first phase from 2014 to 2017 the aim is to reach a sensitivity of $\text{BR} \sim \mathcal{O}(10^{-15})$. Therefore, a muon stopping rate of about $2 \cdot 10^8$ Hz is required. Such a high muon rate is available at the *PSI*. It has the world's most intense proton beam with up to 2.3 mA of 590 MeV/ c protons. The proton beam is used to produce pions in a rotating carbon target. A surface muon beam results from pions at rest which decay very close to the target surface.

Sufficiently high muon rates are available at the $\pi E5$ beamline which is a secondary beamline after the second and thicker target E (see figure 3.4). Currently, this beamline is used by the *MEG* experiment.

In the second phase from 2017 on the *Mu3e* experiment plans to reach its final sensitivity of $\text{BR} \sim \mathcal{O}(10^{-16})$. This requires muon stopping rates of about $2 \cdot 10^9$ Hz and thus the construction of a new muon beamline. High numbers of protons are stopped in the neutron spallation source *SINQ*³ target and so large amounts of muons are generated. The feasibility of a secondary beamline originating from the *SINQ* target is currently under study.

³Swiss Spallation Neutron Source , *PSI*

3.4 The Concept of the Mu3e Experiment

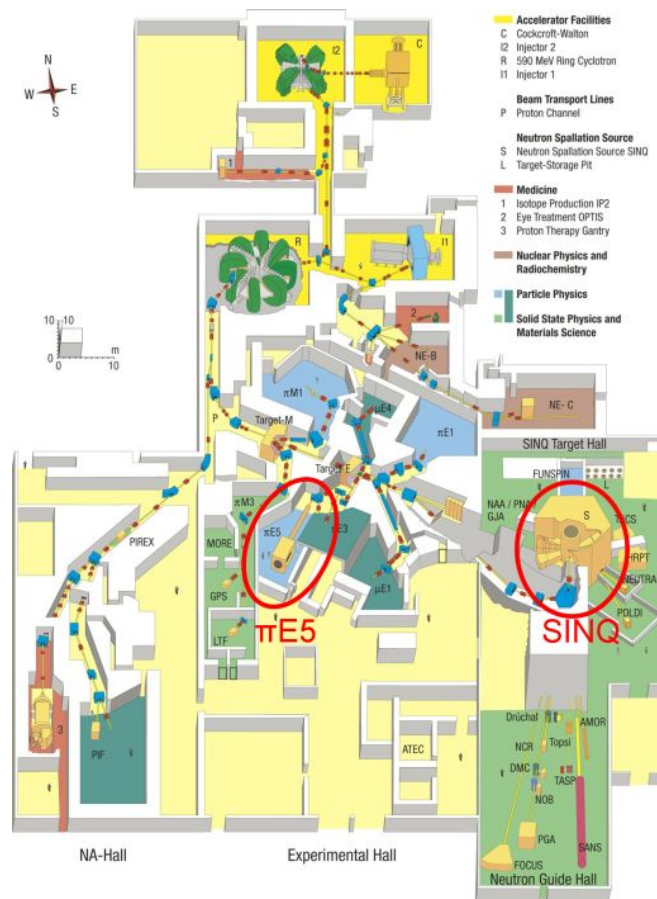


Figure 3.4: The experimental hall at *PSI*. $\pi E5$ and *SINQ* are highlighted by the red ellipses

3 The *Mu3e* Experiment

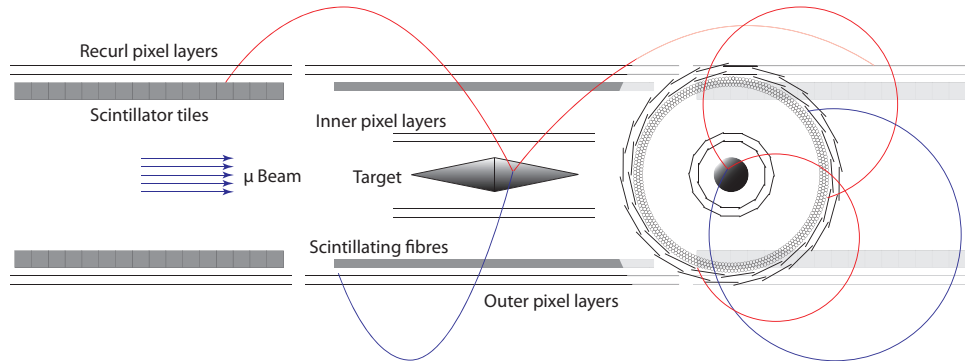


Figure 3.5: Design of the *Mu3e* detector with a signal event. The longitudinal profile with half of each recurl station is visible. The transverse view is overlaid.

3.4.2 The Target

The muons from the beam are then stopped in the target. The target should be constructed such that the muons are stopped uniformly over a large surface in order to separate the individual vertices. Moreover, the decay electrons should see only a minimal amount of target material.

In the current design the target consists of a thin hollow double cone made of aluminium with a length of 100 mm and a radius of 20 mm, similar in shape to the *SINDRUM* target. The aluminium should be thinner than 60 μm .

3.4.3 The Design of the *Mu3e* Detector

In the *Mu3e* experiment the requirements on the detector are relatively tough to achieve the necessary background suppression below a level of 10^{-16} . The detector should have a high vertex, momentum and time resolution and should be able to deal with the high muon rates. Moreover, a high acceptance and efficiency and a minimal material amount to avoid multiple scattering is desired.

3.4 The Concept of the *Mu3e* Experiment

The baseline design of the *Mu3e* detector is depicted in figure 3.5. It has a cylindrical shape with a length of about 2 m and a diameter of about 20 cm. It is divided up into a central part surrounding the target and outer parts on both sides of the central detector – the so-called recurl stations – and it basically consists of a tracking and a timing detector.

The Tracking Detector

The main component of the detector is a tracking detector based on silicon pixel sensors. As the whole detector will be located in a solenoidal magnetic field with a field strength of about $(1 - 1.5)$ T, the momentum of the decay particles can be determined by the curvature of their trajectories.

The tracking detector in the central detector region consists of two double layers of silicon pixel sensors. As the sensor itself is plane, the layers are constructed as prisms with different numbers of sides for the various radii. Details of the geometry are given in table 3.3. The inner prisms are shorter and placed closely to the target. Whereas the outer ones are longer and at larger radii. The choice of the radii has direct influence on the acceptance and momentum resolution. The detector is optimised for electrons with energies between 10 MeV and 53 MeV.

As charged particles have a helical trajectory in a magnetic field, they return – in the projection plane transverse to the magnetic field lines – to their origin. Thus, the momentum resolution can be increased by measuring these recurlers as well. Therefore, additional pixel detectors are installed upstream and downstream from the central detector. The recurl stations have the same radii as the outer double layer of the central detector but are twice as long.

The pixels will have a size of $(80 \times 80) \mu\text{m}^2$ which results in a total number of about 300 million pixels.

The final momentum resolution of the *Mu3e* experiment is limited by multiple scattering. Charged particles that traverse a medium get deflected by electromagnetic interactions with the large number of nuclei of the material. They leave the medium with a displacement and a kink angle with

3 The Mu3e Experiment

Detector part	Reticle [cm ²]	Prism	Radius [cm]	Length [cm]
Inner central	1 × 6	12- & 18-sided	1.90 & 2.86	12
Outer central	2 × 6	24- & 28-sided	7.63 & 8.90	36
Recurl station	2 × 6	24- & 28-sided	7.63 & 8.90	2 × 36

Table 3.3: Geometry of the elements of the tracking detector

respect to the initial trajectory. For small deflection angles a Gaussian distribution can be assumed with a standard deviation for the kink angle in a plane of

$$\theta_{\text{RMS}} = \frac{13.6 \text{ MeV}}{\beta cp} \sqrt{\frac{x}{X_0}} \left[1 + 0.038 \ln \left(\frac{x}{X_0} \right) \right]. \quad (3.3)$$

Herein, β denotes the velocity of the electron in units of the speed of light c , p the momentum, x the thickness of the traversed medium and X_0 the radiation length (see equation 4.7). Thus, the multiple scattering gets more severe for particles with relatively low momentum like the electrons in the *Mu3e* experiment. It can only be reduced by using materials with high radiation lengths and by reducing the material amount in the active detector volume to a minimum.

Therefore, the pixel detector will consist of thinned silicon pixel sensors (for more details see section 4.3) and a mechanical support structure basically made of Kapton®. The thin pixel sensor ($\sim 35 \mu\text{m}$) will be wire-bonded to a flexprint (25 μm Kapton®, $\sim 50\%$ covered by 15 μm thick aluminium traces) and glued to a prism made of 25 μm thin Kapton® foil. Such a pixel detector becomes comparable to gaseous detectors in terms of radiation lengths.

Paper models and prototypes made of Kapton® and 50 μm glass plates turn out to be surprisingly stable and stiff (see figure 3.6).

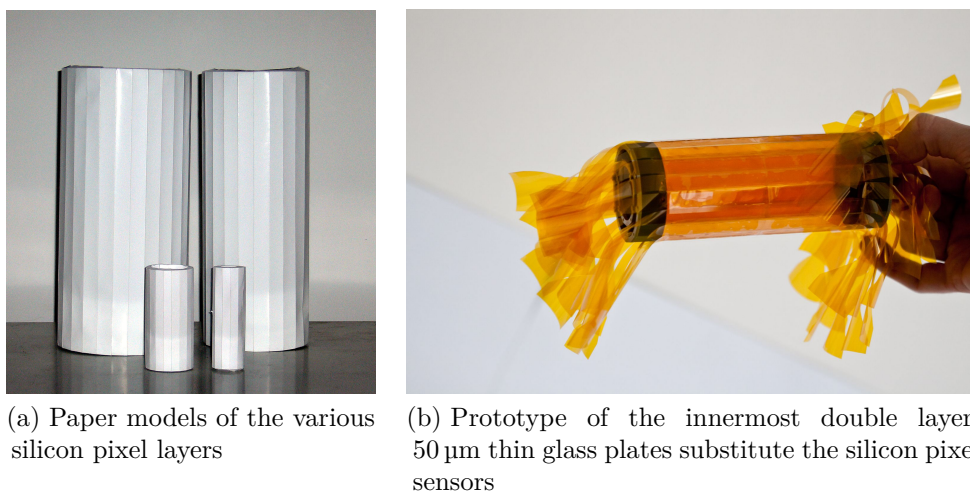


Figure 3.6: Mechanical prototypes

The Timing Detector

The pixel sensors provide the required spatial resolution and thus vertex and momentum resolution but for a good time resolution an additional timing detector is needed.

In the central detector at the inner surface of the outer double layer three to five layers of scintillating fibres will be placed. Their time resolution is expected to be less than 1 ns.

The recoil stations will be equipped with scintillating tiles. Since here multiple scattering is no longer a problem – the electrons may also get stuck in the tiles – more material can be used for the benefit of a system with more precise timing information. The tiles have an expected time resolution of about (0.1 – 0.2) ns.

4 Pixel Sensors for Mu3e

The *Mu3e* tracking detector is based on a special kind of silicon pixel sensors, the so-called *HV-MAPS*¹. These sensors have several advantages like fast charge collection and the possibility to thin them down to a fraction of the original wafer thickness. Thus, they are of large interest for the *Mu3e* experiment.

Before the principle of the *HV-MAPS* is explained basic information about semiconductors and the interactions of electrons with matter is given.

4.1 Silicon as a Semiconductor

Semiconductor detectors are often built of silicon or germanium. As the pixel sensors in the *Mu3e* experiment are made of silicon, the following discussions will only treat silicon. Its basic properties are summarised in table 4.1.

Silicon has a diamond crystal structure (see figure 4.1). Each atom has four covalent bonds to neighbouring atoms. The energy band structure of silicon is shown in figure 4.2. The valence and conduction band are separated by a band gap energy of about $E_g = 1.12 \text{ eV}$ [SN07] which is typical for a semiconductor. At a temperature $T = 0 \text{ K}$ all valence electrons participate in the covalent bonding of the atoms. At room temperature, for example, some electrons can be thermally excited to the conduction band and holes are left in the valence band. Another electron of the valence band can occupy this position leaving behind a hole at its initial position. This looks like as if the hole ‘moves’ in the crystal acting like a positive

¹High Voltage Monolithic Active Pixel Sensors

Crystal Structure		Diamond
Band gap E_g	at 300 K	1.12 eV
	at 0 K	1.17 eV
Band		Indirect band gap
Mobility at 300 K	μ_n	1.450 cm ² s/V
	μ_p	500 cm ² s/V
Atomic number	Z	14
Nucleon number	A	28.09
Atom density		5.02 · 10 ²² /cm ³
Dielectric constant		11.9

Table 4.1: Some important properties of silicon (values taken from [SN07])

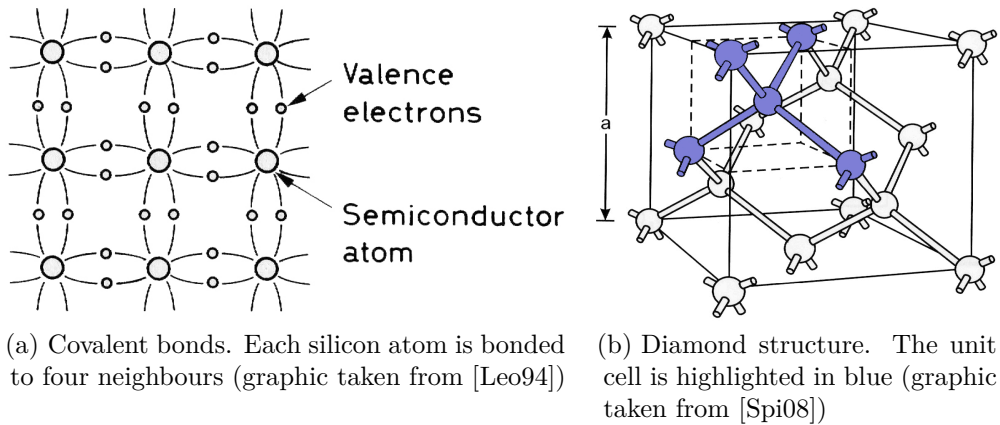


Figure 4.1: Bonds and lattice structure of silicon

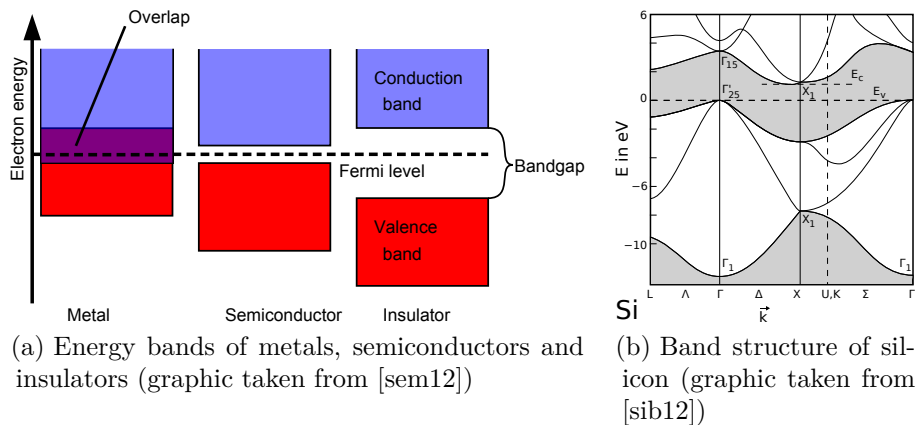


Figure 4.2: Energy band structure of semiconductors

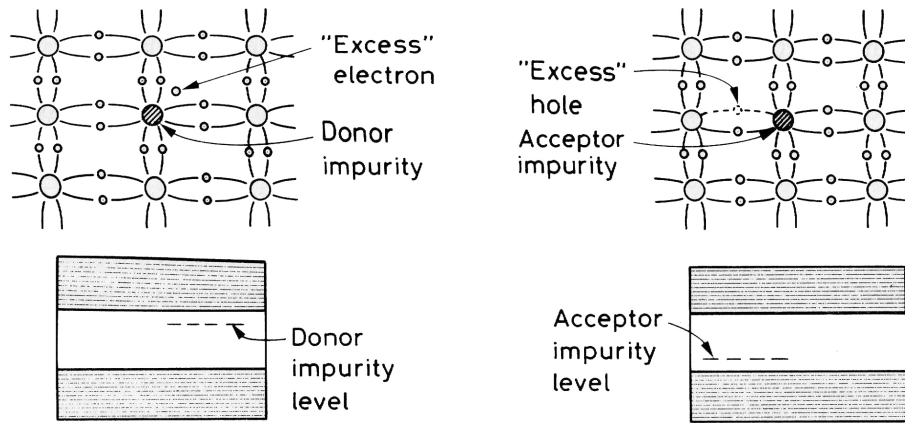


Figure 4.3: N- and P-doping in silicon (graphic taken from [Leo94])

charge carrier. In this way, a small current can flow when an external voltage is applied due to the movement of electrons as well as holes. However, the concentration of electron-hole pairs at $T = 300\text{ K}$ in silicon is about $n_i \approx 1.5 \cdot 10^{10}/\text{cm}^3$ and thus much smaller than the concentration of atoms ($5.02 \cdot 10^{22}/\text{cm}^3$) leading to a negligible current compared to effects due to impurities.

The conductivity of a semiconductor can be increased by introducing impurity atoms into the lattice, the so-called doping (see figure 4.3). Pentavalent atoms like arsenic, phosphorus or antimony have an additional valence electron that does not participate in a covalent bond with the silicon atoms. Thus, an discrete energy level is created close to the conduction band. These electrons can be easily excited to the conduction band. Such dopants are called donors and materials doped this way n-doped as the negative electrons are the majority charge carriers. If, on the other hand, trivalent atoms, called acceptors, like gallium, boron or indium are introduced, the silicon has an excess of holes leading to the creation of an acceptor energy level close to the valence band. Electrons of the valence band can be easily excited to this extra energy level, leaving holes behind. As the holes are the majority charge carriers, such material are called p-doped.

Semiconductor detectors are normally based on diodes formed by a pn-

junction. The electrons and holes of the n- and p-doped side drift to the other side of the junction and recombine with their counterparts, creating a zone without mobile charge carriers, the so-called depletion zone. Detailed calculations can be found in the appendix (see appendix 1).

Charged particles and photons that traverse a semiconductor lose energy in the material. A part of the deposited energy leads to the excitation of electrons from the valence band into the conduction band. The average energy for the creation of an electron-hole pair in silicon is 3.62 eV at $T = 300$ K [Leo94]. A non-negligible part of the energy goes into the creation of phonons. As silicon is an indirect semiconductor, the creation of an electron-hole pair at the lowest energy transfers always involves phonons.

4.2 Interactions of Electrons and Positrons with Matter

The detection of particles is based on interactions of the particles with the detector material. Almost all detectors are based on electromagnetic interactions. Many particles lose a part or all of their energy by ionisation processes, the most frequently used process for particle detection. These particles are called ionising radiation. The energy loss releases charge carriers – always in pairs of positive and negative charge because the electrical charge is a conserved quantity – or photons which can be converted to an electronically processable signal.

The *HV-MAPS* sensor as well is based on the production of electron and hole pairs by electromagnetic interactions of the incident particles with the silicon.

In the *Mu3e* experiment, the only relevant particles are electrons and positrons with energies in the range of (10 – 53) MeV. They will basically lose energy by two processes: inelastic Coulomb collisions on the one hand,

and bremsstrahlung on the other hand. Thus, the mean energy loss per unit path length reads as follows

$$-\frac{dE}{dx} = -\left(\frac{dE}{dx}\right)_{\text{coll}} - \left(\frac{dE}{dx}\right)_{\text{brems}}. \quad (4.1)$$

4.2.1 Collision Stopping Power

Particles can transfer part of their energy by inelastic collisions to the shell electrons of the atoms in the medium leading to ionisation or excitation of the atoms. In some ionisation processes, the amount of transferred energy is high enough that the liberated electron itself, the so-called δ -electron, can perform secondary ionisation.

For most of the particles, the energy loss via inelastic collision processes can be described by the Bethe-Bloch formula. However, this formula needs some modifications if applied to electrons or positrons. These particles are much lighter than for example the muon whose collision stopping power is well described by the Bethe-Bloch formula. Moreover, the incident electrons are quantum-mechanically indistinguishable from shell electrons of the atoms of the medium. This leads to differences in the stopping power for electrons and positrons. Consequently, the Berger-Seltzer formula has to be used while treating electrons or positrons as it accounts for these phenomena.

In the energy range of (10 – 53) MeV the Berger-Seltzer formula reads as follows [SB84, SB82]

$$-\left(\frac{dE}{dx}\right)_{\text{coll}} = \rho \frac{0.153536 Z}{\beta^2} \frac{1}{A} B(T). \quad (4.2)$$

Herein, ρ is the density of the medium in g/cm^3 , β the velocity of the incident particle in units of the speed of light c , Z the atomic number and A the nucleon number of the medium, and $B(T)$ the stopping number as

Atomic number Z	14
Nucleon number A	28.0855
Density ρ [g/cm ³]	2.330
b_1	19.4167
b_2	4.6215
b_3	13.2240
k	3.2546

Table 4.2: Quantities of silicon [SB84, SB82]

a function of the kinetic energy T of the incident particle.

The stopping power is given by the following formula

$$B(T) = B_0(T) + 1 - 2 \ln(p/mc) + b_1 - b_2 \left[1 - \frac{2 \ln(p/mc)}{b_3} \right]^k \quad (4.3)$$

$$\text{for } e^-: B_0(T) = \ln \left(\frac{\tau^2(\tau + 2)}{2} \right) + \frac{1 + \tau^2/8 - \ln(2)(2\tau + 1)}{(\tau + 1)^2} \quad (4.4)$$

$$\begin{aligned} \text{for } e^+: B_0(T) &= \ln \left(\frac{\tau^2(\tau + 2)}{2} \right) + 2 \ln(2) \\ &- \frac{\beta^2}{12} \left(23 + \frac{14}{\tau + 2} + \frac{10}{(\tau + 2)^2} + \frac{4}{(\tau + 2)^3} \right), \end{aligned} \quad (4.5)$$

with the momentum p of the incident particle, the electron mass m , $\tau = \frac{T}{mc^2}$, the material constants b_1 , b_2 and b_3 and the fit parameter k . The values for silicon are given in tabular 4.2. For the *Mu3e* experiment, the energy losses due to ionisation are of the order of 4 MeV/cm = 0.4 keV/ μ m (see figure 4.4).

4.2.2 Bremsstrahlung

Charged particles that traverse a medium get also deflected in the electric field of the nuclei. Thus, the electrons lose part of their energy by radiating photons. This process is called bremsstrahlung. As electrons and positrons are very light, they are affected by bremsstrahlung. For other particles however, bremsstrahlung effects can be neglected.

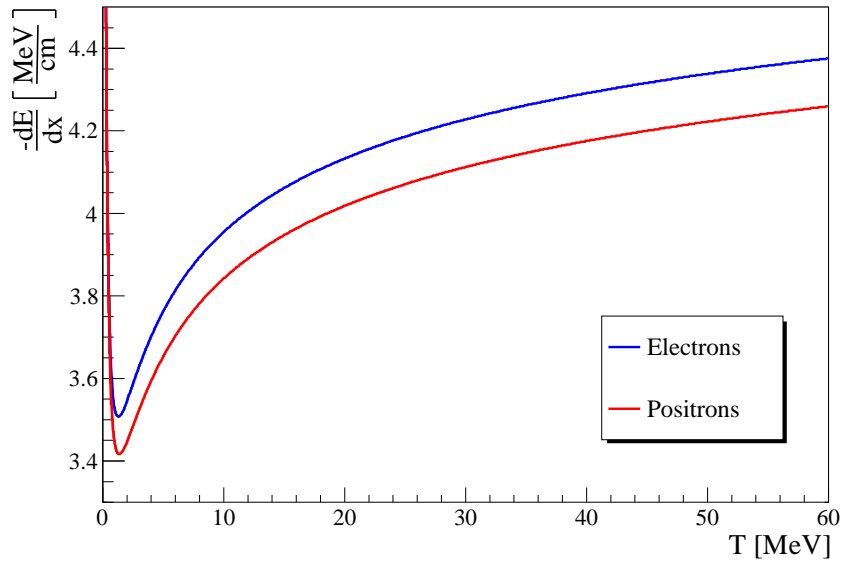


Figure 4.4: Energy loss due to inelastic collisions for electrons and positrons respectively obtained with the Berger-Seltzer formula

The electrons and positrons in the *Mu3e* experiment can be regarded as relativistic. In this case, the bremsstrahlung effects are characterised by the radiation length X_0 which is the mean distance over which the particle's energy has declined to $1/e$ of its initial energy due to bremsstrahlung (see [Leo94])

$$-\left(\frac{dE}{dx}\right)_{\text{brems}} = \frac{E}{X_0}. \quad (4.6)$$

The radiation length can be approximated by

$$X_0 = \frac{1}{\rho} \frac{716.4 \text{ g/cm}^2 A}{Z(Z+1) \ln(287/\sqrt{Z})}. \quad (4.7)$$

The radiation length for silicon is about 9.5 cm.

The combined energy loss by inelastic collisions and bremsstrahlung for electrons and positrons is drawn in figure 4.5.

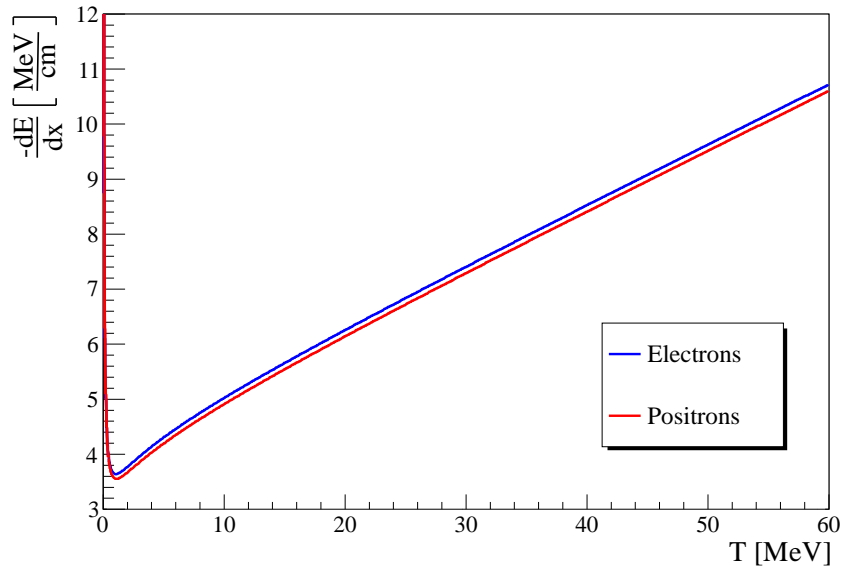


Figure 4.5: Energy loss due to inelastic collisions and bremsstrahlung for electrons and positrons respectively

4.3 HV-MAPS

The $Mu3e$ experiment requires a silicon pixel sensor that is fast on one hand to be able to deal with the high muon rates and that has a minimal amount of material on the other hand.

Standard hybrid pixel sensors – as for example used in the CMS pixel detector upgrade [Hus12] – are no suitable choice for the $Mu3e$ experiment. They have an additional readout chip that is bump-bonded to the actual sensor, a far too large material amount for $Mu3e$.

Monolithic Active Pixel Sensors (MAPS, see [DD10]) pursue a different strategy. Their readout electronics are – at least partly – located inside the individual pixels. An additional readout chip is therefore not needed. MAPS rely on an epitaxial layer in which the incident radiation generates charge carriers that are then collected via diffusion.

The current pixel sensor prototypes $MuPix1$ and $MuPix2$ (see section 5.1) that are characterised in this thesis however are so-called *High Voltage*

*Monolithic Active Pixel Sensors (HV-MAPS)*². Similar to the *MAPS* they have integrated electronics and do not need an extra readout chip.

HV-MAPS are produced in a commercial high-voltage CMOS process, a standard technology that is inexpensive and highly available. On a p-doped substrate the pixels are implemented as n-doped wells. This diode is then reversely biased by more than 50 V³ leading to the creation of a depletion zone. Inside the deep n-well low-voltage PMOS and NMOS – in an additional p-well – transistors are placed, building the pixel electronics, e. g. a charge sensitive amplifier (CSA). This type of diode is therefore called “smart diode” as it is capable of signal processing. Despite the relatively large bias voltage between n-well and p-substrate, these transistors are all on the same potential (“floating logic”).

An ionising particle traversing the sensor generates electron-hole pairs. The charges generated in the depletion zone are separated in the high electric field and drift towards the electrodes, namely n-well and substrate. This causes a slight voltage drop at the n-well. The first step of signal processing on the pixel is amplification. The input of the CSA that is AC-coupled to the n-well senses this voltage drop and can amplify the signal which is then digitised in the sensor periphery.

The principle of the *HV-MAPS* is illustrated in figure 4.6.

The pixels are placed such that their depletion zones overlap resulting in a fill factor of nearly 100%.

The main portion of the signal is due to the charge carriers generated in the depletion zone. Here the charge collection happens via drift, which is much faster than the diffusion used in the *MAPS* concept. The *HV-MAPS* can therefore have a faster response and achieve a better time resolution.

It also means that the sensor can be thinned because most of the substrate material does not contribute to the charge collection. As the depletion

²Developed by Ivan Perić, *ZITI* Mannheim, see [Per07, PKF10, PT10, PTB⁺10, Per12a, Per12b]

³This voltage is relatively high compared to voltages used in standard *MAPS*. As it is colloquially called “high voltage”, this expression will be used in the following even though this voltage does not exceed 100 V.

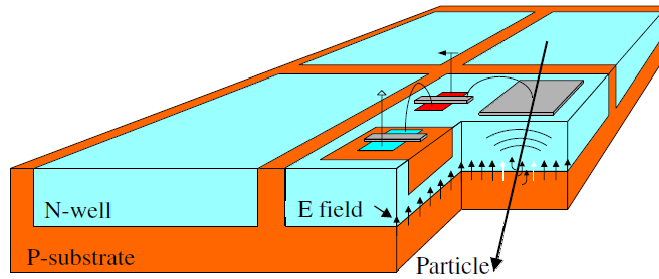


Figure 4.6: Principle of a *HV-MAPS*. Four pixels are shown (graphic taken from [Per07]).

zone is about $10\ \mu\text{m}$ thick (see section 5.1) thinning down to $(30 - 50)\ \mu\text{m}$ seems possible and thus the total material amount in the detector can be enormously reduced.

Even though it is not important for the $Mu3e$ experiment, the *HV-MAPS* is also radiation tolerant because of its small active volume, the high drift speed and the use of PMOS transistors [PKF10].

Part II

**Characterisation of the MuPix
Sensor**

5 The Experimental Setup

For the future tracking detector of the *Mu3e* experiment small prototypes of the silicon pixel sensors have been built in the *HV-MAPS* technology. This chapter gives an overview about the experimental setup used for their characterisation. Emphasis is laid on the description of these prototypes.

5.1 The Prototypes MuPix1 and MuPix2

During this thesis two *HV-MAPS* prototypes for the *Mu3e* pixel detector have been tested: the *MuPix1* (2010) and *MuPix2* (2011) from a later submission (see [Per12a]). The *MuPix1* and *MuPix2* differ only slightly. The major difference is a temperature measurement diode that the *MuPix2* has as additional feature.

Ionising radiation hitting the *MuPix* sensor creates electron-hole pairs. The charges generated in the depletion layer between p-substrate and the n-wells of the pixels are collected by the individual pixels. As the total amount of charge is relatively small, the signal needs to be amplified. A threshold condition is applied in order to distinguish particle hits from noise.

The prototypes have two operation modes. In the hit-flag mode, the hit information of every pixel is read out for the entire pixel matrix. This is binary information, which simply indicates whether or not the pixel has seen a signal that exceeded the threshold. It can be used to determine the distribution of hits over the sensor. The ToT mode is used to probe a single pixel channel. It provides the additional timing information, i. e. how long the signal was above threshold (time over threshold, ToT) and thus information about the amount of generated charge and so the deposited

5 The Experimental Setup

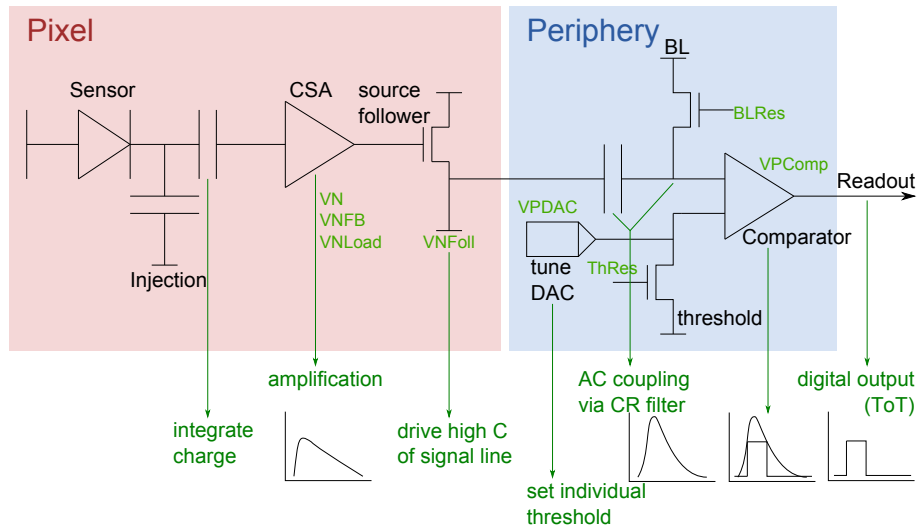


Figure 5.1: Electronics of the *MuPix* inside the pixel and on the chip periphery. The bias voltages that can be changed to improve the performance are highlighted in green

energy. Unfortunately, in the current design this is only possible for a single but freely selectable pixel.

Each sensor consists of two parts: the pixel matrix itself, where basically the analogue signal processing happens, and the chip periphery, where the signals get digitised. This is illustrated in figure 5.1.

The pixels are implemented as smart diodes in the 180 nm AMS¹ HV CMOS technology (see section 4.3). The sensor diode is coupled via a capacitor to the input of the CSA. The sensor signal can also be mimicked for test purposes by the injection capacitor. This test pulse is distributed to all pixels in the matrix. After pre-amplification, the signal passes a source follower that is necessary to drive the capacitance of the signal line from the pixel to its digital processing unit (DPU).

Each pixel has its own DPU in the chip periphery. The signal is AC-coupled via a CR filter to the input of a comparator. This stage compares the signal amplitude to a certain threshold voltage and outputs a digital signal, whose width depends on the signal amplitude and thus the charge

¹austriamicrosystems

5.1 The Prototypes MuPix1 and MuPix2

amount generated in the pixel (ToT).

The global threshold voltage is the same for all pixels in the matrix. As every pixel has its own CSA, the amplification varies slightly from pixel to pixel. Moreover, the offsets of the comparators differ slightly. In order to even out these non-uniformities, a tuning circuit has been implemented to allow individual fine adjustment of the threshold for each pixel. The threshold input line has an additional transistor. The voltage across this transistor is controlled via a 4 bit tune DAC (digital to analogue converter) and adds up to the global threshold voltage.

If the sensor is operated in the ToT mode, the output of the comparator of a single pixel is multiplexed to a test pad. In the hit-flag mode, the comparator output enables the storage of the state of a trigger signal (active is zero) in a flip-flop (hit-flag). If the sensor is hit by a particle (and the amount of generated charges is high enough so that the signal can pass the threshold) and the trigger is active, the hit-flag becomes one. The whole pixel matrix is then row-wise read out and afterwards the hit-flags are deleted.

The CR filter together with the source follower of the pixel electronics form a CR-RC filter – a typical filter used in pulse shaping. Pulse shaping basically reduces the bandwidth and improves thus the signal-to-noise ratio (SNR). The CR-RC filter is further discussed in appendix 2.

The performance of the sensor can be influenced by changing the various bias voltages, for example in order to optimise the timing performance or to adjust the range of the additional tuning voltage that can be generated by the tune DACs.

Furthermore, the chip features a global bias block that provides most of the required bias voltages, registers for configuration and readout and input-output (IO) pads.

The prototypes have a matrix of 42×36 pixels of $(39 \times 30) \mu\text{m}^2$ size and thus a sensitive area of about $(1.6 \times 1.1) \text{mm}^2$. Consequently, the periphery has a matrix of 42×36 DPUs.

The n-well has a dopant concentration of $N_D \approx 1 \cdot 10^{17} / \text{cm}^3$ and the

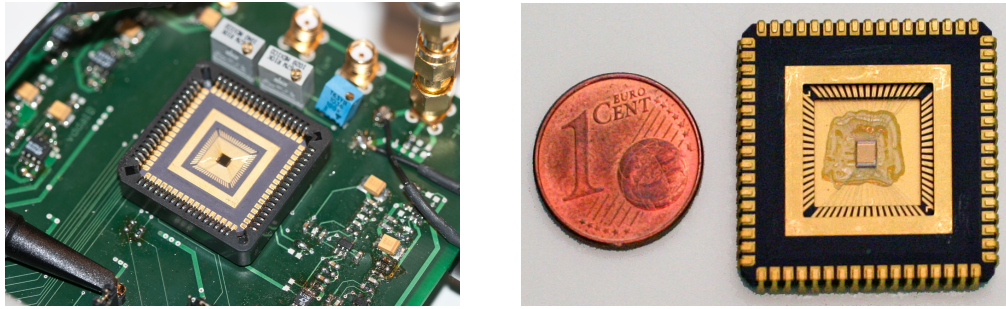


Figure 5.2: Photographs of the *MuPix* prototype

p-substrate of $N_A \approx 1 \cdot 10^{15} / \text{cm}^3$. This leads to a depletion depth of about $d \approx 9 \mu\text{m}$ at a bias voltage of $U_B = 60 \text{ V}$. An electron of about 30 MeV that traverses the sensor vertically has an energy loss of about $\frac{dE}{dx} \approx 0.75 \text{ keV}/\mu\text{m}$ and generates approximately 2000 electron-hole pairs in the depletion layer. The collection time is fast (approximately $t_C \approx 90 \text{ ps}$), which results in a transverse diffusion of $\sigma_{\text{transverse}} \approx 0.8 \mu\text{m}$ at 300 K.

5.2 The Setup

The complete setup for testing and characterising the *MuPix* sensor is very compact. The main components are a printed-circuit board (PCB) hosting the sensor and a FPGA board (field programmable gate array) called Uxibo (USB Xilinx Board, see [uxi12]) that is connected to a computer or laptop (see figures 5.3, 5.4 and 5.5).

The sensor itself is wire-bonded to a ceramic carrier which can be placed in a socket on the PCB (see figure 5.2). Thus, the various sensors can be exchanged easily. The PCB basically provides the required voltages: The low input voltage of +5 V is converted to 1.8 V and 3.3 V for the internal electronics and there is an adaptor for the negative high voltage necessary to create the depletion layer. The high voltage can be either provided by a power supply or by an array of batteries which is more stable, but has only a fixed voltage. The PCB is connected to the Uxibo via a flat ribbon cable.

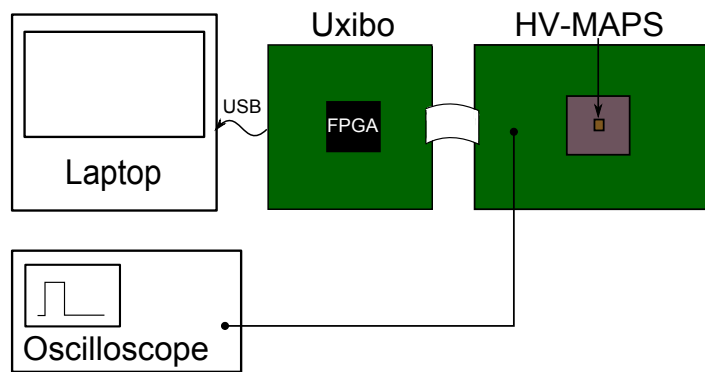


Figure 5.3: Schematic of the setup

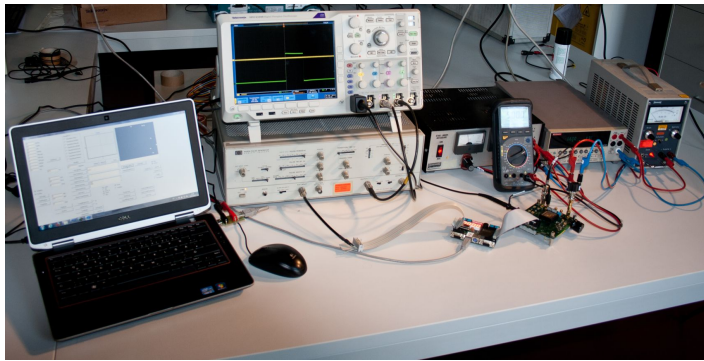


Figure 5.4: Complete experimental setup in the laboratory

On the other side the Uxibo is connected to a computer via USB. It is responsible for the communication with the sensor. It does configuration and reads out the data. The Uxibo has a second adaptor for a flat ribbon cable which can be used to monitor different signals of interest like the internal trigger or to put in signals like the gate for testbeam measurements. The Uxibo as well needs to be powered by 5 V.

The sensor is controlled via a computer program based on C++ (see figure 3 in the appendix). The various functions are explained in appendix 3.

Additionally, the ToT signal can be tapped directly at the PCB and for example observed on an oscilloscope.

5 The Experimental Setup

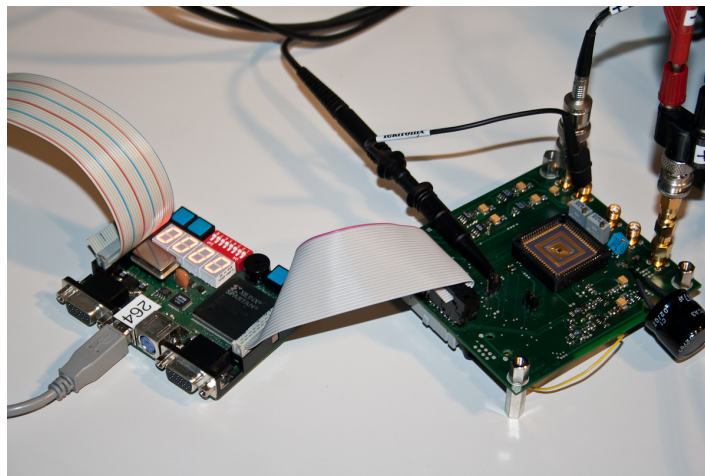


Figure 5.5: Uxibo (left) and PCB with sensor (right). The connected flat cables, USB cable and power supply cables as well as the probe for the oscilloscope can be seen.

6 Measurements with Injection Pulses

Before tests of the *MuPix* sensor with real particles like electrons or photons are discussed, the measurements with internally generated test pulses are presented.

As shown in figure 5.1, the signal of the detector diode resulting from real particle hits can also be mimicked by an injection pulse via an additional capacitor placed inside the pixel n-well. In this way, the electronics, e. g. the CSA and shaper, can be tested by well-known test pulses.

6.1 Injection-Scan for a Single Pixel

Ideally, the single pixels would detect a hit as soon as the signal is above threshold and would reject it already if it is just slightly below. But noise leads to small fluctuations and thus enables signals to surpass the threshold even if their amplitudes are actually too small.

This behaviour can be studied for a single pixel by a method called ‘injection-scan’. Starting with a relatively large test pulse, which causes a signal that is, after amplification and shaping, definitely above threshold, a series of test pulses is generated. The software then counts how many pulses are actually detected. This procedure is repeated for lower and lower injection pulses until no pulse of the series is detected. A typical histogram of such an injection-scan is shown in figure 6.1.

Without noise this histogram would look like a step-function: all pulses that are lower than the threshold are not detected but 100% of the pulses above threshold. In reality, the sharp edge of the step-function is blurred by noise. This is best described by an error function. The resulting width (σ) of the fit is a measure of the noise. Figure 6.2 shows the mean value and

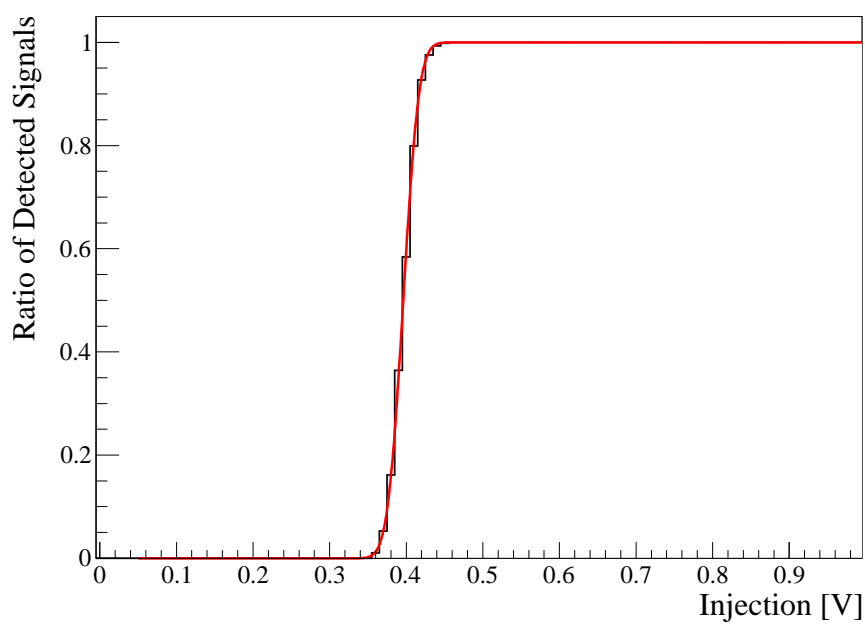


Figure 6.1: Histogram of an injection-scan of a central pixel. The ratio of detected signals is plotted against the amplitude of the injection pulse. The applied error function fit is shown by the red line

6.1 Injection-Scan for a Single Pixel

width of the error function fits for injection-scans at various thresholds. The mean value represents the position at which 50% of the pulses are detected. As expected, the edge of the error function is shifted to higher injection voltages by increasing the threshold. The dependency is almost linear, which means that also the height of the output pulse of the CSA has to be proportional to the height of the input signal¹. At low thresholds a slight non-linearity can be observed. The gain of the amplifier seems to be lower.

The width of the error function fit decreases at low thresholds and then stays almost constant. This is due to the slight non-linearity that can be seen in figure 6.2(a).

For the SNR, the value of the noise has to be compared to a real signal. For this, a radioactive source (⁵⁵Fe) can be used (for more details see chapter 8). The ⁵⁵Fe provides γ rays of about 5.9 keV that can get fully stopped in the sensor by the photoelectric effect. The electrons in the *Mu3e* experiment would deposited similar amounts of energy in the depletion layer. For each threshold, the injection pulse is determined which yields the same ToT as the photoelectric peak of the ⁵⁵Fe. This is used as signal for the SNR. For the noise, the width of the error function fit is chosen. The result is shown in figure 6.3. Good SNR values are achieved which range from 21.5 up to 35.7. The SNR rises slightly with the threshold. This is caused by the fact that the injection voltage, which refers to the ⁵⁵Fe γ -peak, is not constant but increases with the threshold. Moreover, the width of the error function fit shows a slight decrease at low thresholds.

For other tests, the threshold has to be chosen such that the minimal expected signal is sufficiently far above the mean value (9σ is a good value).

¹In fact, the CSA and its feedback circuit are designed such that the width of the output pulse is proportional to the input signal (see [Per12a]).

6 Measurements with Injection Pulses

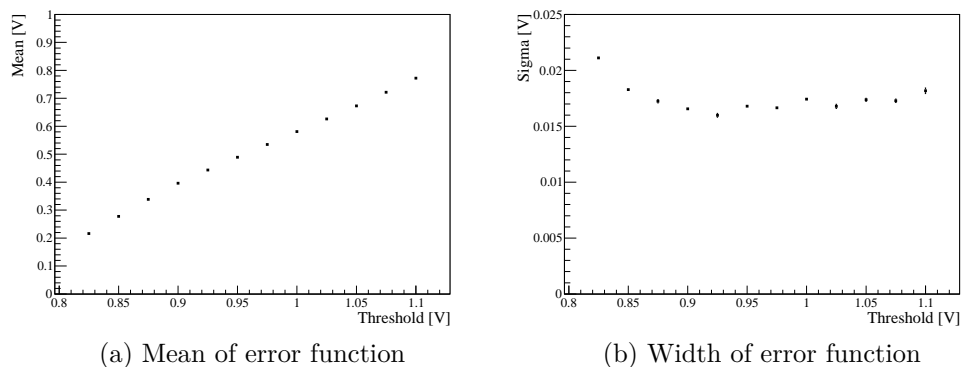


Figure 6.2: Fit results of injection-scans at various thresholds

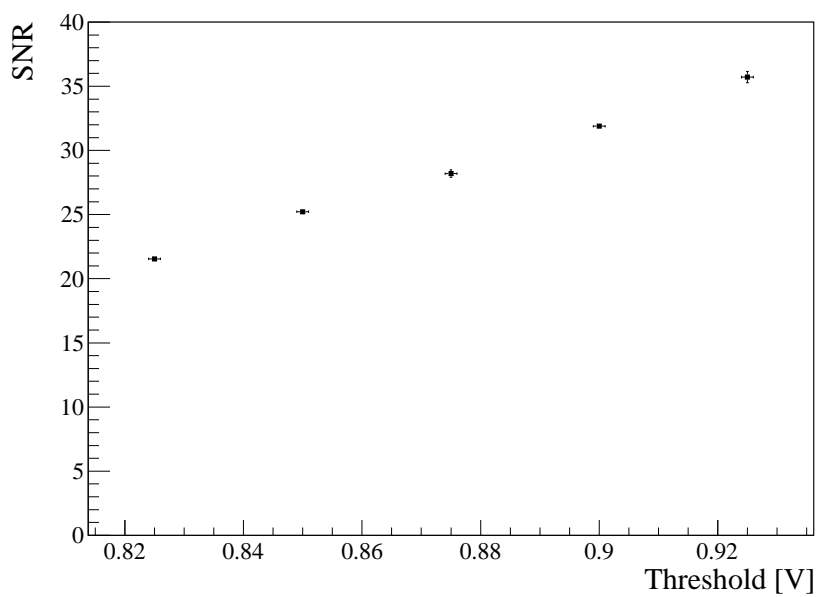


Figure 6.3: SNR obtained with the injection-scan and the ^{55}Fe source as signal reference

6.2 Injection-Scan and Threshold-Scan for the Entire Pixel Matrix

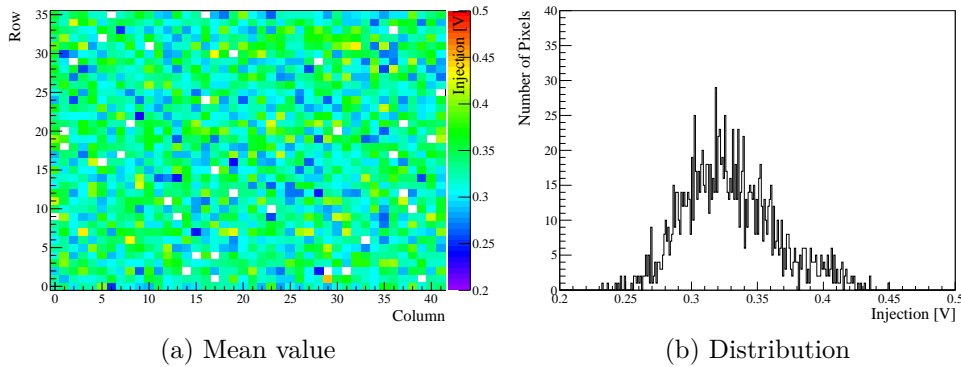


Figure 6.4: Fast injection-scan of all pixels in the pixel matrix.

(a) The mean value obtained by an error function fit is shown in colour for the individual pixels. A white pixel is drawn if the fit failed (usually when the ratio of detected signals does not go beyond 98 % or below 2 %).

(b) Histogram of the obtained mean values.

6.2 Injection-Scan and Threshold-Scan for the Entire Pixel Matrix

The injection-scan method presented in the previous section works satisfactorily only for a single pixel. To evaluate deviations between the pixels of the entire matrix it just takes too long to perform an injection-scan for each pixel individually. Such measurements are done with a ‘fast-scan’ method. The principle is similar to the single pixel injection-scan method, but it is performed for the whole pixel matrix at the same time. Therefore, in the fast scan procedure the hit-flags of all pixels are read out after each test pulse and stored in the FPGA. The fitting of the histograms is carried out subsequently. The fast injection-scan is shown in figure 6.4.

A similar fast scan can also be performed by varying the threshold voltage while the injection is kept constant. The injection represents a constant energy deposition. Figure 6.5 shows such a threshold-scan. The dispersion of thresholds is far too large for a good sensor performance. In the following section a method is presented that evens out this dispersion.

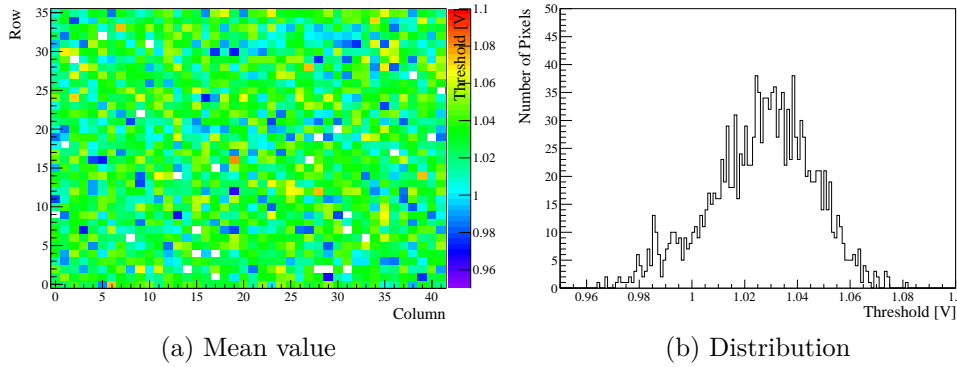


Figure 6.5: Fast threshold-scan of all pixels in the pixel matrix.

(a) The mean value obtained by an error function fit is shown in colour for the individual pixels. A white pixel is drawn if the fit failed (usually when the ratio of detected signals does not go beyond 98 % or below 2 %).

(b) Histogram of the obtained mean values.

6.3 TDAC-Tuning

As it became clear in the previous section the response of the individual pixels is not equal. Because the amplification and the offset of the comparator can differ slightly from pixel to pixel, a threshold dispersion is observed when a threshold scan is performed. Thus, every pixel needs an individual threshold. In the current prototype this is implemented as follows (see figure 5.1): In addition to the global threshold each pixels has a 4 bit DAC² that adds a certain voltage to the global threshold. The ‘strength’ of these TDAC values can be chosen via the bias voltage VPDAC.

The influence of the TDAC value on the threshold is shown in figure 6.6. Here, for all possible TDAC values a threshold-scan is performed for a single pixel (just as the injection-scan for a single pixel but with a constant injection and a variable threshold). The resulting mean value is plotted against the TDAC value. It can be seen that higher TDAC values have a

²The values of this ‘tune’ DAC will be called ‘TDAC’ in the following. Herein, the ‘T’ stands for tuning.

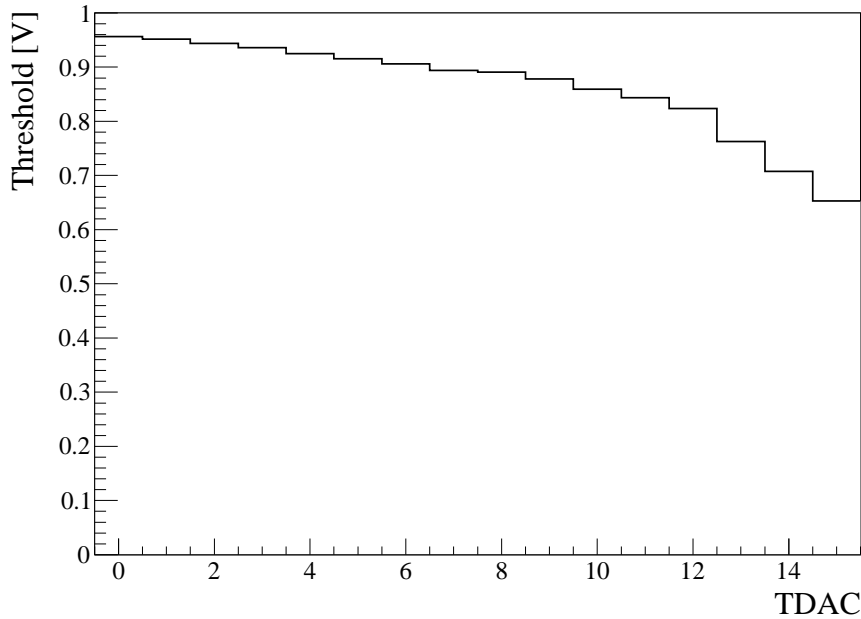


Figure 6.6: Mean value obtained by a threshold-scan for a central pixel as function of the TDAC value

greater impact on the threshold.

The best TDAC value is determined via the ‘fast-tune’³ procedure. As there is no linear dependency between threshold and TDAC and every pixel behaves slightly differently, the easiest way to find the correct TDACs is by just trying the different values. Firstly, all TDACs are set to 7. A series of test pulses is generated. The actual TDAC value is assigned to all pixels that detect $\sim 50\%$ ⁴ of the test pulses. For the remaining pixels the procedure is repeated with a higher or lower TDAC value corresponding to the ratio of detected pulses and so on. Pixels which would need an even lower or higher TDAC value are assigned 0 or 15 respectively. Figure 6.7 shows the distribution of the TDAC values. Higher TDAC values are

³There was a previous tuning procedure that was much slower (and less accurate).

This is why the current procedure is called ‘fast’.

⁴The applied condition is that the ratio lies within a window of 40% to 60%. If this window is too narrow, the procedure is not able to find the correct TDAC value.

6 Measurements with Injection Pulses

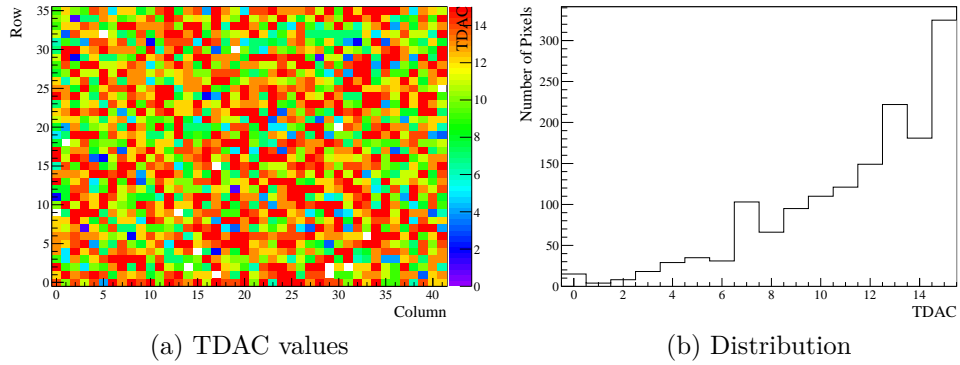


Figure 6.7: TDAC values obtained with the fast-tune procedure
(a) The TDAC values assigned to the individual pixels are shown in colour.
(b) Histogram of the number of pixels which yield a certain TDAC value.

assigned to more pixels than lower ones. As can be seen in figure 6.6 high TDAC values span a wider range in threshold than lower ones and have consequently a higher probability.

In order to evaluate the quality of the tuning, another kind of injection-scan can be applied. For a certain injection-pulse, the number of activated pixels is counted. The voltage of the injection-pulse is swept. Figure 6.8 shows the results without (all TDAC = 0) and with tuning. As after tuning most of the pixels get activated by the same injection voltage the distribution rises more steeply as before tuning. The width of the applied error function fit decreases from (31.5 ± 1.0) mV to (12.5 ± 0.3) mV.

A threshold-scan that is performed before and after tuning reveals the strength of the tool (see figure 6.9). The threshold dispersion is drastically reduced. Without tuning the mean of the thresholds is 1.026 V with an RMS of 0.0196 V, after tuning it is 0.990 V and has a RMS of 0.0023 V which is nearly one order of magnitude smaller. The mean decreases slightly because the local threshold can only be increased by the TDAC values. Thus on average a smaller threshold is determined by the threshold scan method as it varies the global threshold voltage.

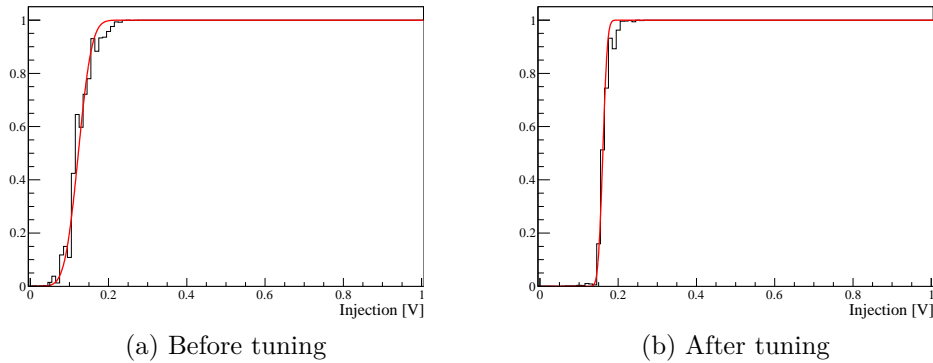


Figure 6.8: Fraction of activated pixels in the matrix as function of the injection pulse

6.4 Pixel Response Time

Latency denotes the time difference between a particle hit or a test pulse and the occurrence of the sensor signal. Fluctuations of the latency are called jitter. In the following discussion, fluctuations of the signal of a single pixel are called single-pixel-jitter and the differences across the pixel matrix matrix-jitter. Especially the matrix-jitter is an important quantity for a good sensor performance. In the later experiment time frames of 50 ns will be used and therefore the matrix-jitter should lie significantly below this value.

For this purpose, 25 pixels are randomly chosen and the ToT signals observed on the oscilloscope. The test pulses as well are tapped on the second adaptor at the Uxibo and observed on the oscilloscope, thus allowing for latency measurements.

Figure 6.10 shows the measured latency. The values have a mean of (59.37 ± 1.63) ns and lie all within a range of 6 ns.

In figure 6.11 the single-pixel jitter is plotted. The mean is (0.74 ± 0.18) ns and so about two orders of magnitude smaller than the latency. All measured values lie within a range of about 0.8 ns.

The matrix-jitter obtained with this procedure is already acceptable but

6 Measurements with Injection Pulses

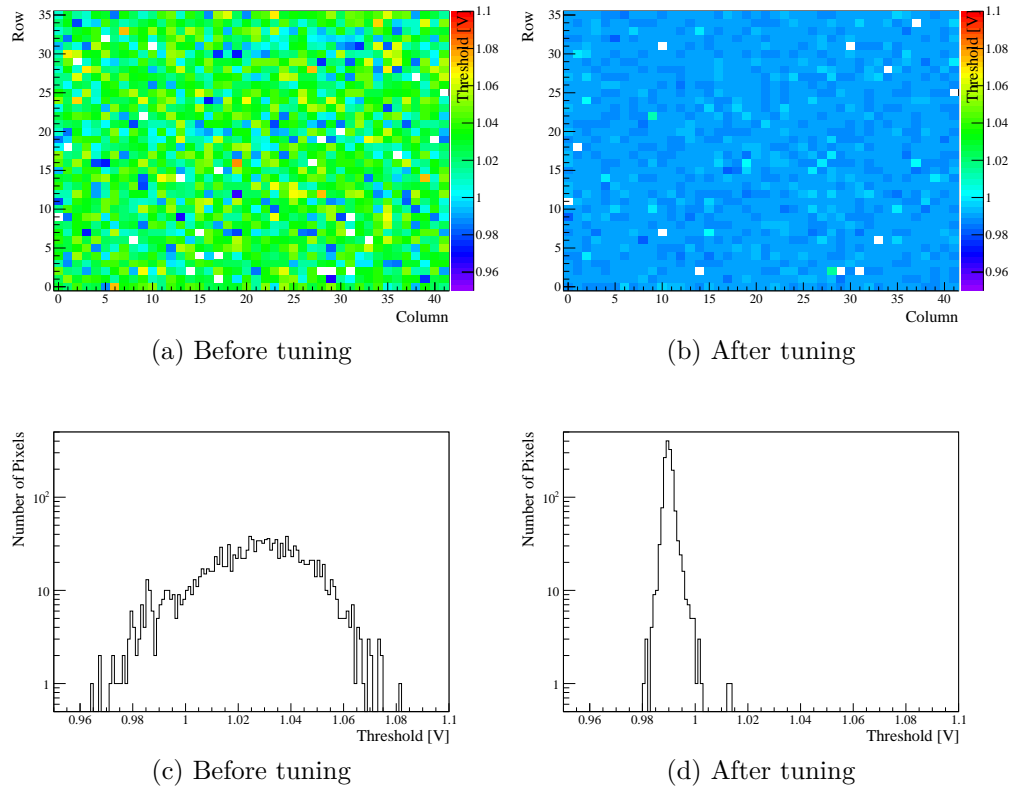


Figure 6.9: Threshold-scan for the entire pixel matrix performed before and after tuning

(a) & (b) The mean value obtained by an error function fit is shown in colour for the individual pixels. A white pixel is drawn if the fit failed (usually when the ratio of detected signals does not go beyond 98% or below 2%).

(c) & (d) Histogram of the obtained mean values.

6.4 Pixel Response Time

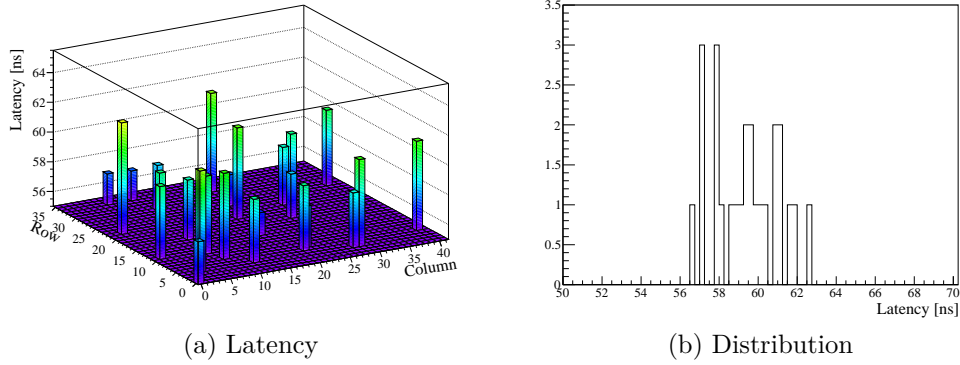


Figure 6.10: Latency of randomly chosen pixels obtained with test pulses (average over 1000 pulses).

- (a) Latency of the individual pixels
- (b) Histogram of the measured latencies

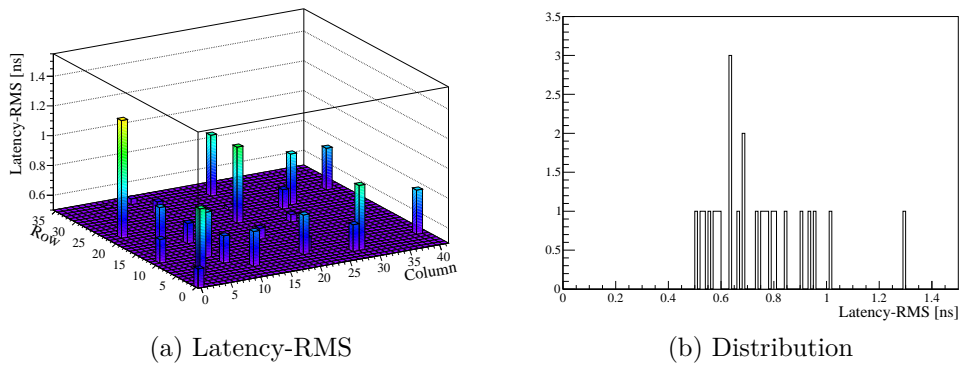


Figure 6.11: Latency-RMS or single-pixel jitter of randomly chosen pixels obtained with test pulses (average over 1000 pulses).

- (a) Single-pixel jitter of the individual pixels
- (b) Histogram of the measured single-pixel jitter

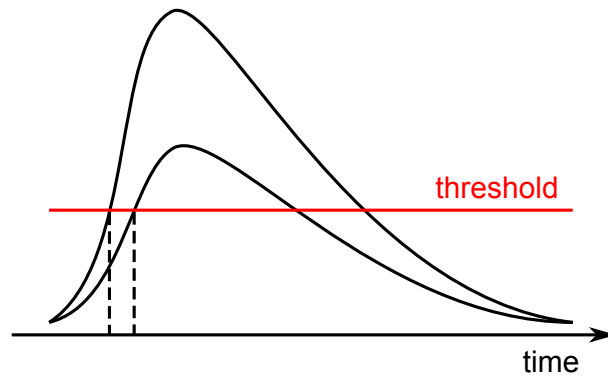


Figure 6.12: Influence of the pulse height on the latency

the latency itself is relatively long. So far, it seems that the timing cannot benefit from the fast charge collection with the current electronics, especially as this test was performed with very high test pulses. For such pulses the output pulse of the CSA has a steeply rising edge and is consequently earlier above threshold (as illustrated in figure 6.12). In the case of real particles, also much smaller pulses can occur. Hence, the latency and the matrix-jitter are larger. Additional delays from the charge collection inside the depletion layer play only a minor role.

The pixel-wise observation on the oscilloscope is no suitable procedure for measuring a large number of pixels. For this purpose, the trigger window can be used, whose starting time and width can be controlled by the software. In the matrix-readout mode, only hits are registered that occur within the trigger window. By scanning of the starting time of the trigger window, the latencies for all pixels can be determined. However, currently the increment is limited by the Uxibo to 20 ns. It is thus rather coarse and does not allow a measurement.

7 Measurements with LEDs and Laser Diodes

LEDs and laser diodes pulsed with a function generator can be used for timing measurements. The output of the function generator can be observed on the oscilloscope and thus compared to the sensor output. For the characterisation of the *MuPix* sensor white and blue LEDs and laser diodes with a wavelength of 850 nm are used.

Photons of a few eV get mainly absorbed by the photoelectric effect. The intensity I decreases exponentially with the penetration depth x as described by the Beer-Lambert law

$$I = I_0 e^{-\mu x}. \quad (7.1)$$

Herein, I_0 denotes the initial intensity at $x = 0$ and μ the absorption coefficient. The absorption coefficient depends on the involved absorption processes, the absorbing material and the energy of the incident photons. In this chapter measurements of the latency and double pulse resolution with LEDs and laser diodes are presented.

7.1 Latency and Time-over-Threshold

Latency is the delay between a particle hit and the appearance of the detector signal and should thus be small. A long ToT leads to a long dead time and increases the probability to miss subsequent particle hits. Both quantities are studied with LEDs.

The setup for measurements of latency and ToT with LEDs or laser diodes

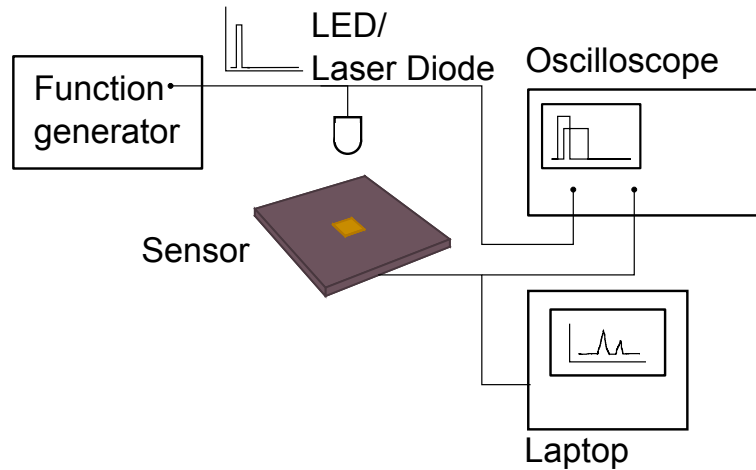


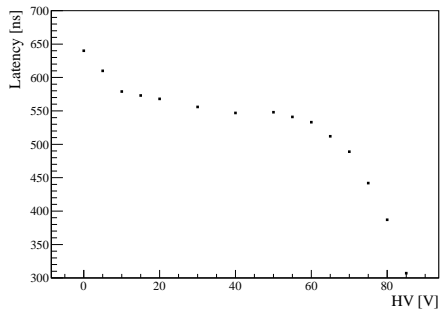
Figure 7.1: Schematic of the LED or laser diode setup

is shown in figure 7.1. A function generator is used to pulse the LED which illuminates the sensor. The sensor is operated in the ToT mode and the comparator output is directly tapped by a probe and observed on an oscilloscope. Thus, the ToT can be easily measured. In order to determine the latency, both the output of the function generator and the comparator output are observed at the oscilloscope and the delay between both signals is measured. Of course, additional delays resulting from different cable lengths are considered.

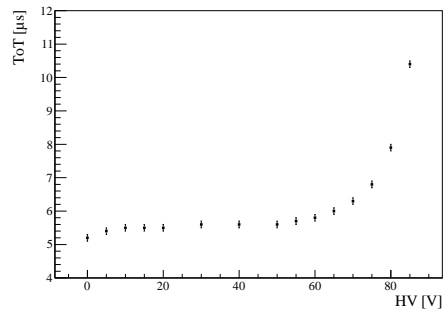
Figure 7.2 shows how the latency and ToT of a central and a corner pixel changes with the applied high voltage.

The ToT of the central pixel first rises slightly with the high voltage and then stays constant at about $5.5 \mu\text{s}$ up to 50 V. For higher bias voltages the ToT rises steeply. In this regime the electric field inside the depletion layer is so strong, that the electrons gain enough energy to generate secondary electron-hole pairs and thus amplification occurs. Additionally, the width of the depletion zone increases with the high voltage, as described in appendix 1, and thus the number of absorbed photons in the active volume. However, the depletion zone extends mostly into the bulk and thus to decreasing photon intensity because the n-well is more heavily doped than the substrate. Consequently, the amount of additional photons per increase

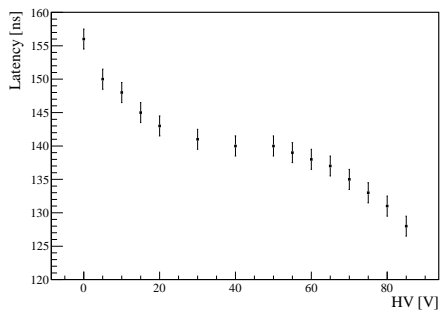
7.1 Latency and Time-over-Threshold



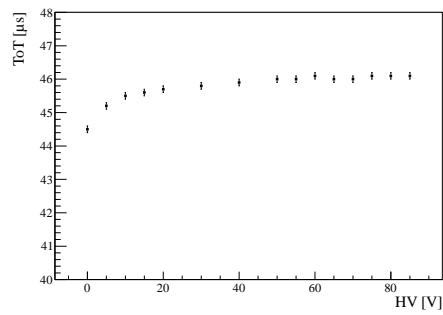
(a) Central pixel: Latency



(b) Central pixel: Time-over-threshold



(c) Corner pixel: Latency



(d) Corner pixel: Time-over-threshold

Figure 7.2: Influence of the applied high-voltage on the latency and time-over-threshold of a central and a corner pixel (Please note the different y-axes for central and corner pixel)

of the high voltage decreases. The effect should be more pronounced at smaller high voltage and cannot alone explain the steep rise at higher bias voltages.

A similar behaviour can be observed for ToT spectra of a ^{55}Fe source (see section 8.2).

The latency instead decreases with the high voltage. The larger the amount of collected charges, the steeper the signal rises and thus the earlier it is above threshold. Additionally, the charge collection time as well decreases with the bias voltage. However, this seems to be a minor effect. The latencies measured are far above the calculated charge collection time and are therefore dominated by the electronics.

The ToT of the corner pixel shows at low bias voltages a similar behaviour as the central pixel but does not rise at higher voltages. Moreover, the corner pixel has a much higher ToT than the central one. The corner pixels are surrounded by bulk material. The depletion layer extends into that material. Thus, the pixel at the edges and corners of the sensor cover effectively a larger area and consequently detect more photons than an inner pixel. This leads to longer ToT and even shorter latencies. The fact that the ToT does not increase further with the high voltage is most probably due to saturation effects.

The behaviour of the corner pixels is studied further in the following section.

7.2 Pulse Shape

The *MuPix* sensor has digital output only. There is no possibility to tap the analogue signal before the comparator. However, with the measurement of latency and ToT it becomes possible to reconstruct the pulse shape.

The measurement of the pulse shape is performed with the same setup as for latency and ToT measurements. Figure 7.3 shows the principle. For a constant threshold the point on the rising edge is given by the latency and the point on the falling edge by the sum of latency and ToT. The pulse is

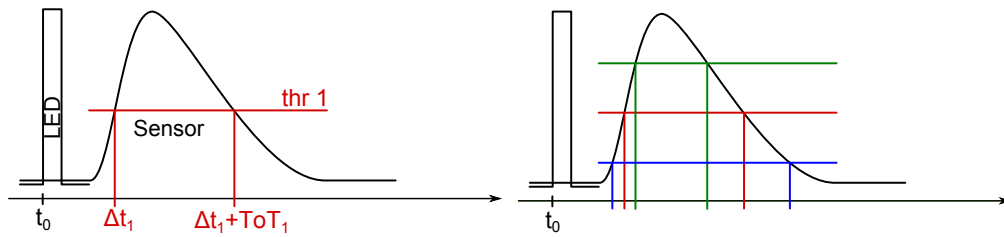


Figure 7.3: Principle of the pulse shape measurement as explained in the text

	Time constant [μs]
High pass τ_1	4.14 ± 0.31
Low pass τ_2	0.955 ± 0.063

Table 7.1: Time constants of the CR-RC filter derived by fit

then scanned by varying the threshold.

Figure 7.4 shows an exemplary pulse shape. The response function of a CR-RC filter as derived in appendix 2 is fitted to the data and describes it very well. The derived time constants are given in table 7.1

Measuring the pulse shape allows comparison between corner and central pixels (see figure 7.5(a)). The pulse shape of the corner pixel is much larger and longer than for a central pixel. It already shows saturation effects at low thresholds. A corner pixel collects charges from a far larger volume than a central pixel.

Comparing the pulse shapes at different high voltages (see figure 7.5(b)) supports the theory of amplification discussed in the previous section. The amplitude above baseline increases by about 80% by changing the high voltage from 60 V to 80 V. Consequently, the ToT becomes more than 40% larger (at a threshold of 0.9 V) and the latency is shorter.

Moreover, the influence of the various global bias voltages (see figure 5.1) can be studied. These voltages determine the timing and shape of the pulse. A compromise between fast latency and reasonable ToT on one hand and a good pulse amplitude and thus SNR on the other hand has to be found. Figure 7.5(c) shows the pulse shapes for the default configuration

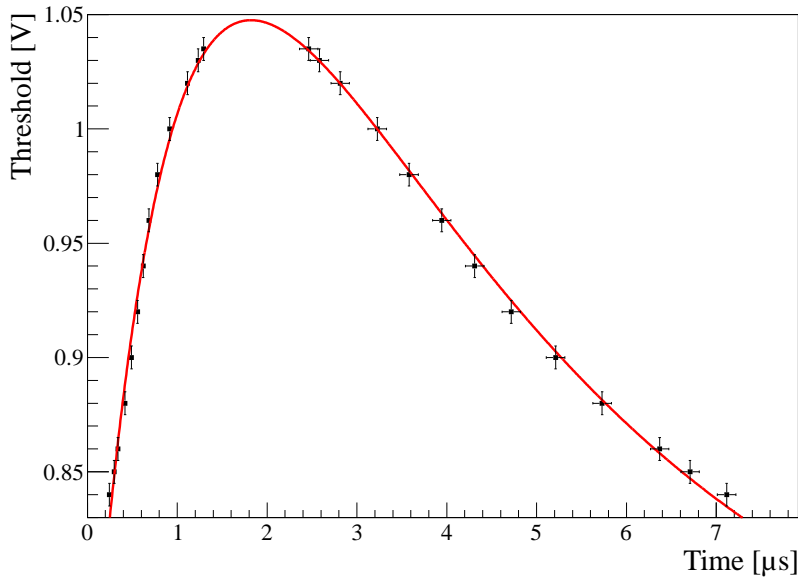


Figure 7.4: Pulse shape with fitted CR-RC filter response

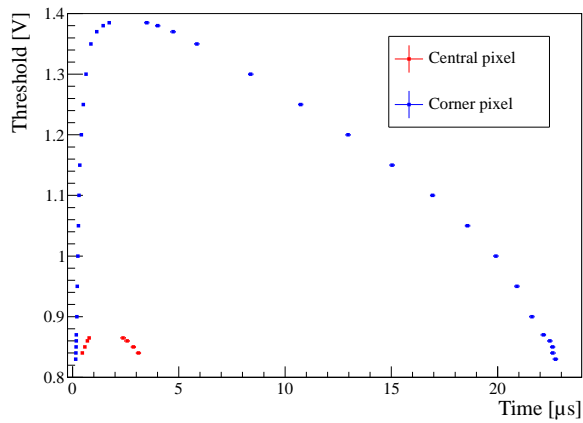
and for a new configuration which is improved for timing (the values can be found in table 1 in the appendix). The pulse is significantly shortened (by about 45% at a threshold of 0.86 V) and rises earlier but has also a lower amplitude leading to worse SNR.

7.3 Double Pulse Resolution

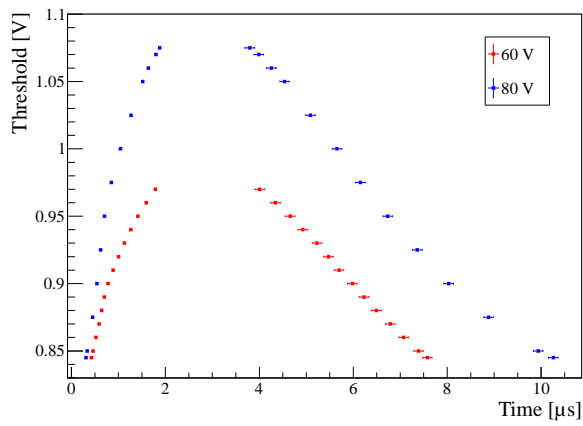
If a detector is exposed to high particle rates, pile-up can occur. If the time difference between two particle hits is too short, the detector cannot resolve the second hit. The actual double pulse resolution is an important quantity which has to be measured.

Therefore, double pulses are applied to the LED. If there is a long delay between the single pulses the sensor is able to distinguish between them and two pulses are visible in the ToT mode. But if the delay is much shorter these two pulses merge into a single output pulse with a much longer ToT (see figure 7.6).

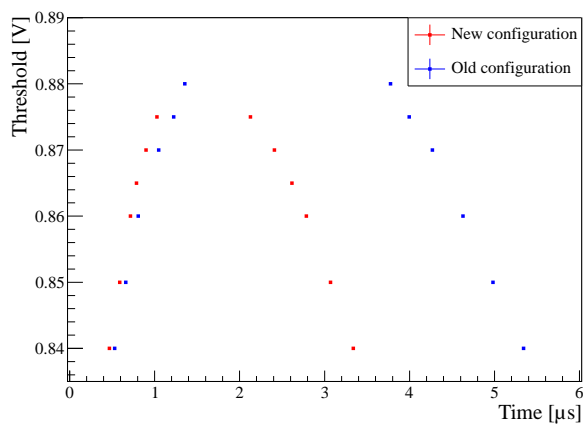
7.3 Double Pulse Resolution



(a) Pulse shape of a central and a corner pixel

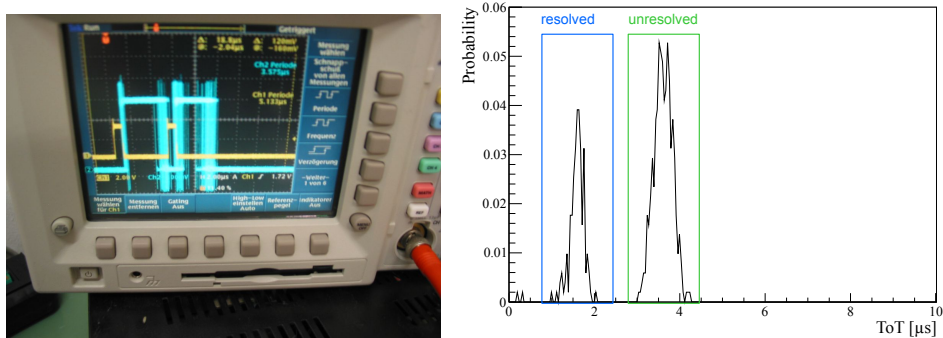


(b) Pulse shape for a high voltage of 60 V and 80 V



(c) Pulse shape obtained with an old and a new set of global bias voltages

Figure 7.5: Comparison of pulse shapes



(a) Double pulse on the oscilloscope. The double pulse from the function generator (yellow) and the signal from the sensor (blue) can be seen. (b) ToT spectrum of double pulses. Double pulses that could not be resolved show up in a peak at higher ToT (highlighted in green)

Figure 7.6: Double pulse measurement

For the analysis of the double pulse resolution, ToT spectra are recorded for different delays. Resolved double pulses show up in a peak at smaller ToT and unresolved in a peak at higher ToT (see figure 7.6). The number of events in each peak is counted and the ratio of unresolved double pulses is plotted against the delay (see figure 7.7). An error function is used to describe the data. The blue line indicates the point where only 1% of the double pulses cannot be resolved. In this measurement this point is reached at an delay of about $(2.678 \pm 0.002) \mu\text{s}$. However, this value is strongly dependent on the chosen threshold and the energy deposited. Figure 7.8 exemplarily shows the influence of the threshold and the voltage powering the LED on the double pulse resolution. Moreover, the double pulse resolution differs from pixel to pixel, as for example the pixels at the fringe have a significantly different pulse shape.

For the later experiment the double pulse resolution has to be determined with radiation that matches the maximum energy deposited by the electrons in the pixel sensor in *Mu3e*.

7.3 Double Pulse Resolution

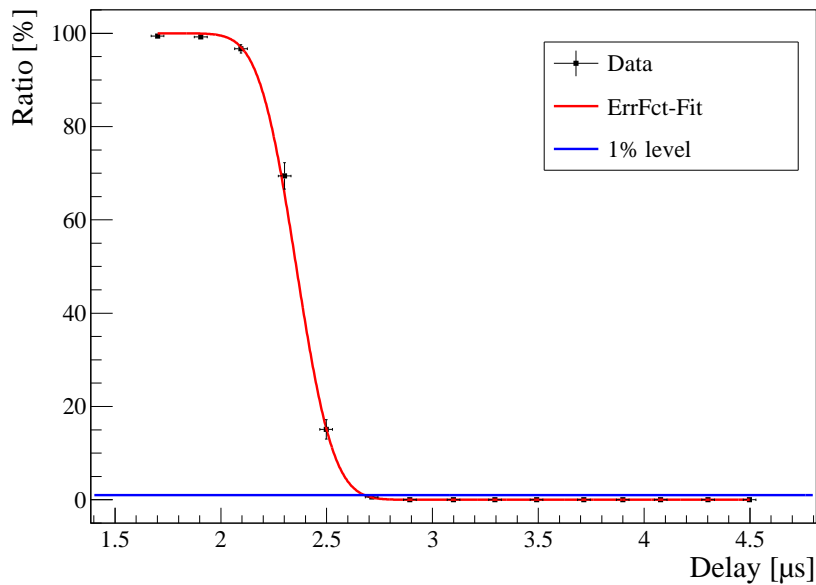
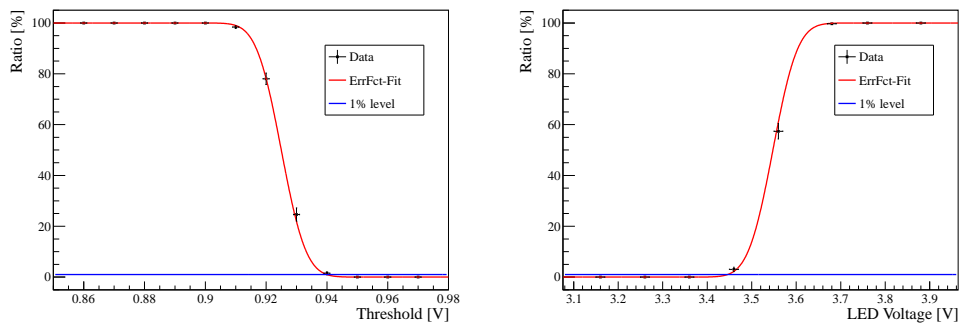


Figure 7.7: Double pulse resolution. The ratio of unresolved double pulses is plotted against the delay between the two pulses



(a) Double pulse resolution as function of the threshold for a constant delay (b) Double pulse resolution as function of the voltage at the LED

Figure 7.8: Influence of threshold and deposited energy on the double pulse resolution. The ratio of unresolved double pulses is plotted against the delay between the two pulses

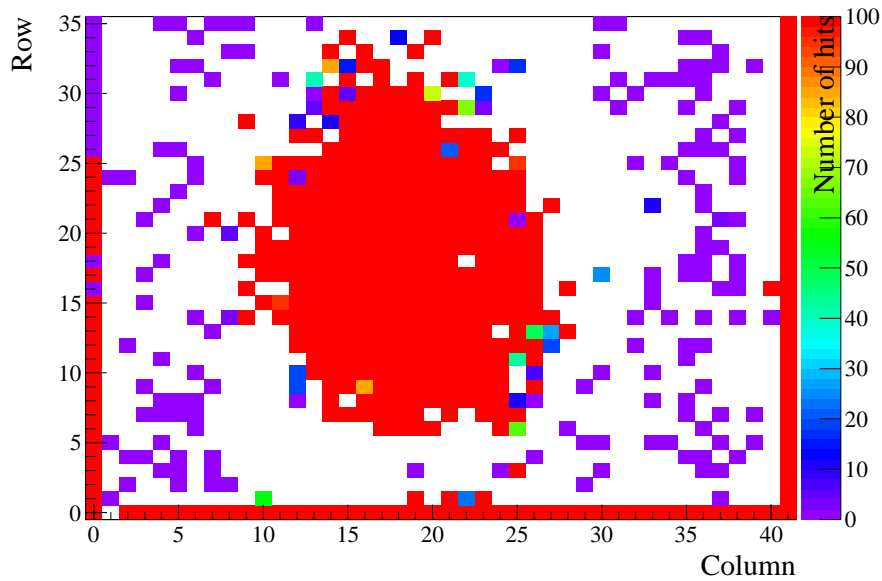


Figure 7.9: Overlay of 100 pictures of a pinhole illuminated with a LED taken with the *MuPix* sensor. The colour indicates how often the individual pixel has detected the LED light

7.4 Readout of the Total Pixel Matrix

While operated in hit-flag mode, the sensor can be used to take ‘pictures’. Figure 7.9 shows 100 accumulated pictures of a pinhole which is illuminated with the LED. The shape of the pinhole is clearly visible. In the illuminated area most of the pixels detect photons in every exposure while the other pixels are mostly inactive. The fringe again has a special role. At three edges the pixels are very active. This is due to scattered light. As these pixels cover effectively a much larger area a lower light intensity is still sufficient to generate enough charges to activate the pixel. At the fourth edge the pixels are not surrounded by bulk material but border on a different kind of test pixels, which are not studied in this thesis. Consequently, these pixels behave like other central pixels.

More detailed studies performed with the pixel matrix readout can be found in [Aug12].

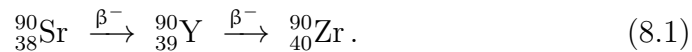
8 Measurements with Radioactive Sources

Radioactive sources offer the possibility to test the sensor with real particles. The sources used provide either electrons with a few 100 keV or γ 's in the range of a few keV up to MeV.

8.1 Radioactive Sources

Four different radioactive sources are used for the *MuPix* tests: ^{55}Fe , ^{60}Co , ^{90}Sr and ^{137}Cs . The results of measurements with the ^{90}Sr - and ^{55}Fe -source are representatively presented here.

^{90}Sr decays via β^- -emission. A proton of the nucleus converts to a neutron under the emission of an electron and a neutrino. The electron has a continuous energy spectrum with the decay energy as upper edge. The daughter nucleus of ^{90}Sr is a β^- -emitter as well. Therefore, the ^{90}Sr -decay is a two-staged decay with decay energies of 546 keV and 2.28 MeV



^{55}Fe however decays via electron capture



The missing electron in the inner shells of the daughter isotope ^{55}Mn will be filled by an outer electron leading to the emission of an Auger electron

or γ 's. The K_α -line¹ is of particular interest for the *MuPix* test. The monochromatic γ 's of 5.90 keV can be absorbed via the photoelectric effect in the depletion zone, resulting in a peak in the ToT spectrum.

8.2 Time over Threshold Spectra

For a single pixel the output of the comparator can be multiplexed to a testpad which allows to do spectral measurements of the ToT (time-over-threshold).

Figure 8.1 shows a ToT spectrum of the ^{90}Sr source². ^{90}Sr has been exemplarily chosen as β^- emitter. The shape of the spectrum is due to three effects. At first, there is the continuous spectrum of the two β^- -decays. Energies below the threshold cannot be measured, therefore the spectrum is cut at the left. Secondly, the height of the signal depends on the amount of generated charges. The electrons are not totally stopped in the sensor but only lose part of their energy depending on the length of the path and the energy. And finally, the whole amount of charges is not always collected by a single pixel (see discussion on ^{55}Fe spectra).

The ToT spectra of the ^{55}Fe source³ have a different slope (see figure 8.2). A clear peak is visible due to the photoelectric effect. The energy of the γ quantum is transferred in a single interaction. If this happens inside the depletion layer, all generated charge carriers can be collected. If the charges are mainly collected by a single n-well, this results in the γ -peak whereas charge collection by two or more pixels results in shorter ToT. Of course, coincidences of two or more γ 's are possible and thus ToT larger than the ToT of the γ -peak occur. Moreover, charges generated outside the depletion layer – for example in the bulk – can be partially collected and thus contribute to the spectrum.

The ^{55}Fe spectrum is fitted with a Gaussian function that describes the γ -

¹Probability for K_α is 24.4%. For K_β (6.49 keV) it is 2.86%.

²The ^{90}Sr -source used has an activity of 3.7 MBq.

³The ^{55}Fe -source used has an activity of 332 MBq.

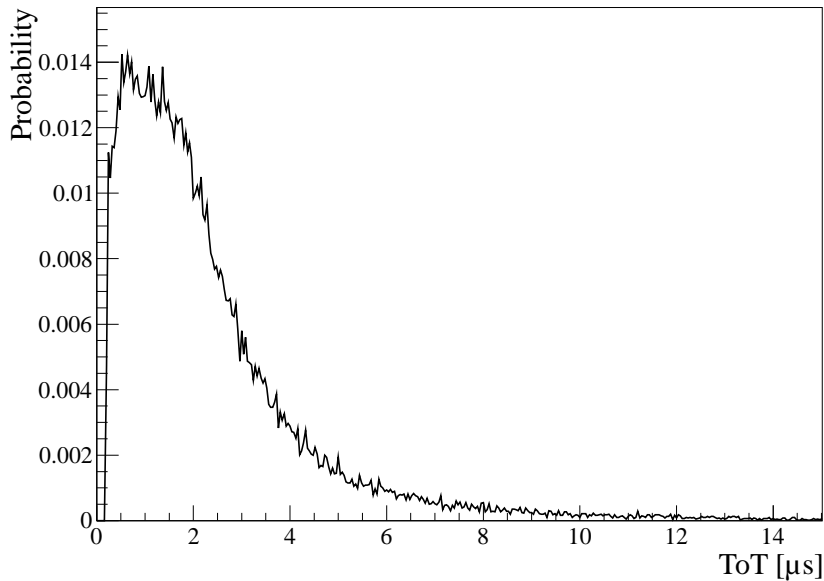


Figure 8.1: ToT spectrum of the ^{90}Sr source

peak and an underlying exponentially decaying function representing the events in which the charges have been shared between pixels or got partially lost in the bulk.

Figure 8.3 shows the shift of the ^{55}Fe γ -peak as a function of the threshold. With increasing threshold the peak moves almost linearly to smaller ToT. Consequently, there is a linear relationship between the signal height and the ToT.

In figure 8.4 the influence of the applied reverse bias voltage on the ToT of the ^{55}Fe γ -peak is shown. At low bias voltages, the ToT rises steeply. The electric field in the depletion zone grows and thus also the collection efficiency. Larger amounts of collected charges lead to higher signals and longer ToT. In the range of about 20 V to 60 V, the ToT remains basically constant. The diode collects the total charge. Further increase of the high voltage finally leads to rising ToT. The electric field inside the depletion layer is now so strong that the electrons generated by the incident radiation gain enough energy to create additional electron-hole pairs. Amplification

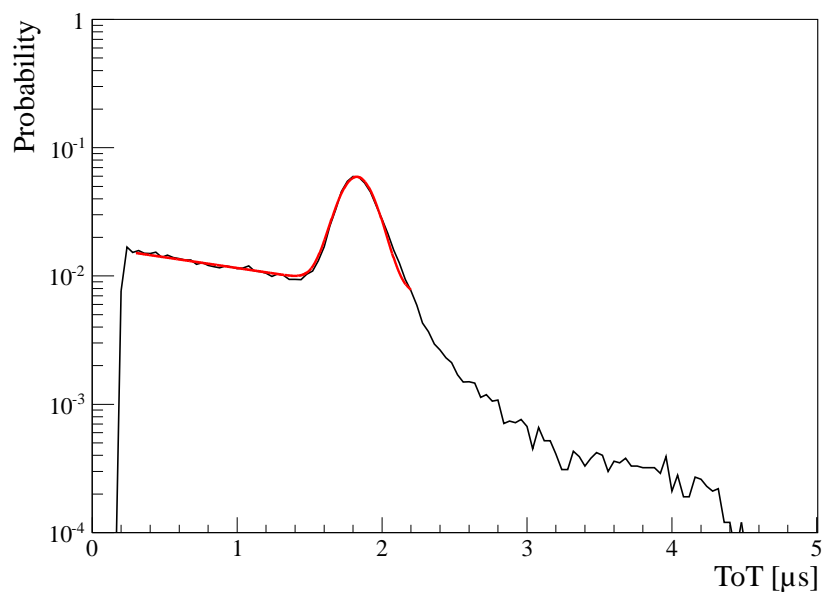


Figure 8.2: ToT spectrum of the ^{55}Fe source. A fit is applied which describes the γ -peak

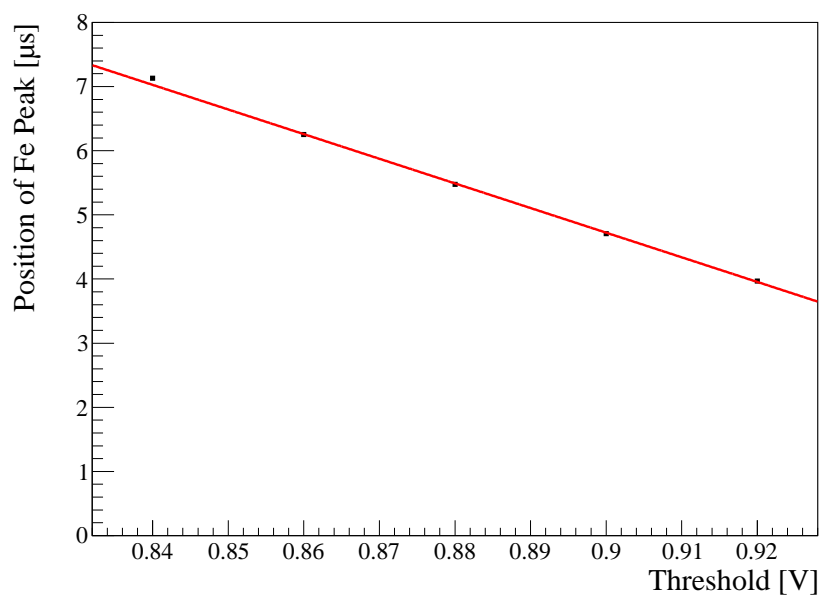


Figure 8.3: Shift of the ^{55}Fe γ -peak as a function of the applied threshold

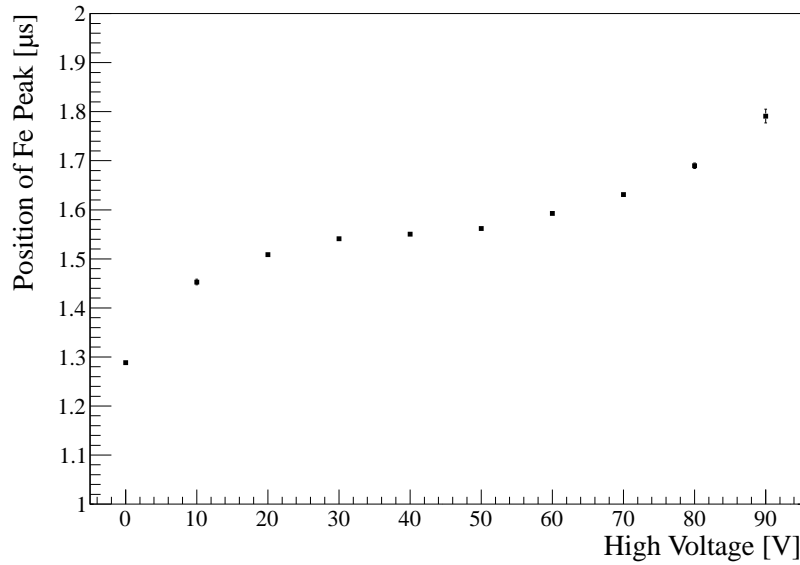


Figure 8.4: Shift of the ^{55}Fe γ -peak as a function of the applied high voltage

effects occur. The amount of collected charges rises and longer ToT are observed. The sensor shows a similar behaviour as a gaseous ionisation detector.

This measurement is performed at 30 °C and 80 °C (see figure 8.5). Both measurements show the same high voltage dependency of the ToT but the amplification effect seems to be much more pronounced at 30 °C. At lower temperatures, the mean free path of the electrons is longer. So they can become faster and thus more easily generate secondary electron-hole pairs.

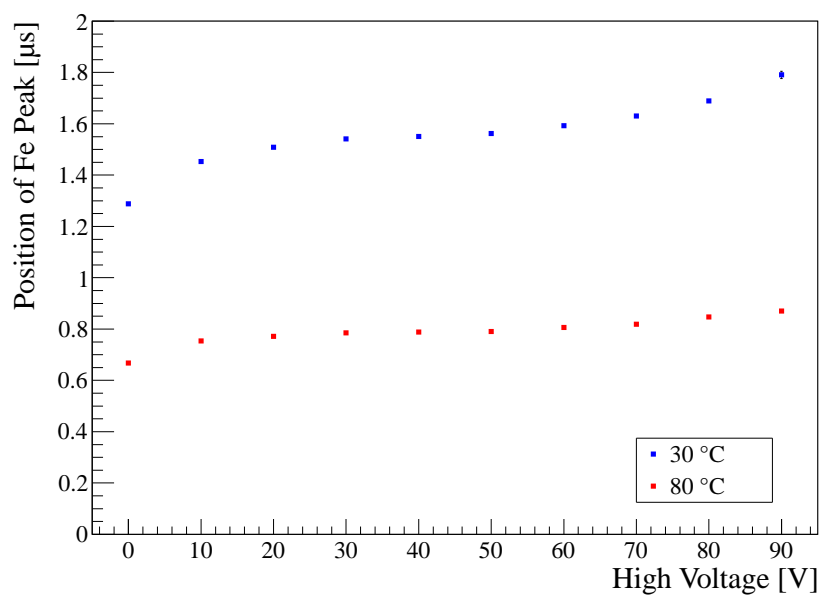


Figure 8.5: Shift of the ^{55}Fe γ -peak as a function of the applied high voltage at 30 °C and 80 °C

9 Measurements with X-ray Fluorescence

By exposing a material to X-radiation, e. g. from a X-ray tube, electrons from the target material can get excited to higher energy levels. The following de-excitation leads to the emission of characteristic X-rays. These X-rays have typical energies of a few ten's of keV depending on the target material and thus lie in a similar energy range as the γ -rays from the ^{55}Fe source. By determining the position of the photoelectric peak in the ToT spectra, the influence of the deposited energy on the ToT can be evaluated.

ToT spectra of various sources are recorded with the setup shown in figure 9.1 and 9.2. The sensor is shielded from the initial X-rays by an aperture. The target itself emits the characteristic radiation isotropically. The targets used and the corresponding X-ray energies are summarised in table 9.1.

In figure 9.3 the ToT spectra of a single (central) pixel for a constant threshold are plotted. A similar fit as in section 8.2 is performed to de-

Target	Z	E_{K_α} [keV]	E_{K_β} [keV]
Ti	22	4.47	4.89
Fe	26	6.40	7.05
Ni	28	7.48	8.28
Cu	29	8.06	8.92
Zn	30	8.66	9.60
Zr	40	15.80	17.70
Mo	42	17.48	19.61

Table 9.1: Energies of the K-lines of the various target materials

9 Measurements with X-ray Fluorescence

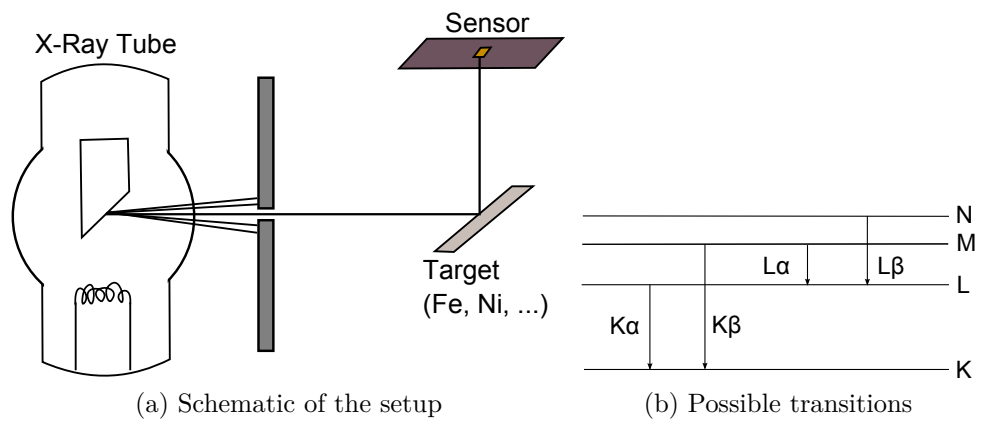


Figure 9.1: X-ray fluorescence

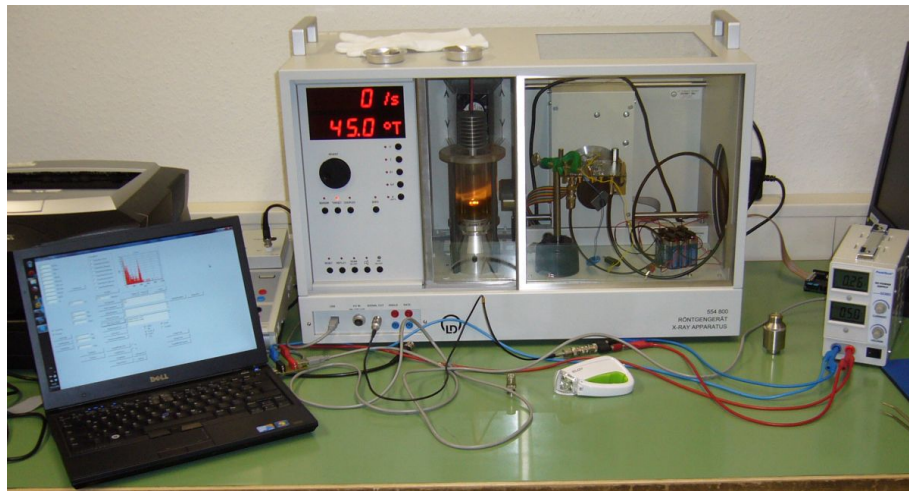


Figure 9.2: Photograph of the X-ray fluorescence setup. The X-ray tube is located in the left part of the device whereas the target and the sensor are placed in the right part

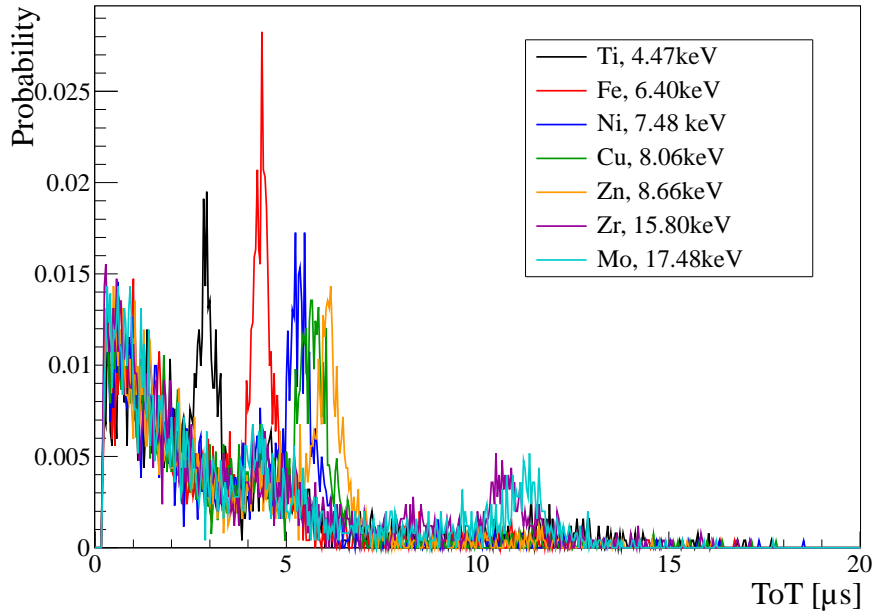


Figure 9.3: ToT spectra of the different X-ray fluorescence targets of a central pixel

termine the ToT of the peak. This ToT is then plotted as a function of the energy of the corresponding K_{α} line (see figure 9.4). An exponential function is fitted to the data. As the pulses have a relatively steeply rising edge, the ToT is basically determined by the falling edge. A rough calculation yields the expected exponential energy dependency of the ToT.

The pulse can be approximated by (see appendix 2)

$$U(t) \approx U_0 \exp\left(-\frac{t}{\tau}\right). \quad (9.1)$$

In this case, the amplitude U_0 is proportional to the deposited energy E . The pulse decreases with time and falls below the threshold voltage U_{thr} after the time interval t_{ToT}

$$U_{\text{thr}} \approx U_0 \exp\left(-\frac{t_{\text{ToT}}}{\tau}\right) \quad (9.2)$$

$$\Rightarrow E \propto U_0 \propto \exp(t_{\text{ToT}}). \quad (9.3)$$

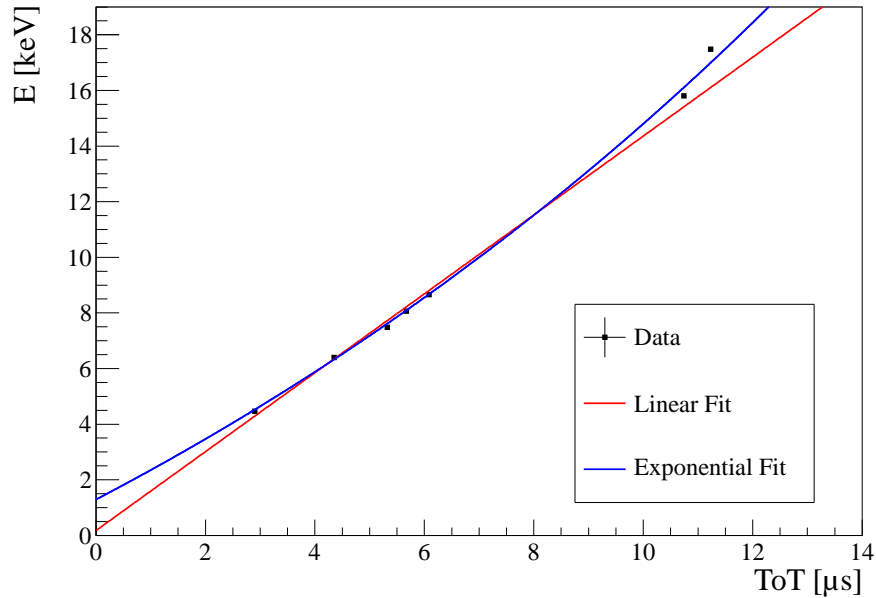
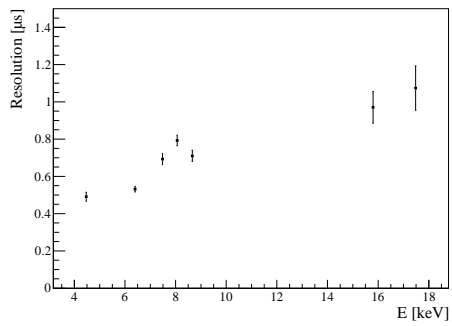


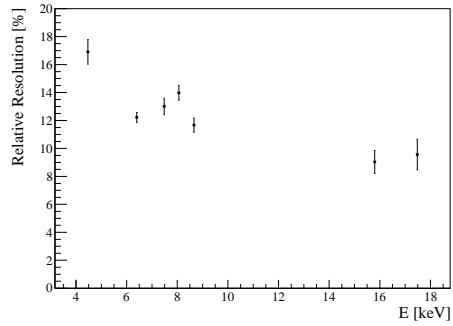
Figure 9.4: Plot of the ToT of the photoelectric peak of the various K_{α} lines and applied linear and exponential fit

A linear fit, which is also applied, does only approximately describe the data.

The width of the fluorescence peak is an estimator for the energy resolution. As conventionally used, the full width at half maximum ($\text{FWHM} = 2.35\sigma$) is chosen for the energy resolutions shown in figure 9.5. The energy resolutions are given in terms of ToT and the relative energy resolution (ToT of the width divided by the ToT of the peak) is plotted. A relative energy resolution of about (10 – 20) % can be achieved. This is due to charge sharing between neighbouring pixels. A larger pixel size – as planned for *Mu3e* – would improve the energy resolution. However, for the *Mu3e* experiment the information about the energy deposition in the single pixels is irrelevant and thus no good energy resolution is needed.



(a) Absolute energy resolution



(b) Relative energy resolution

Figure 9.5: Energy resolution determined in the X-ray fluorescence spectra. The FWHM of the photoelectric peaks is plotted against the corresponding energy. The errors result from fit.

10 Temperature Dependence

In the later experiment temperatures of up to about 60 °C and temperature differences in the range of 40 °C are expected (see [Zim12]). Therefore, the performance of the pixel sensors at temperatures above room temperature has to be studied.

For this purpose, the PCB with the sensor is placed inside a temperature chamber and heated up to (30–80) °C. Tests with internal injection pulses and the ^{55}Fe source are performed. With the ^{55}Fe source the total sensor is tested at a constant energy deposition. The injection pulses allow to test the electronics separately from the sensor diode. Thus, comparison between physical and electronic-related effects become possible.

10.1 ^{55}Fe Source

At the different temperatures a ToT spectrum with the ^{55}Fe source is taken (see figure 10.1). By a fit like in section 8.2 the ToT of the photoelectric peak can be determined. Figure 10.2 shows the temperature dependence of that peak. The error in ToT results from the fit whereas the error on the temperature is estimated to be 1 °C. The ToT of the peak decreases with increasing temperature almost linearly. A linear fit is applied. The absolute value of the slope is given in table 10.1.

10.2 Test Pulses

10.2.1 ToT Spectra

In order to distinguish between physical and electronic-related effects, similar measurements are done with the internally generated test pulses. The injection pulse is chosen such that it has almost the same ToT as the

10 Temperature Dependence

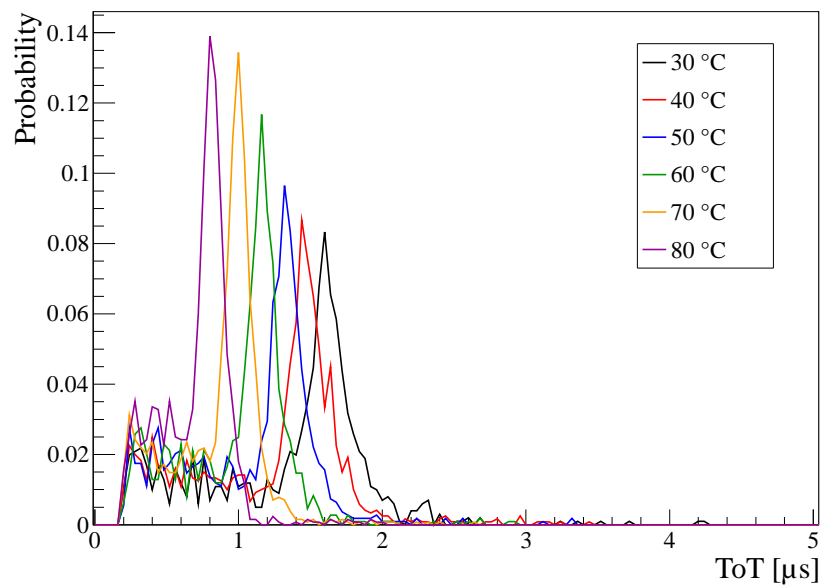


Figure 10.1: ToT spectra of ^{55}Fe γ -rays at different temperatures
(Note: The spectra are normalised. As a consequence, the height of the peak appears to be smaller for spectra which span a wider range in ToT.)

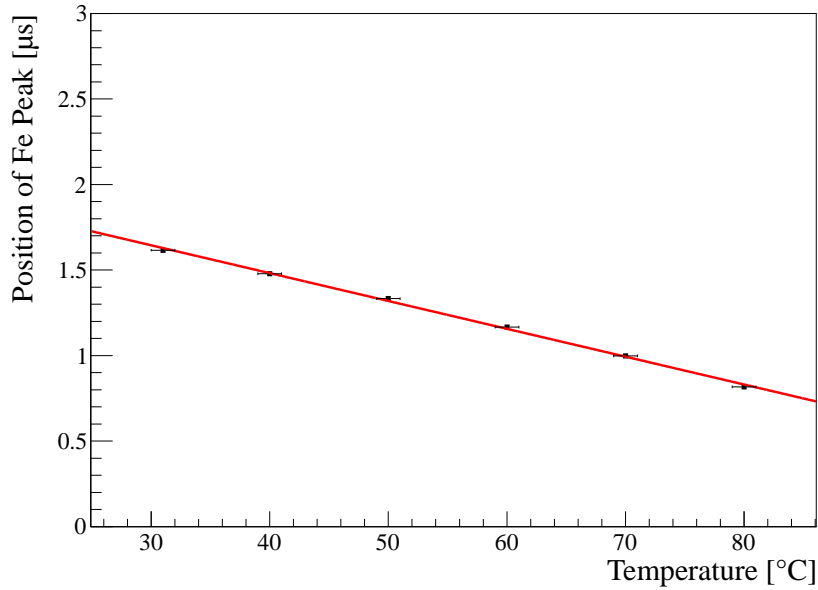


Figure 10.2: Influence of the temperature on the ToT of the photoelectric peak of the ^{55}Fe γ -rays

^{55}Fe peak at 30 °C. The position of the peaks is determined by fitting a Gaussian distribution and is plotted against the temperature. The results can be seen in figures 10.3 and 10.4. Here again the ToT decreases linearly with the temperature. The fit results for the slope are given in table 10.1. The measurements with ^{55}Fe and test pulses show almost the same slope. The temperature dependency seems to originate mainly from the electronics. A possible source is the CSA (see figure 10.5). The feedback capacitance C_f that detects the signal charge is discharged via a feedback circuit. The current of that feedback circuit rises with increasing temperature and thus C_f is faster discharged. The output pulse of the CSA decreases faster and its amplitude becomes smaller. A simulation of the output pulse confirms the observed behaviour (see figure 10.6).

10 Temperature Dependence

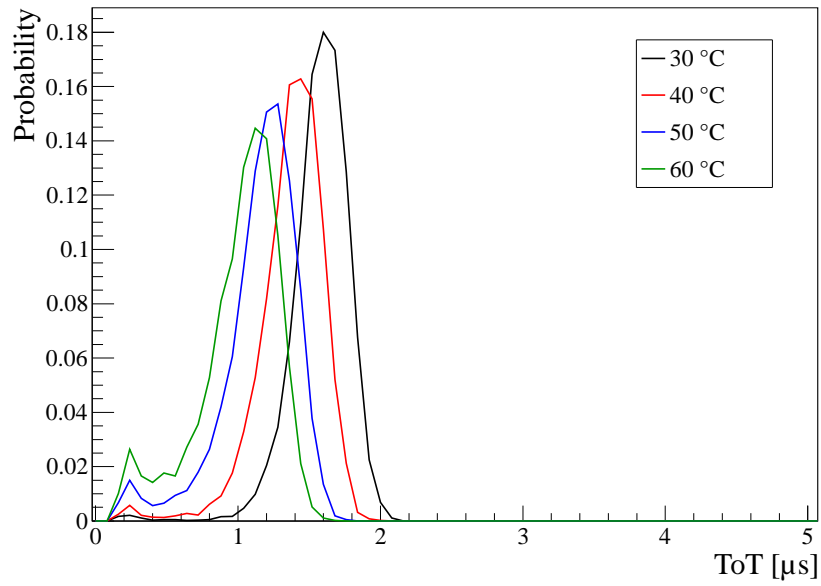


Figure 10.3: ToT spectra of injection pulses at different temperatures. The injections are chosen such that they fit the ^{55}Fe peak at 30 °C (Note: Again, the spectra are normalised.)

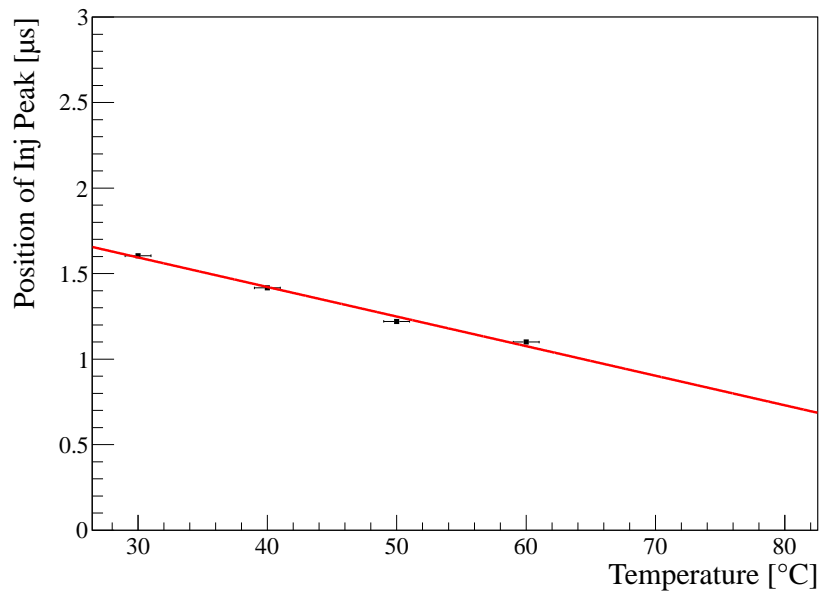


Figure 10.4: Influence of the temperature on the ToT of injection pulses

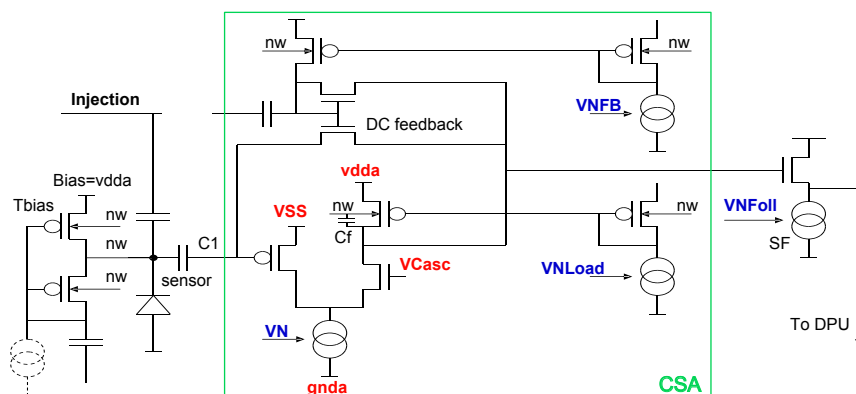


Figure 10.5: Electronics inside the pixel. The CSA is highlighted in green (graphic taken from [Per12a])

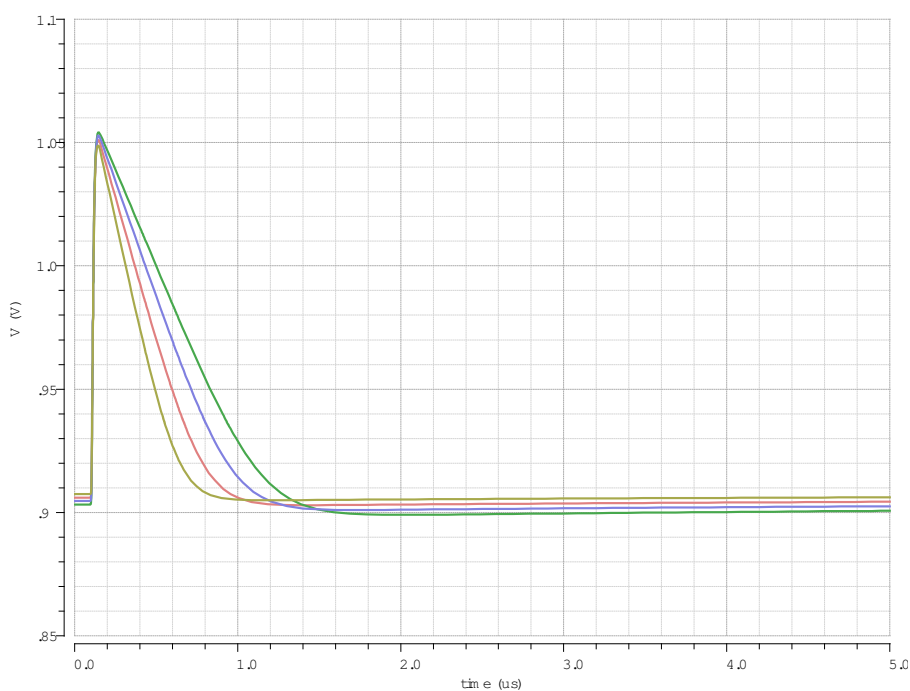


Figure 10.6: Simulation of the output pulse at 30°C (green), 40°C (blue), 50°C (red) and 60°C (yellow) (simulation by courtesy of Ivan Perić)

10 Temperature Dependence

Measured with	Absolute value of slope [ns/°C]
⁵⁵ Fe	16.3 ± 0.4
Test pulses	17.3 ± 0.8

Table 10.1: Absolute values of the slope obtained by a linear fit

10.2.2 Injection Scan

Another quantity that is expected to change with temperature is the noise. The thermal noise is due to velocity fluctuations of the electrons and scales with the square root of the temperature (see [Spi08]).

To study this behaviour injection-scans as in section 6.1 are performed. The width of the error function fit is a measure of the noise. Figure 10.7 shows the mean value and the width obtained by an error function fit at the different temperatures.

The mean value increases with temperature. This supports the theory of increasing feedback current. The feedback capacitor is discharged faster at higher temperatures and therefore the output pulse at the CSA cannot reach the same amplitude as at lower temperatures. A higher injection is necessary to pass the threshold.

The width and thus the noise increases slightly with the temperature. In combination with the decreasing pulse height the SNR gets worse with increasing temperature. A linear fit is applied to be able to estimate the increase of the noise. The slope is (0.293 ± 0.010) mV/°C.

10.3 Temperature Sensor

The *MuPix2* sensor features an additional diode that can be used for temperature measurements. The resistance of the diode is expected to change with temperature. A first test in the temperature chamber is performed. For different temperatures the resistance of the diode is measured with a multimeter¹. The results are plotted in fig 10.8. The resistance decreases

¹KEITHLEY, Model 2000 Multimeter

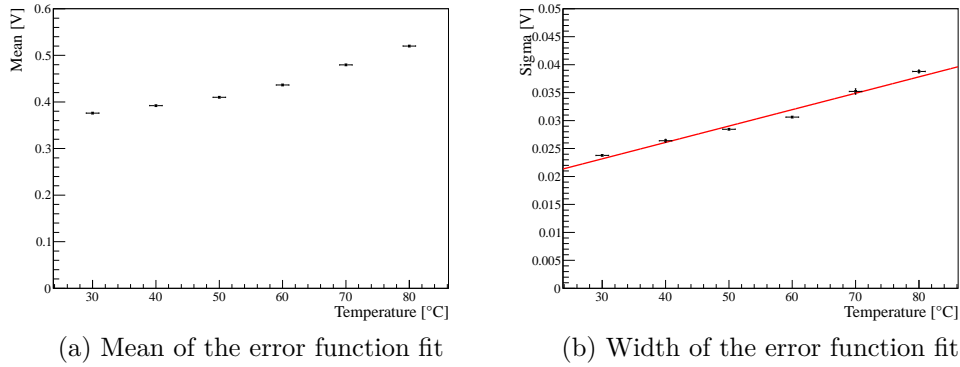


Figure 10.7: Injection-scan at various temperatures for a central pixel

with temperature.

The current-voltage characteristic of a diode is given by the Shockley diode equation. Reduced to the temperature dependent terms the current I becomes (see [SN07])

$$I \propto \sqrt{\frac{D}{\tau}} n_i^2 \exp\left(\frac{eU}{k_B T}\right), \quad (10.1)$$

wherein D denotes the diffusion constant, τ the charge carrier lifetime and n_i the intrinsic charge carrier concentration. e is the elementary charge, k_B the Boltzmann constant, U the forward bias voltage and T the temperature.

The intrinsic charge carrier concentration is strongly temperature dependent

$$n_i^2 \propto T^3 \exp\left(-\frac{E_g}{k_B T}\right), \quad (10.2)$$

with the band gap energy E_g .

For the diffusion constant term the following temperature dependence is assumed

$$\sqrt{\frac{D}{\tau}} \propto T^{C_1}, \quad (10.3)$$

10 Temperature Dependence

with the constant C_1 .

Thus, the current yields

$$I = C_2 T^{3+C_1} \exp\left(\frac{eU - E_g}{k_B T}\right), \quad (10.4)$$

with the proportionality constant C_2 .

Usually, the voltage is measured at a small constant current

$$U = \frac{E_g}{e} + \frac{k_B T}{e} \ln\left(\frac{I}{C_2 T^{3+C_1}}\right) \propto -T, \quad (10.5)$$

at sufficiently small currents. Consequently, the resistance as well decreases with temperature.

A linear fit is applied to the data. The resistance decreases with a slope of $(-217 \pm 6) \Omega/^\circ\text{C}$ and an ordinate intercept of $(67.7 \pm 0.3) \text{ k}\Omega$.

For the *Mu3e* experiment, having temperature sensors distributed over the whole tracking detector is of large interest as it provides information about how well the cooling works and allows for compensation of temperature effects in the performance of the pixel sensors. However, in order to use the diode as temperature sensor further tests and more exact calibration has to be done, e. g. the current-voltage characteristic should be measured.

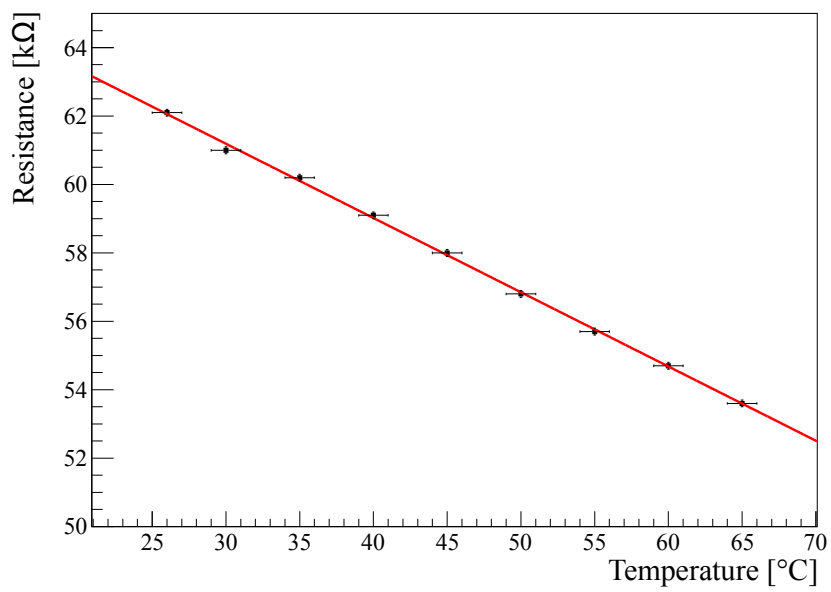


Figure 10.8: Resistance of the temperature diode for different temperatures

11 Testbeam Measurements at the SPS

Two testbeam measurements have been performed in August 2012 at the T4-H8 beamline at the *CERN* north area. The total run time was in the range of hours.

T4-H8 is a secondary beamline of the *Super Proton Synchrotron (SPS)*, the final injector of the *LHC* (see figure 11.1). The primary beam is a (400 – 450) GeV/ c proton beam. By a conversion target different kinds of particle beams can be produced for the secondary beamline. In this measurement, 180 GeV/ c pions were selected which have a comparable energy loss to the electrons in the *Mu3e* experiment of about 0.5 keV/ μm .

The pion rate is in the range of MHz. There is a spill approximately every 45 s which lasts about 10 s.

The testbeam measurements were performed together with the *Timepix* telescope (see [tim, Pla10]). The *MuPix* sensor was operated such, that it was only active while the *Timepix* took data too. The telescope takes data for up to ~ 1 ms and reads out afterwards, which takes approximately 20 ms. Thus, the actual data taking time was further reduced.

Firstly, the *MuPix* was operated parasitically in front of the telescope. The distribution of hits over the pixel matrix can be seen in figure 11.4(a). As the active area of the sensor is very small, it is rather difficult to place the sensor directly in the beam. A tendency of more hits on the left side is visible. However, the run time was quite short and so each pixel has only a small number of hits (9.4 ± 4.3 on average, see figure 11.5).

After this first test in front of the *Timepix* telescope the sensor was placed at the device under test (DUT) position between the two telescope submo-

11 Testbeam Measurements at the SPS

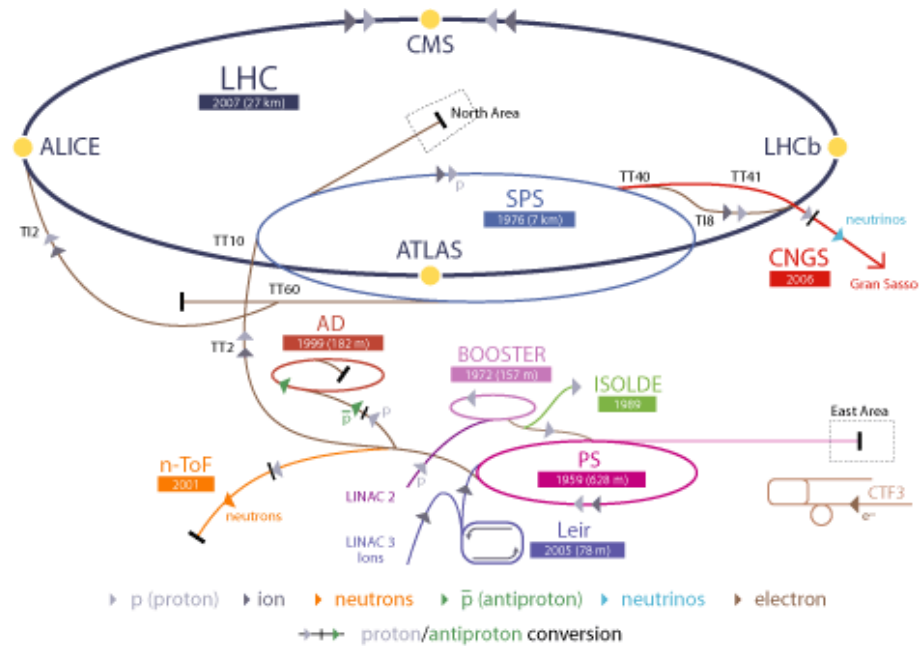


Figure 11.1: Accelerators at *CERN* (graphic taken from [CER12])

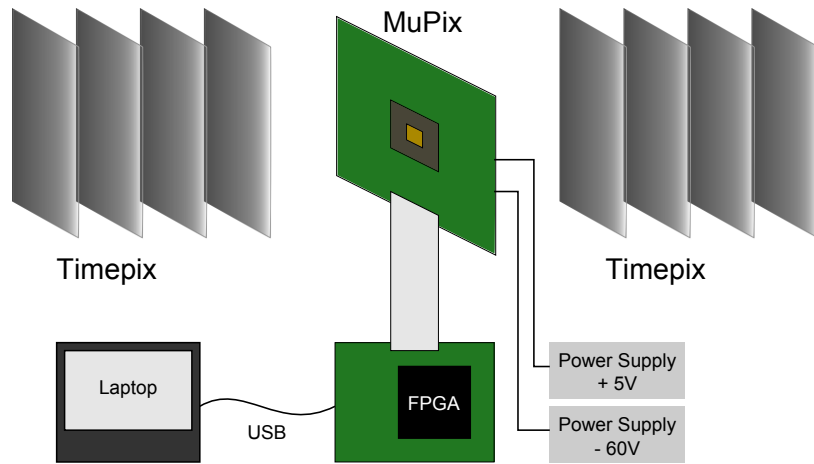
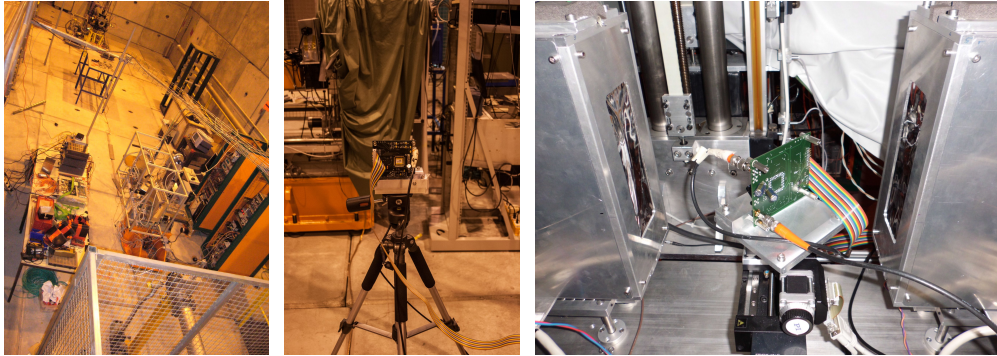


Figure 11.2: Setup with the *MuPix* sensor at the DUT position of the *Timepix* telescope



(a) Overview over the T4-H8 beamline (b) The *MuPix* sensor in front of the *Timepix* telescope (c) The *MuPix* sensor at the DUT position of the *Timepix* telescope

Figure 11.3: At the testbeam area T4-H8

dules (see figures 11.2 and 11.3). The sensor is consequently at a different position with respect to the beam line and so the hit distribution over the pixel matrix looks different (see figure 11.4(b)). Again, the number of hits per pixel is small due to the run time, 11.0 ± 4.0 on average (see figure 11.5(b)).

An important quantity to know is the cluster size, i.e. the number of activated pixels per particle hit. By charge sharing, more than one pixel can be activated by a single particle. The cluster size has effects on the spatial resolution and the data rate in the later experiment.

Figure 11.6(a) shows a typical event. Only a single pixel has detected a particle hit. In figure 11.6(b) a large cluster is shown. Such a pattern is most probably due to particles that showered in the surrounding material. Figure 11.7 shows histograms of the cluster size. Single pixel clusters are most probable. Clusters of two pixels occur with a probability that is already more than one order of magnitude smaller. The probability for clusters with more than four pixels is less than 4% and clusters of ten or more pixels occur with a probability of less than 1%. The analysis of cluster sizes is not corrected for pile-up. This would need the additional information of the *Timepix* telescope.

11 Testbeam Measurements at the SPS

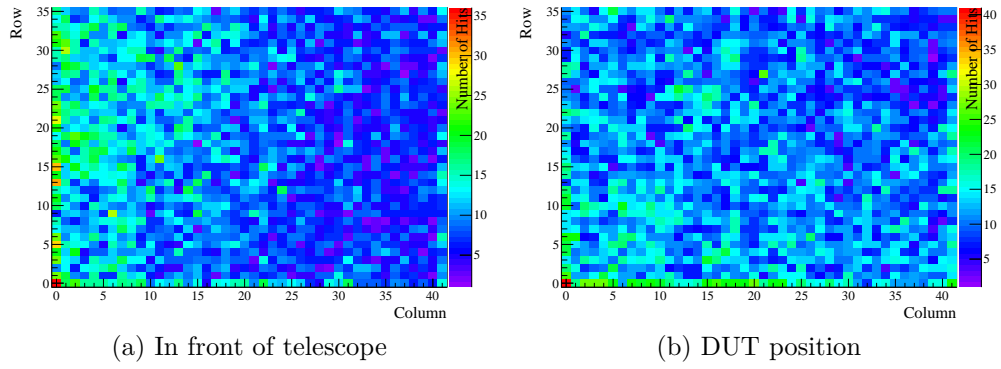


Figure 11.4: Distribution of hits over the pixel matrix. The colour indicates how often the individual pixel was hit while running in front of the telescope or at the DUT position

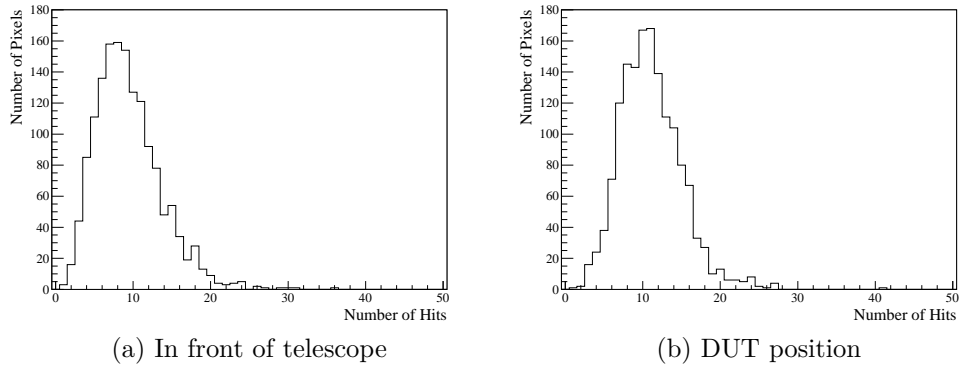
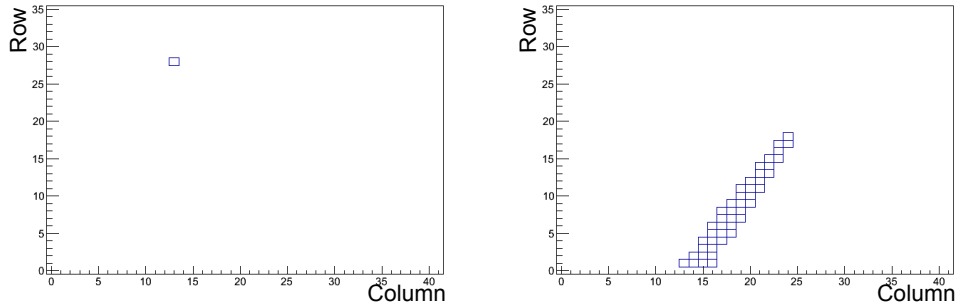
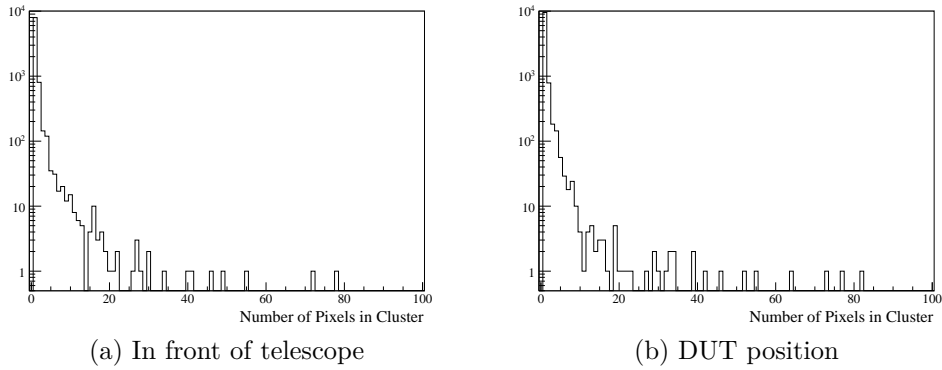


Figure 11.5: Histogram of the number of hits in a single pixel



(a) Typical event: only a single pixel is hit (b) Particle showered in the surrounding material

Figure 11.6: Plots of the hit pixels during gate of the *Timepix* telescope



(a) In front of telescope

(b) DUT position

Figure 11.7: Histogram of the size of clusters during one gate of the *Timepix*

11 Testbeam Measurements at the SPS

The combined analysis of the *Timepix* and *MuPix* data offers more possibilities. With the *Timepix* data the individual particle tracks can be reconstructed. This can be used to study the efficiency of the individual pixels and cross talk. But again this analysis might suffer as well from the short run time. At the moment, the combined analysis is still pending.

Part III

Discussion

12 Discussion and Outlook

The novel *Mu3e* experiment aims to search for the charged lepton flavour violating decay $\mu^+ \rightarrow e^+e^-e^+$ with a sensitivity of one in 10^{16} muon decays, four orders of magnitude better than previous experiments (see [B⁺12]). The Standard Model of particle physics implies the conservation of the lepton flavour and the extended Standard Model including lepton mixing yields suppressions far beyond experimental reach. As a consequence, the observation of the decay $\mu^+ \rightarrow e^+e^-e^+$ would be a clear sign for new physics.

The projected sensitivity can only be reached by exploiting novel detector technologies. The *Mu3e* detector will be based on a tracking detector consisting of *High Voltage Monolithic Active Pixel Sensors* which provide an excellent SNR and fast charge collection combined with the possibility of thinning of the sensor down to $50\mu\text{m}$ or less improving the multiple scattering dominated momentum resolution.

The characterisation of the first two *HV-MAPS* prototypes for the *Mu3e* experiment is the subject of this thesis. The sensors *MuPix1* and *MuPix2* are therefore tested in different setups. The results are summarised and discussed in this chapter.

12.1 Discussion

Test pulses can simulate signals caused by particle hits. The test pulses are injected in a capacitor that substitutes the sensor capacitance. Thus, the electronics can be tested.

12 Discussion and Outlook

The injection-scan method determines the noise level of single pixels. Compared to signals induced by a ^{55}Fe source, excellent signal-to-noise (SNR) values in excess of 20 can be achieved.

As the amplification and the threshold offset is slightly different for the individual pixels, non-uniformities in the pixel response occur. The TDAC tuning method allows an individual fine-adjustment of the local threshold and yields a reduction of the threshold dispersion by nearly one order of magnitude.

The mean latency of 25 randomly chosen pixels determined with test pulses yields (59.37 ± 1.63) ns and is so nearly three orders of magnitude higher than the expected charge collection time. Benefits from the fast charge collection would be hardly visible. Moreover, these latencies have been measured with high injection voltages so the output signal of the CSA has a steeply rising edge and goes rapidly above threshold. Particle hits can produce smaller signals and have thus even longer latencies.

The matrix-jitter however is measured to be acceptable but will be larger for particles, as the amount of generated charge carriers fluctuates.

Additional delays from the sensor diode are not considered in the test pulse measurements. However, as the charge collection time is very small, this is only a minor effect.

Tests with LEDs are performed to determine the timing behaviour of the prototypes, in particular the latency and ToT.

The long shaping times seem to be the major drawback of the current prototypes. The measured latencies are of the order of a few 100 ns and the ToT of μs .

The pulse shape of the signal before the comparator is measured and shows the expected shape of a CR-RC filter, but yields time constants of μs .

Consequently, double pulse resolutions in the range of μs are determined as they strongly depend on the pulse shape.

The timing can be influenced by varying a set of global bias voltages. This leads to an improvement but does not achieve the desired fast timing

behaviour with time constants in the range of 10 ns to 100 ns.

Consequently, for the following submissions of prototypes the CSA and shaper have to be modified. However, this might result in worse SNR.

In comparison to pixels in the central area of the sensor, the pixels at the edges and corners are much more sensitive. Illuminated with the LED they yield pulse shapes with much higher amplitudes and ToTs in the range of a few 10 μ s.

This is due to the fact that the depletion layer also extends into the surrounding bulk material. Thus, the edge pixels have a larger detection volume.

In the later experiment, the pixel size is larger than in the tested prototypes and so this effect will be less pronounced. Furthermore, the overall percentage of edge pixels will be smaller, as the sensors are larger. Nevertheless, compensation methods might be of interest, e.g. by adjusting the local threshold as in the TDAC tuning procedure.

Spectral measurements of the ToT are performed for single pixels irradiated with radioactive sources. The ^{55}Fe source is of particular interest, as it provides monoenergetic 5.9 keV γ -rays which are absorbed by the photoelectric effect and thus appear as a peak in the ToT spectrum.

The influence of the high voltage on the ToT of the ^{55}Fe peak is studied. Above 60 V amplification effects occur. A similar behaviour is observed for the ToT in measurements with a LED at different temperatures. A comparison of the measurement with ^{55}Fe at 30 °C and 80 °C shows that the increase of the ToT is more pronounced at lower temperatures and thus supports the theory of amplification. As the mean free path of the electrons is longer at lower temperatures, amplification effects are stronger. These measurements are performed with a temperature chamber which can heat only. A repetition with a cooled sensor would be very interesting as the effects should be even more pronounced.

12 Discussion and Outlook

By X-ray fluorescence atoms can be forced to emit characteristic X-rays. Targets with K_α lines in the range of 4.47 keV up to 17.48 keV are chosen and ToT spectra recorded. By doing so, an energy calibration becomes possible. An exponential dependency between ToT and energy is observed as expected by the pulshape. The analysis of the energy resolution yields relative energy resolutions in the range of 10 % to 20 %, sufficiently good for *Mu3e*. The energy resolution suffers from charge sharing between the pixels. Larger pixel sizes as in the final experiment should show better energy resolutions.

The influence of the temperature on the sensor performance is studied by heating the sensor up to 80 °C.

A shift in ToT of the ^{55}Fe peaks is observed and compared to corresponding test pulses. With higher temperatures the ToT decreases. As there is almost no difference between the measurements with ^{55}Fe and the test pulses, this effect is mainly caused by the electronics. The feedback capacitor of the CSA is discharged faster, which leads to shorter ToT and smaller signal amplitudes. The pulse shape should be analysed at different temperatures and compared to the simulation in order to fully understand the temperature dependency.

Additionally, the noise is observed to increase with temperature as expected.

The *MuPix2* sensor is equipped with a temperature sensing diode. With the temperature the current-voltage characteristic of the diode changes so the diode can be used as a thermometer. A first calibration is performed, but for the utilisation in the *Mu3e* the current-voltage characteristic has to be measured more precisely.

A first testbeam measurement has been performed at the *SPS* with a secondary beam of 180 GeV/ c pions together with the *Timepix* telescope.

As the run time was a few hours only little amounts of data could be collected. An analysis of the cluster size shows that clusters of more than

four pixels occur with a probability below 4%. Large clusters are not due to charge sharing but are caused by showers produced in the surrounding material.

The combined analysis of the *Timepix* and *MuPix* data can provide information about the efficiency of the single pixels and cross talk but again will suffer from the small number of particles hits.

For the future, a longer testbeam run would be desirable – perhaps at *DESY*¹ together with the *EUDET* telescope or at *PSI*, because *CERN* will shut down the *LHC* beginning of 2013 and consequently terminate testbeam activities in the meantime.

Moreover, the signal produced by a minimal ionising particle (MIP) is interesting to know. This can also be done at a testbeam but of course spectral ToT measurements of single pixels require again long run times.

12.2 Summary

The first *HV-MAPS* prototypes for *Mu3e* are successfully tested.

Good SNR values are measured with internally generated test pulses. The timing performance is mainly investigated by a LED setup and yields time constants in the range of μs . By means of spectral measurements with X-rays in the range of 4.5 keV to 17.5 keV, an energy calibration is performed. Pixel-to-pixel non-uniformities can be compensated by a tuning procedure. The influence of the temperature on the detection performance is studied and a first calibration of the temperature-sensing diode is performed.

Pixel sensors made in the *HV-MAPS* technology appear to be a suitable candidate for the *Mu3e* tracking detector. Nevertheless, the expected benefits from the fast charge collection via drift have so far not been observed. An improvement of the timing is desirable for the use of *HV-MAPS* in the *Mu3e* experiments.

¹*Deutsches Elektronen-Synchrotron*

12.3 Outlook

The cross talk between pixels has not been measured so far. Perhaps the combined analysis of the *Timepix* and *MuPix* data can provide first results. Otherwise, the cross talk can be determined by a new testbeam measurement with a telescope or with a laser with a small beam spot – order of μm or less. The *MuPix3* features also the possibility to apply test pulses to one row only. Pulses detected in the neighbouring pixels would indicate cross talk. For later submissions, a chequerboard like test pulse pattern would be interesting.

One of the main reasons that the *HV-MAPS* technology is chosen for *Mu3e* is the possibility of thinning. It has to be measured how thin the sensor can actually be made without insupportable reductions of detection performance. Since part of the collected charge carriers results from the bulk, the total amount of collected charges decreases and the shape of the signal is changed by thinning. Moreover, the depletion zone can be damaged during the thinning process.

The recently submitted third prototype version *MuPix3*² has a pixel size of $(92 \times 80) \mu\text{m}^2$ and thus for the first time nearly the final pixel size. Moreover, the sensitive area is larger. *MuPix3* has to be carefully tested and compared to results of the previous *MuPix* sensors. The size of the diode has not changed with respect to the previous sensors so no increase in noise caused by larger detector capacitances is expected. However, the fill-factor might be reduced as a result.

Moreover, some modifications concerning timing are made to this prototype and have to be studied as well.

Finally, if the sensor overcomes these tests a first detector prototype – for example two sensors placed as in a double-layer – can be built.

²Submission was in August 2012.

Part IV
Appendix

1 PN-Junction

A pn-junction is the boundary between p-doped and n-doped semiconductor material. Because of the differences in concentration of free charge carriers in both materials, electrons start to diffuse into the p-doped and holes into the n-doped material. The electrons recombine with the holes on the p-side and the holes with the electrons on the n-side. Positive donor ions on the n-side and negative acceptor ions on the p-side are left behind which leads to the formation of an electric field across the pn-junction. This field works against the diffusion process and eventually stops it in the thermal equilibrium. The potential difference due to the electric field is called contact potential. The pn-junction results in a depletion layer without mobile charge carriers.

The width of the depletion layer can be easily calculated by applying an one dimensional model (the x-direction will be chosen, calculations are based on [Leo94, Spi08]).

With the voltage U , the charge density distribution ρ , the dielectric constant ϵ_0 and the relative permittivity ϵ the Poisson's equation reads as follows

$$\frac{d^2 U(x)}{dx^2} = -\frac{\rho(x)}{\epsilon_0 \epsilon}. \quad (1)$$

$\rho(x)$ will be approximated by a uniform charge distribution with x_n being the extent of the depletion zone to the n-side and x_p to the p-side

$$\rho(x) = \begin{cases} eN_D & \text{for } 0 < x \leq x_n \\ -eN_A & \text{for } -x_p < x \leq 0. \end{cases} \quad (2)$$

Herein e is the electric charge and N_A and N_D the acceptor and donor impurity concentrations.

Integration of equation (1) under the constraint that $\frac{dU}{dx} = 0$ at $x = x_n$ and $x = -x_p$ yields

$$\frac{dU(x)}{dx} = \begin{cases} -\frac{eN_D}{\epsilon_0\epsilon}(x - x_n) & \text{for } 0 < x \leq x_n \\ \frac{eN_A}{\epsilon_0\epsilon}(x + x_p) & \text{for } -x_p < x \leq 0. \end{cases} \quad (3)$$

This equation describes the electric field within the depletion layer. Further integration leads to

$$U(x) = \begin{cases} -\frac{eN_D}{\epsilon_0\epsilon}\left(\frac{x^2}{2} - x_n x\right) + C & \text{for } 0 < x \leq x_n \\ \frac{eN_A}{\epsilon_0\epsilon}\left(\frac{x^2}{2} + x_p x\right) + C' & \text{for } -x_p < x \leq 0. \end{cases} \quad (4)$$

Both cases of equation (4) must be equal at $x = 0$ and hence the integration constants: $C = C'$.

At $x = x_n$ the voltage equals the contact potential, $U(x_n) = U_0$, and thus

$$U_0 = \frac{eN_D}{2\epsilon_0\epsilon}x_n^2 + C, \quad (5)$$

and at $x = -x_p$ it is $U(-x_p) = 0$ and therefore

$$0 = -\frac{eN_A}{2\epsilon_0\epsilon}x_p^2 + C. \quad (6)$$

The elimination of the constant C leads to

$$U_0 = \frac{e}{2\epsilon_0\epsilon} \left(N_D x_n^2 + N_A x_p^2 \right). \quad (7)$$

As the total charge is conserved, $N_D x_p = N_A x_n$, x_n and x_p can be obtained

$$x_n = \sqrt{\frac{2\epsilon_0\epsilon U_0}{2eN_D(1 + N_D/N_A)}} \quad (8)$$

$$x_p = \sqrt{\frac{2\epsilon_0\epsilon U_0}{2eN_A(1 + N_A/N_D)}}. \quad (9)$$

The depletion layer will thus extend further in the lighter doped side of the pn-junction.

This yields the width d of the depletion layer

$$d = x_n + x_p = \sqrt{\frac{2\epsilon_0\epsilon U_0}{e} \frac{N_A + N_D}{N_A N_D}}. \quad (10)$$

In the case of a highly doped n-side, $N_D \gg N_A$, the depletion width becomes approximately:

$$d \approx x_p \approx \sqrt{\frac{2\epsilon_0\epsilon U_0}{e N_A}}. \quad (11)$$

If ionising radiation enters the depletion zone it produces electron and hole pairs. Because of the electric field inside the depletion layer these charge carriers will be swept out of it and can be detected as an electronic signal. Thus, pn-junctions are of great interest for particle detectors.

If an additional reverse-bias voltage is applied the width of depletion layer grows and thus the field strengths and the sensitive volume. In this case the term U_0 in equation (10) has to be replaced by $U_0 + U_B$ with the reverse-bias voltage U_B

$$d = \sqrt{\frac{2\epsilon_0\epsilon(U_0 + U_B)}{e} \frac{N_A + N_D}{N_A N_D}} \quad (12)$$

$$\xrightarrow{U_0 \ll U_B} \approx \sqrt{\frac{2\epsilon_0\epsilon U_B}{e} \frac{N_A + N_D}{N_A N_D}}. \quad (13)$$

Another quantity of interest is the charge collection time t_C that a charge carrier needs to traverse the whole depletion zone.

The drift velocity saturates at high electric fields due to interactions of the charge carriers with optical phonons. With the saturation velocity $v_{\text{saturation}}$, the charge collection time becomes

$$t_C = \frac{d}{v_{\text{saturation}}}. \quad (14)$$

The generated charge carriers do not follow straightly the electric field lines towards the electrodes but also have a certain transverse motion due to thermal diffusion. The resulting transverse spread of the charge can be regarded as Gaussian-distributed with a standard deviation of

$$\sigma_{\text{transverse}} = \sqrt{2Dt}, \quad (15)$$

with the time t the charges are travelling and the diffusion constant $D = \frac{k_{\text{B}}T}{e}\mu$ (k_{B} : Boltzmann constant, T : temperature, μ : mobility).

Inserting the the charge collection time t_{C} the transverse diffusion yields

$$\sigma_{\text{transverse}} = \sqrt{2Dt} \approx \sqrt{2\frac{k_{\text{B}}T}{e}\mu t_{\text{C}}}. \quad (16)$$

2 The CR-RC Filter

A CR-RC filter consists of a high and a low pass in series (see figure 1).

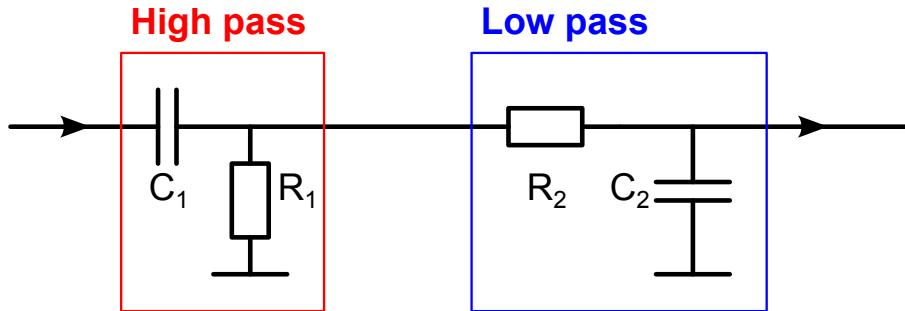


Figure 1: A CR-RC filter consisting of an high and a low pass

The following calculations are based on [Spi08].

Assuming that the incoming voltage is a step function with amplitude U_0 ,

$$U_{\text{in}}(t) = U_0 \Theta(t) \quad (17)$$

the response of a CR-RC filter can be calculated as follows:

Firstly, the high pass is discussed. The voltages at the capacitor (U_{C_1}) and at the resistor (U_{R_1}) are

$$U_{C_1} = \frac{Q}{C_1} \quad (18)$$

$$U_{R_1} = R_1 \dot{Q}, \quad (19)$$

wherein Q is the electric charge, C_1 the capacitance and R_1 the resistance of the high pass.

Application of Kirchhoff's mesh rule yields

$$U_{C_1} + U_{R_1} = U_{\text{in}} \quad (20)$$

$$\Rightarrow \frac{Q}{C_1} + R_1 \dot{Q} = U_{\text{in}}. \quad (21)$$

The homogeneous solution ($U_{\text{in}} = 0$) is as follows

$$\frac{Q}{C_1} + R_1 \dot{Q} = 0 \quad (22)$$

$$\Leftrightarrow \frac{\dot{Q}}{Q} = -\frac{1}{R_1 C_1}. \quad (23)$$

This will then be integrated over the time t

$$\int_{t_0=0}^t \frac{\dot{Q}}{Q} dt = - \int_{t_0=0}^t \frac{1}{R_1 C_1} dt \quad (24)$$

$$\Rightarrow \ln\left(\frac{Q}{Q_0}\right) = -\frac{t}{R_1 C_1} \quad (25)$$

$$\Rightarrow Q = Q_0 e^{-\frac{t}{R_1 C_1}} \quad (26)$$

with $Q_0 = Q(t = 0)$.

The inhomogeneous solution can be obtained by varying the constant. Allowing for a time-dependent Q_0 equation 21 becomes

$$\frac{Q_0}{C_1} e^{-\frac{t}{R_1 C_1}} + R_1 \dot{Q}_0 e^{-\frac{t}{R_1 C_1}} - R_1 \frac{Q_0}{R_1 C_1} e^{-\frac{t}{R_1 C_1}} = U_{\text{in}} \quad (27)$$

$$\Rightarrow \dot{Q}_0 = \frac{U_{\text{in}}}{R_1} e^{-\frac{t}{R_1 C_1}}. \quad (28)$$

Integrating once more over time results in

$$Q_0 = U_0 C_1 \left(e^{\frac{t}{R_1 C_1}} - 1 \right) \quad (29)$$

$$\Rightarrow Q = U_0 C_1 \left(1 - e^{-\frac{t}{R_1 C_1}} \right). \quad (30)$$

Thus, the outgoing voltage is

$$U_{\text{out}} = \dot{Q} R_1 \quad (31)$$

$$= U_0 e^{-\frac{t}{R_1 C_1}}. \quad (32)$$

If a time constant $\tau_1 \equiv R_1 C_1$ is defined, equation 32 becomes

$$U_{\text{out}} = U_0 e^{-\frac{t}{\tau_1}} . \quad (33)$$

The following low pass with capacitance C_2 and resistance R_2 as well obeys Kirchhoff's mesh rule (see equation 21)

$$U_{C_2} + U_{R_2} = U_{\text{out}} \quad (34)$$

$$\Rightarrow \frac{Q}{C_2} + R_2 \dot{Q} = U_{\text{out}} , \quad (35)$$

with a small difference: the incoming voltage is the outgoing voltage U_{out} of the high pass.

Thus, the homogeneous solution does not change with respect to equation 26

$$\Rightarrow Q = Q_0 e^{-\frac{t}{R_2 C_2}} , \quad (36)$$

but the inhomogeneous solution changes slightly

$$\frac{Q}{C_2} + R_2 \dot{Q} = U_{\text{out}} \quad (37)$$

$$\Rightarrow \left(\frac{Q_0}{C_2} + R_2 \dot{Q}_0 - R_2 \frac{Q_0}{R_2 C_2} \right) e^{-\frac{t}{R_2 C_2}} = U_0 e^{-\frac{t}{R_1 C_1}} \quad (38)$$

$$\Leftrightarrow \dot{Q}_0 = \frac{U_0}{R_2} e^{\left(\frac{1}{\tau_2} - \frac{1}{\tau_1}\right)t} . \quad (39)$$

Herein a time constant $\tau_2 \equiv R_2 C_2$ has been applied.

Integrating over time leads to

$$\Rightarrow Q_0 = \frac{U_0}{R_2} \frac{\tau_1 \tau_2}{\tau_1 - \tau_2} \left(e^{\left(\frac{1}{\tau_2} - \frac{1}{\tau_1}\right)t} - 1 \right) \quad (40)$$

$$\Rightarrow Q = U_0 C_2 \frac{\tau_1}{\tau_1 - \tau_2} \left(e^{-\frac{t}{\tau_1}} - e^{-\frac{t}{\tau_2}} \right) . \quad (41)$$

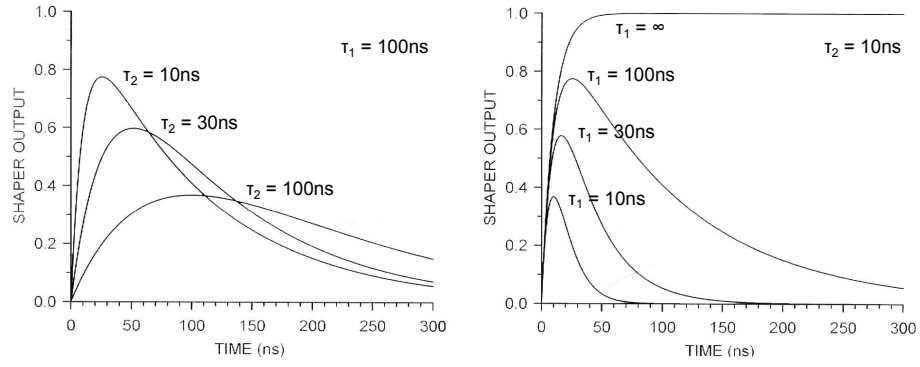


Figure 2: Response of the CR-RC filter for different time constants (graphic taken from [Spi08])

Thus the output voltage of the CR-RC filter becomes

$$U = \frac{Q}{C_2} \quad (42)$$

$$= U_0 \frac{\tau_1}{\tau_1 - \tau_2} \left(e^{-\frac{t}{\tau_1}} - e^{-\frac{t}{\tau_2}} \right). \quad (43)$$

In the case of equal time constants $\tau_1 = \tau_2 \equiv \tau$ the output voltage is

$$U = U_0 \frac{t}{\tau} \exp\left(-\frac{t}{\tau}\right). \quad (44)$$

The response of the CR-RC filter for various time constants is shown in figure 2. The shape of the falling edge is determined by τ_1 and the rising edge by τ_2 .

3 The Configuration and Data Readout Software

The configuration and the data readout of the sensor is controlled by a C++ based computer program. The graphical user interface is shown in figure 3. The main functions are described in this chapter.

Get Ready All configurations are set, e. g. bias voltages, threshold, pixel. The values of the bias voltages which are improved for good timing can be found in table 1.

SetAllTDACs All TDACs are given the value entered in the field 'TDAC'. Default is 0. 'Get Ready' has to be pressed afterwards.

Start Sequencer A series of 128 test pulses is generated. The number of detected pulses is counted for a single pixel.

TOT Scan A series of test pulses is generated and the resulting ToT spectrum of a single pixel is plotted.

Spect Meas The ToT spectrum of a single pulse is plotted. This can be used for spectral measurements of external sources as for example the radioactive sources.

InputScan For a single pixel a series of test pulses is generated and the number of detected pulses is counted. This is repeated for lower and lower injection voltages until no more pulse is detected. The result is plotted and fitted by an error function.

ReadFifo A test pulse is applied to the sensor and the hit-flags of the entire pixel matrix are read out and plotted.

Effi The ratio of pixels that detect a test pulse is counted. The injection voltage is swept from 0 V to the maximum voltage of 1.8 V. The result is plotted.

FastScanAllPixels (Thr) & FastScanAllPixels (Amp) For the entire pixel matrix a threshold/injection scan is performed. For each threshold/injection a test pulse series is generated. The hit-flags are stored in the FPGA after each test pulse. The resulting histograms are fitted afterwards. The results are stored in a text file.

FastTune This procedure determines the best TDAC³ value for each pixel. At first, all TDACs are set to 7. A series of test pulses is applied. Pixels that detected $\sim 50\%$ of the pulses are assigned the actual TDAC value. For the remaining pixels the procedure is repeated with a higher (more than 50% of the pulses have been detected) or lower (less than 50%) TDAC value. Pixels which would need an even lower or higher TDAC value are assigned 0 or 15 respectively. The result is stored in a text file.

LdTuneVal All TDACs are given the values determined by the ‘FastTune’ procedure. ‘Get Ready’ has to be pressed afterwards.

SweepTune For a single pixel a threshold scan is performed for every TDAC value. The resulting mean of the error function fit is plotted against the TDAC value.

³It is a 4 bit DAC. Values from 0 to 15 are possible.

3 The Configuration and Data Readout Software

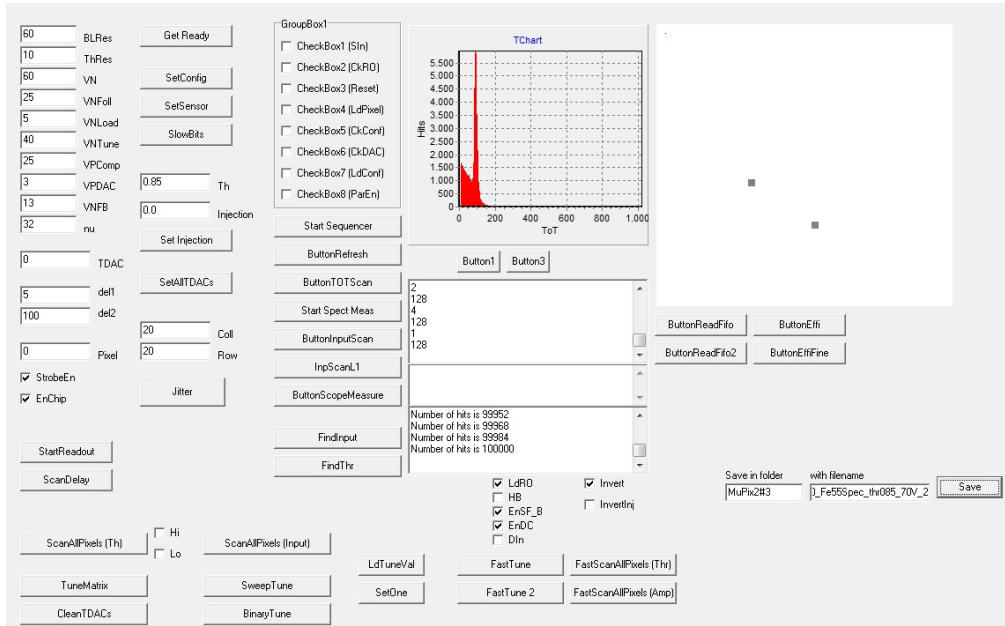


Figure 3: Screenshot of the configuration and data readout software

Bias voltage	Default configuration	New configuration
BLRes	60	60
ThRes	10	10
VN	60	60
VNFoll	10	25
VNLload	5	5
VNTune	0	40
VPComp	5	25
VPDAC	1	3
VNFb	1	13
nu	32	32

Table 1: Bias voltages improved for timing

Lists

4 List of Figures

2.1	Standard Model of particle physics	6
2.2	Feynman diagram of the decay $\mu^+ \rightarrow e^+e^-e^+$ via neutrino mixing in a loop	8
2.3	Diagrams of the decay $\mu^+ \rightarrow e^+e^-e^+$ in new physics models	9
2.4	Reach in mass scale for the experiments <i>SINDRUM</i> , <i>MEG</i> and <i>Mu3e</i>	10
3.1	Lepton flavour conserving muon decays	12
3.2	Sources of accidental background	16
3.3	Effective branching ratio as function of the missing energy	17
3.4	Experimental hall at <i>PSI</i>	19
3.5	Design of the <i>Mu3e</i> detector	20
3.6	Mechanical prototypes	23
4.1	Bonds and lattice structure of silicon	26
4.2	Energy band structure of semiconductors	26
4.3	N- and P-doping in silicon	27
4.4	Energy loss due to inelastic collisions for electrons and positrons respectively obtained with the Berger-Seltzer formula . . .	31
4.5	Energy loss due to inelastic collisions and bremsstrahlung for electrons and positrons respectively	32
4.6	Principle of a <i>HV-MAPS</i>	34
5.1	Electronics of the <i>MuPix</i> inside the pixel and on the chip periphery	38
5.2	Photographs of the <i>MuPix</i> prototype	40
5.3	Schematic of the setup	41
5.4	Complete experimental setup in the laboratory	41
5.5	Uxibo and PCB with sensor	42

Lists

6.1	Injection-scan of a central pixel	44
6.2	Fit results of injection-scans at various thresholds	46
6.3	SNR obtained with the injection-scan and the ^{55}Fe source as signal reference	46
6.4	Fast injection-scan of all pixels in the pixel matrix	47
6.5	Fast threshold-scan of all pixels in the pixel matrix	48
6.6	Mean value obtained by a threshold-scan for a central pixel as function of the TDAC value	49
6.7	TDAC values obtained with the fast-tune procedure	50
6.8	Fraction of activated pixels in the matrix as function of the injection pulse	51
6.9	Threshold-scan for the entire pixel matrix performed before and after tuning	52
6.10	Latency of randomly chosen pixels obtained with test pulses	53
6.11	Single-pixel jitter of randomly chosen pixels obtained with test pulses	53
6.12	Influence of the pulse height on the latency	54
7.1	Schematic of the LED or laser diode setup	56
7.2	Influence of the applied high-voltage on the latency and time-over-threshold of a central and a corner pixel	57
7.3	Principle of the pulse shape measurement	59
7.4	Pulse shape with fitted CR-RC filter response	60
7.5	Comparison of pulse shapes	61
7.6	Double pulse measurement	62
7.7	Double pulse resolution	63
7.8	Influence of threshold and deposited energy on the double pulse resolution	63
7.9	Overlay of 100 pictures of a pinhole illuminated with a LED taken with the <i>MuPix</i> sensor	64
8.1	ToT spectrum of the ^{90}Sr source	67
8.2	ToT spectrum of the ^{55}Fe source	68
8.3	Shift of the ^{55}Fe γ -peak as a function of the threshold . . .	68
8.4	Shift of the ^{55}Fe γ -peak as a function of the high voltage .	69
8.5	Shift of the ^{55}Fe γ -peak as a function of the applied high voltage at 30 °C and 80 °C	70
9.1	X-ray fluorescence	72
9.2	Photograph of the X-ray fluorescence setup	72

9.3	ToT spectra of the different X-ray fluorescence targets of a central pixel	73
9.4	Plot of the ToT of the photoelectric peak of the various K_α lines	74
9.5	Energy resolution determined in the X-ray fluorescence spectra	75
10.1	ToT spectra of ^{55}Fe γ -rays at different temperatures	78
10.2	Influence of the temperature on the ToT of the photoelectric peak of the ^{55}Fe γ -rays	79
10.3	ToT spectra of injection pulses at different temperatures .	80
10.4	Influence of the temperature on the ToT of injection pulses	80
10.5	Electronics inside the pixel	81
10.6	Simulation of the output pulse at different temperatures .	81
10.7	Injection-scan at various temperatures for a central pixel .	83
10.8	Resistance of the temperature diode for different temperatures	85
11.1	Accelerators at <i>CERN</i>	88
11.2	Setup with the <i>MuPix</i> sensor at the DUT position of the <i>Timepix</i> telescope	88
11.3	At the testbeam area T4-H8	89
11.4	Distribution of hits over the pixel matrix	90
11.5	Histogram of the number of hits in a single pixel	90
11.6	Plots of the hit pixels during gate of the <i>Timepix</i> telescope	91
11.7	Histogram of the size of clusters during one gate of the <i>Timepix</i>	91
1	A CR-RC filter consisting of an high and a low pass	107
2	Response of the CR-RC filter for different time constants .	110
3	Screenshot of the configuration and data readout software	113

5 List of Tables

3.1	Branching ratios of various muon decay modes	11
3.2	Limits on branching ratios for lepton flavour violating muon decays and muon-to-electron conversion experiments	14
3.3	Geometry of the elements of the tracking detector	22
4.1	Important properties of silicon	26
4.2	Quantities of silicon	30
7.1	Time constants of the CR-RC filter derived by fit	59
9.1	Energies of the K-lines of the various target materials . . .	71

Lists

10.1	Absolute values of the slope obtained by a linear fit	82
1	Bias voltages improved for timing	113

Bibliography

- [A⁺01] Q. R. Ahmad et al. Measurement of the charged current interactions produced by B-8 solar neutrinos at the Sudbury Neutrino Observatory. *Phys. Rev. Lett.*, 87:071301, 2001.
- [A⁺11] J. Adam et al. New limit on the lepton-flavour violating decay $\mu^+ \rightarrow e^+\gamma$. *Phys. Rev. Lett.*, 107:171801, 2011.
- [Aok10] Masaharu Aoki. A new idea for an experimental search for $\mu - e$ conversion. *PoS*, ICHEP2010:279, 2010.
- [Aok12] M. Aoki. An experimental search for muon-electron conversion in nuclear field at sensitivity of 10^{-14} with a pulsed proton beam. *AIP Conf.Proc.*, 1441:599–601, 2012.
- [Aug12] Heiko Christian Augustin. Charakterisierung von HV-MAPS. Bachelor's Thesis, Ruprecht-Karls-Universität Heidelberg, 2012.
- [B⁺88] U. Bellgardt et al. Search for the Decay $\mu^+ \rightarrow e^+e^+e^-$. *Nucl.Phys.*, B299:1, 1988.
- [B⁺99] M. L. Brooks et al. New limit for the family-number non-conserving decay $\mu^+ \rightarrow e^+\gamma$. *Phys. Rev. Lett.*, 83:1521–1524, 1999.
- [B⁺06] Wilhelm H. Bertl et al. A search for $\mu - e$ conversion in muonic gold. *Eur. Phys. J.*, C47:337–346, 2006.
- [B⁺12] A. Blondel et al. Letter of intent for an experiment to search for the decay $\mu \rightarrow eee$. 2012.
- [Ber02] Christoph Berger. *Elementarteilchenphysik*. Springer-Lehrbuch. Springer, Berlin ; Heidelberg [et al.], 2002.
- [C⁺08] R.M. Carey et al. Proposal to search for $\mu^- N \rightarrow e^- N$ with a single event sensitivity below 10^{-16} . *FERMILAB-PROPOSAL-0973*, 2008. Spokespersons: J.P. Miller, R.H. Bernstein.

Bibliography

- [C⁺09] Y.G. Cui et al. Conceptual design report for experimental search for lepton flavor violating $\mu^- - e^-$ conversion at sensitivity of 10^{-16} with a slow-extracted bunched proton beam (COMET). *KEK-2009-10*, 2009.
- [CER12] CERN. The accelerator complex. <http://public.web.cern.ch/public/en/research/AccelComplex-en.html>, September 2012.
- [DD10] C. Dritsa and M. Deveaux. A detector response model for CMOS monolithic active pixel sensors. *PoS*, BORMIO2010:015, 2010.
- [DK09] Rashid M. Djilkibaev and Rostislav V. Konoplich. Rare Muon Decay $\mu^+ \rightarrow e^+e^-e^+\nu_e\bar{\nu}_\mu$. *Phys.Rev.*, D79:073004, 2009.
- [E⁺03] K. Eguchi et al. First results from KamLAND: Evidence for reactor anti- neutrino disappearance. *Phys. Rev. Lett.*, 90:021802, 2003.
- [F⁺98] Y. Fukuda et al. Evidence for oscillation of atmospheric neutrinos. *Phys. Rev. Lett.*, 81:1562–1567, 1998.
- [FER12] FERMILAB. What is the world made of? <http://www.fnal.gov/pub/inquiring/matter/madeof/index.html>, September 2012.
- [Gri11] David J. Griffiths. *Introduction to elementary particles*. Wiley-VCH, Weinheim, 2. rev. edition, 2011.
- [Hig12] *Higgs booklet: First observations of a new particle in the search for the Standard Model Higgs boson at the LHC*. 2012.
- [Hun11] Siegfried Hunklinger. *Festkörperphysik*. Oldenbourg, München, 3. rev. edition, 2011.
- [Hus12] Ulrich Husemann. A New Pixel Detector for the CMS Experiment. May 2012. Talk.
- [K. 10] K. Nakamura et al. (Particle Data Group). Particle physics booklet, July 2010. *J. Phys. G* 37.
- [Kit11] Charles Kittel. *Introduction to solid state physics*. Oldenbourg, 2011.

- [Kun08] Yoshitaka Kuno. Lepton flavor violation: Muon to electron conversion, COMET and PRISM/PRIME at J-PARC. *PoS, NUFACT08*:111, 2008.
- [Kun10] Yoshitaka Kuno. Search for muon to electron conversion at J-PARC: COMET. *PoS, ICHEP2010*:526, 2010.
- [Leo94] William R. Leo. *Techniques for Nuclear and Particle Physics Experiments*. Springer, 1994.
- [Lut07] Gerhard Lutz. *Semiconductor radiation detectors*. Springer, Berlin ; Heidelberg [et al.], 2007.
- [MS08] Brian R. Martin and Graham Shaw. *Particle physics*. Wiley, Chichester [et al.], 3. edition, 2008.
- [Per12] I. Perić. Private communication. 2011/12.
- [Per07] I. Perić. A novel monolithic pixelated particle detector implemented in high-voltage CMOS technology. *Nucl.Instrum.Meth.*, A582:876–885, 2007.
- [Per12a] I. Perić. MuPixel small pixel detector description. March 2012.
- [Per12b] Ivan Perić. Forschungsgruppe neuartige Detektoren für wissenschaftliche und medizinische Anwendungen - Neuartige monolithische Pixelsensoren zum Teilchennachweis. http://www.ziti.uni-heidelberg.de/ziti/index.php?option=com_content&view=article&id=128&Itemid=76&lang=de, February 2012.
- [PJU⁺10] J. Pasternak, L. Jenner, Y. Uchida, R. Barlow, K. Hock, et al. Accelerator and Particle Physics Research for the Next Generation Muon to Electron Conversion Experiment - the PRISM Task Force. WEPE056, 2010.
- [PKF10] I. Perić, C. Kreidl, and P. Fischer. Particle pixel detectors in high-voltage CMOS technology—New achievements. *Nucl. Instrum. Meth. A*, In Press, Corrected Proof:–, 2010.
- [Pla10] Richard Plackett. Timepix Telescope - A new high resolution, time tagging telescope. November 2010. Talk.
- [Pov09] Bogdan Povh. *Teilchen und Kerne*. Springer, Berlin ; Heidelberg, 8. edition, 2009.

Bibliography

- [PT10] I. Perić and C. Takacs. Large monolithic particle pixel-detector in high-voltage CMOS technology. *Nucl. Instrum. Meth.*, A624(2):504 – 508, 2010. New Developments in Radiation Detectors - "Proceedings of the 11th European Symposium on Semiconductor Detectors, 11th European Symposium on Semiconductor Detectors".
- [PTB⁺10] I. Perić, C. Takacs, J. Behr, F. M. Wagner, and P. Fischer. The first beam test of a monolithic particle pixel detector in high-voltage CMOS technology. May 2010.
- [SB82] Stephen M. Seltzer and Martin J. Berger. Evaluation of the collision stopping power of elements and compounds for electrons and positrons. *The International Journal of Applied Radiation and Isotopes*, 33(11):1189 – 1218, 1982.
- [SB84] Stephen M. Seltzer and Martin J. Berger. Improved procedure for calculating the collision stopping power of elements and compounds for electrons and positrons. *Int. J. Appl. Radiat. Isot.*, 35(7):665–676, 1984.
- [SBN11] André Schöning, Sebastian Bachmann, and Rohin Narayan. A novel experiment to search for the decay $\mu \rightarrow eee$. *Physics Procedia*, 17(0):181 – 190, 2011. 2nd International Workshop on the Physics of fundamental Symmetries and Interactions - PSI2010.
- [sem12] <http://upload.wikimedia.org/wikipedia/commons/c/c7/Isolator-metal.svg>, October 2012.
- [sib12] http://upload.wikimedia.org/wikipedia/commons/0/04/Band_structure_Si_schematic.svg, October 2012.
- [SN07] Simon Min Sze and Kwok K. Ng. *Physics of semiconductor devices*. Wiley, New York, NY, 3. edition, 2007.
- [Spi08] Helmuth Spieler. *Semiconductor detector systems*. Oxford Univ. Press, Oxford [et al.], repr. edition, 2008.
- [tim] The Timepix Chip. <http://medipix.web.cern.ch/medipix/pages/medipix2/timepix.php>.
- [Tsc11] R. Tschirhart. The Mu2e experiment at Fermilab. *Nucl.Phys.Proc.Suppl.*, 210-211:245–248, 2011.

- [uxi12] Uxipedia. http://www.uxibo.de/uxipedia/index.php/Main_Page, October 2012.
- [Zim12] Marco Zimmermann. Cooling with Gaseous Helium for the Mu3e Experiment. Bachelor's Thesis, Ruprecht-Karls-Universität Heidelberg, 2012.

Acknowledgements

At the end of my thesis, I would like to express my thanks to everyone that accompanied me during my time in the *Mu3e* group.

First of all, I would like to thank Prof. Dr. André Schöning for offering me the possibility to carry out a thesis on this exciting topic and his support along the way, and Priv.-Doz. Dr. Maarten DeKieviet who agreed to be the second examiner.

My special thanks to the developer of the sensor Dr. Ivan Perić for all his help and support and the fruitful discussions.

I thank Dr. Dirk Wiedner who supervised me for supporting me in words and deeds during the whole time.

I would like to thank Heiko Augustin, Dr. Niklaus Berger and Moritz Kiehn for their help and advice and for proofreading, and the working group in general for the pleasant atmosphere.

Furthermore, I would like to thank Ralf Achenbach who thought me the bonding of the sensors, Dr. Jens Wagner and Gerhard Lamade for their support during the measurements at the students lab course and Dr. Daniel Hynds and Dr. Heinrich Schindler for the possibility to have testbeam and their support throughout the measurements.

Last but not least, I would like to thank Thorwald Klapdor-Kleingrothaus and my family and friends for their support, in particular towards the end of my studies.

Erklärung

Ich versichere, dass ich diese Arbeit selbstständig verfasst habe und keine anderen als die angegebenen Quellen und Hilfsmittel benutzt habe.

Heidelberg, den 30. Oktober 2012

.....
(Ann-Kathrin Perrevoort)